UNIVERSITY OF CALIFORNIA, SAN DIEGO

Applications of Nanotechnology to the Central Nervous System

A dissertation submitted in partial satisfaction of the
requirements for the degree
Doctor of Philosophy

in

Bioengineering

by

James P. Blumling III

Committee in charge:

Professor Gabriel Silva, Chair
Professor Michael Heller
Professor Sungho Jin
Professor Michael Sailor
Professor Shankar Subramaniam

2012

The dissertation of James P. Blumling III is approved, and it is acceptable in quality and form for publication on microfilm and electronically:

_____

_____

_____

_____

_____
Chair

University of California, San Diego

2012

DEDICATION

I dedicate this dissertation to all the people in my life that have encouraged and supported me. I am extremely fortunate to possess a wonderful family, an amazing girlfriend, and a host of great friends and colleagues.

EPIGRAPH

Do what you can, with what you have, where you are.

— Theodore Roosevelt

TABLE OF CONTENTS

LIST OF ABBREVIATIONS

(+)DP	Cationic DP
(-)DP	Anionic DP
αmethyldopa	L-α-methyl-3,4-dihydroxyphenylalanine
AAV	Adeno-associated viral
ABC	ATP binding cassette
AcNP	NP of DNA and $CK_3$0PEG10 in the presence of acetate counter-ions
AD	Alzheimer's disease
AE	Arachnoid epithelium
AF647	Alexa Fluor 647
ALS	Amyotrophic lateral sclerosis
AM	Acetoxymethyl ester
AMD	Age-related macular degeneration
Anova	Analysis of variance
ANTS	8-Aminonaphthalene-1,3,6-trisulfonic acid
Apo	Apolipoprotein
APTES	(3-Aminopropyl)triethoxysilane
ARE	Antioxidant response element
ARPE-19	Human adult RPE cell line 19
A.U.	Arbitrary Units
BBB	Blood-brain barrier
Bcl	B-cell lymphoma
BCNU	N,N- bis(2-chloroethyl)-N-nitrosourea
BCRP	breast cancer resistance protein 1
BDNF	Brain-derived neurotrophic factor
bFGF	Basic fibroblast growth factor
bis-SorbPC	1,2-Bis[10-(2,4-hexadienoyloxy)decanoyl]-sn-glycero-3-phosphocholine
BMP	Betamethasone phosphate
BSA	Bovine serum albumin
CAM	Cell adhesion molecule
CaM	Calmodulin
CD	Canavan disease
CdS:MnZnS	Cadmium sulfide core/manganese zinc sulfide shell
CED	Convection-enhanced delivery
CFP	Cyan fluorescent protein
$CK_3$0PEG10	N-terminal cysteine polylysine (30-mer) conjugated to a 10 kDa PEG-maleimide
CMV	Cytomegalovirus

CNS	Central nervous system
CNV	Choroidal neovascularization
CPP	Cell-pepetrating peptide
CPT-11	Camptothecin-11
CSF	Cerebrospinal fluid
CT	Computed tomography
DAPI	4,6-diamidino-2-phenylindole
DDAB	Dimethyldioctadecylammonium bromide
DHLA	Dihydrolipoic acid
DL-NAM	D,L-2-amino-5-bis[(2-chloroethyl)amino]-1,2,3,4-tetrahydro-2-naphthoic acid and D,L-1-amino-7-bis[(2-chloroethyl)amino]-1,2,3,4-tetrahydro-l-naphthoic acid
DM	dexamethasone
DMEM	Dulbeccos modified eagle medium
DMSO	Dimethyl sulfoxide
DP	3rd generation poly(benzyl ether) functionalized porphyrin
DSPC	1,2-Distearoyl-sn-glycero-3- phosphocholine
DSS	Dioctyl sulfosuccinate sodium
EAU	Experimental autoimmune uveoretinitis
EDTA	Ethylenediametetraacetic acid
EGF	Epidermal growth factor
EGFR	EGF receptor
EM	Electron microscopy
ERG	Electroretinography
EthD-1	Ethidium homodimer-1
EtOH	Ethanol
EuLG	Eudragit® L100-gliclazide
EuRG	Eudragit® RSPO-gliclazide
EVAc	Ethylene-vinyl acetate copolymer
eYFP	Enhanced yellow fluorescent protein
FAcNP	NP of DNA and $CK_3$0PEG10 in the presence of trifluoroacetate counter-ions
FAD-SA	Fatty acid dimers and sebacic acid
FBS	Fetal bovine serum
FcRn	Neonatal Fc receptor
FITC	Fluorescein isothiocyanate
FRET	Förster RET
$FuCl_2$	Fumaryl chloride
FUS	Focused ultrasound
GABA	γ-Aminobutyric acid
GCV	Ganciclovir

GDNF	Glial-derived neurotrophic factor
GECI	Genetically encoded calcium indicator
GES	Genetically encoded sensor
GFAP	Glial fibrillary acidic protein
GFP	Green fluorescent protein
GPCR	G protein-coupled receptor
hAADC	Human aromatic L-amino acid decarboxylase
HBSS	Hank's balanced salt solution
HEPES	4-(2-hydroxyethyl)-1-piperazineethanesulfonic acid
hIR	Human insulin receptor
HIRMAb	Humanized/chimeric form of MAb83-14
HIV-1	Human immunodeficiency virus type 1
HSA	Human serum albumin
HUVEC	Human umbilical vascular endothelial cell
IA	Itaconic anhydride
ICC	Immunocytochemistry
ICV	Intracerebroventricular
IgG	Immunoglobulin G
IL	Interleukin
IPTG	Isopropyl β-D-1-thiogalactopyranoside
IR	Infrared
IRBP	Interphotoreceptor retinoid-binding protein
LAT-1	large neutral amino acid carrier
LDL	Low-density lipoprotein
LH	Leutenizing hormone
LLC	Lewis lung carcinoma cell line
LPS	Lipopolysaccharide
mAb	Monoclonal antibody
MEM	Minimum essential medium
MMOCT	Magnetomotive OCT
MNP	Magnetic NP
MPA	Methylprednisone acetate
MRI	Magnetic resonance imaging
MRP	Multidrug resistance-associated protein
MTH	Molecular trojan horse
NGF	Nerve growth factor
NLS	Nuclear localization sequence
NP	nanoparticle
NSET	Nanosurface energy transfer
OCT	Optical coherence tomography
ONL	Outer nuclear layer
OPTA	*o*-Phthalyic hemithioacetal
OS	Outer segment

PBS	Phosphate buffered saline
PCPP-SA	Copolymer of poly(bis(p-carboxy-phenoxy)propane) anhydride and sebacic acid
PCR	Polymerase chain reaction
PD	Parkinsons disease
PDL	Poly-D-lysine
PDT	Photodynamic therapy
PEG	Polyethylene glycol
PEG-DSPE	1,2-Distearoyl-sn-glycero-3-phosphoethanolamine-N-[methoxy(poly(ethylene glycol))-2000]
PEG-PHDCA	Poly(ethylene glycol-co-hexadecyl cyanoacetate)
PEGPL	PEG-block-poly(L-lysine)
PEI	Polyethyleneimine (also spelled polyethylenimine)
Pen/strep	Penicillin:streptomycin solution
Pgp	P-glycoprotein
PIL	PEGylated immunoliposome
PLA	Poly(lactic acid)
PLGA	Poly(lactic- co-glycolic acid)
PNA	Peptide nucleic acid
pNIPAAm	poly(N-isopropyl acrylamide)
polyR	Polyarginine
POPC	Palmitoyl-2-oleoyl-sn-glycerol-3-phosphocholine
PS	Photosensitizer
QD or qdot	Quantum dot
qRT-PCR	Quantitative RT-PCR
R8	octaarginine
R11	undecaarginine
RET	Resonance energy transfer
RMC	Retinal Müller cell
RMT	Receptor-mediated transcytosis
ROI	Region of interest
ROS	Reactive oxygen species
RPE	Retinal pigment epithelium
RT-PCR	Reverse transcription-PCR
RVG	Rabies virus glycoprotein
SAPNS	Self-assmebling peptide nanofiber scaffold
SC	Sodium cacodylate
shRNA	Short hairpin RNA
siRNA	Small interfering RNA
SLN	Solid lipid NP
SLX	Sialyl Lewis X
SOD1	Superoxide dismutase 1
SPR	Surface plasmon resonance

SR101	Sulforhodamine 101
SRB	Sulforhodamine B
sSLX	Synthetic analog of SLX
TAM	Tamoxifen
TAP	Transcriptionally active PCR product
TAT	Trans-activator of transcription
TCEP	Tris(2-carboxyethyl)phosphine
TEM	Transmission EM
TEOS	Tetraethyl orthosilicate
TfR	Insulin and transferrin receptor
TGFβ-2	Transforming growth factor β2
TMP	2,2,4-Trimethylpentane
TnC	Troponin C
TRITC	Tetramethylrhodamine isothiocyanate
UA	Uranyl acetate
UV	ultraviolet
VEGF	Vascular endothelial growth factor
WGA	Wheat germ agglutinin
YFP	Yellow fluorescent protein

LIST OF FIGURES

LIST OF TABLES

LIST OF GRAPHS

ACKNOWLEDGEMENTS

The authors would like to thank Dr. Marilyn Farquhar for the use of the electron microscopy facility, and Ying Jones and Timo Meerloo for aid with electron microscopy sample preparation.

Chapter 1, in full, is currently in preparation for submission. Blumling, James P.; Silva, Gabriel A. Diagnostic and therapeutic nanotechnologies with applications to the retina and optic nerve. The dissertation author was the primary author of this material.

Chapter 2, in full, is a reprint of the material as it appears in Blumling, James P.; Silva, Gabriel A. "Targeting the brain: advances in drug delivery." *Curr. Pharm. Biotechnol.*, in press (2012). The dissertation author was the primary author of this paper.

Chapter 3, in full, is a reprint of the material as it appears in Kim, Soon-Jong; Blumling, James P.; Davidson, Marie C.; Saad, Helen; Eun, Su-Yong; Silva, Gabriel A. Calcium and EDTA induced folding and unfolding of calmodulin on functionalized quantum dot surfaces, Journal of Nanoneuroscience, in press (2012). The dissertation author was second author of this paper.

Chapter 4, in part, contains data as it appears in Nguyen-Ta, Kim. Characterization of peptide-mediated delivery of quantum dots into cortical astrocytes. Thesis, UCSD, 2011. The dissertation author was a secondary investigator for this material.

Chapter 5, in full, has been submitted for publication of the material as it may appear in Blumling, James P.; Silva, Gabriel A. Sulforhodamine B-loaded polyethyleneimine/silica hybrid nanoparticles, Small, submitted (2012). The dissertation author was the primary investigator and author of this material.

VITA AND PUBLICATIONS

2006	B. S. in Biology and B. S. in Physics, Massachusetts Institute of Technology, Cambridge, MA
2008	M. S. in Bioengineering, University of California, San Diego, La Jolla, CA
2012	Ph. D. in Bioengineering, University of California, San Diego, La Jolla, CA

Blumling JP and Silva GA (submitted for review). "Sulforhodamine B-loaded polyethyleneimine/silica hybrid nanoparticles." *Small*.

Blumling JP, and Silva GA (in press). "Targeting the brain: advances in drug delivery." *Current Pharmaceutical Biotechnology*.

Kim S-J, **Blumling JP**, Davidson MC, Saad H, Eun S-Y, and Silva GA (in press). "Calcium and EDTA induced folding and unfolding of calmodulin on functionalized quantum dot surfaces." *Journal of Nanoneuroscience*.

Blumling JP, and Silva GA (in preparation). "Diagnostic and therapeutic nanotechnologies with applications to the retina and optic nerve."

Karp JM, Yeh J, Eng G, Fukuda J, **Blumling JP**, Suh K-Y, Cheng J, Mahdavi A, Borenstein J, Langer R, and Khademhosseini A (2007). "Controlling size, shape and homogeneity of embryoid bodies using poly(ethylene glycol) microwells." *Lab on a Chip*.

Khademhosseini A, Ferreira L, **Blumling JP**, Yeh J, Karp JM, Fukuda J, and Langer R (2006). "Co-culture of human embryonic stem cells with murine embryonic fibroblasts on microwell-patterned substrates." *Biomaterials*.

Fukuda J, Khademhosseini A, Yeo Y, Yang X, Yeh J, Eng G, **Blumling JP**, Wang C-F, Kohane D, and Langer R (2006). "Micromolding of shape-controlled, harvestable cell-laden hydrogels." *Biomaterials*.

Khademhosseini A, Eng G, Yeh J, Fukuda J, **Blumling JP**, Langer R, and Burdick JA (2006). "Micromolding of photocrosslinkable hyaluronic acid for cell encapsulation and entrapment." *Journal of Biomedical Materials Research*.

Yeh J, Ling Y, Karp JM, Gantz J, Chandawarkar A, Eng G, **Blumling JP**, Langer R, and Khademhosseini A (2006). "Micromolding of shape-controlled, harvestable cell-laden hydrogels." *Biomaterials*.

ABSTRACT OF THE DISSERTATION

Applications of Nanotechnology to the Central Nervous System

by

James P. Blumling III

Doctor of Philosophy in Bioengineering

University of California, San Diego, 2012

Professor Gabriel Silva, Chair

Nanotechnology and nanomaterials, in general, have become prominent areas of academic research. The ability to engineer at the nano scale is critical to the advancement of the physical and medical sciences. In the realm of physical sciences, the applications are clear: smaller circuitry, more powerful computers, higher resolution intruments. However, the potential impact in the fields of biology and medicine are perhaps even grander. The implementation of novel nanodevices is of paramount importance to the advancement of drug delivery, molecular detection, and cellular manipulation.

The work presented in this thesis focuses on the development of nanotech-

nology for applications in neuroscience. The nervous system provides unique challenges and opportunities for nanoscale research. This thesis discusses some background in nanotechnological applications to the central nervous system and details:

(1) The development of a novel calcium nanosenser for use in neurons and astrocytes. We implemented the calcium responsive component of Dr. Roger Tsien's Cameleon sensor, a calmodulin-M13 fusion, in the first quantum dot-based calcium sensor.

(2) The exploration of cell-penetrating peptides as a delivery mechanism for nanoparticles to cells of the nervous system. We investigated the application of polyarginine sequences to rat primary cortical astrocytes in order to assess their efficacy in a terminally differentiated neural cell line.

(3) The development of a cheap, biocompatible alternative to quantum dots for nanosensor and imaging applications. We utilized a positively charged co-matrix to promote the encapsulation of free sulforhodamine B in silica nanoparticles, a departure from conventional reactive dye coupling to silica matrices. While other methods have been invoked to trap dye not directly coupled to silica, they rely on positively charged dyes that typically have a low quantum yield and are not extensively tested biologically, or they implement reactive dyes bound to larger encapsulated molecules.

Chapter 1

Diagnostic and therapeutic nanotechnologies with applications to the retina and optic nerve

Abstract

Nanoengineering refers to the design, engineering and selective manipulation of materials and devices at the nanoscale, or the level of individual molecules and even single atoms. Nanotechnology is the practical consequence of nanoengineering and its implementation. Nanoscale materials tend to acquire new properties distinct from their bulk counterparts or constituent building blocks, which can result in unique responses to electromagnetic fields or high chemical sensitivity, resulting in the ability to detect very slight changes in surrounding media. Biologically, the size of nanodevices facilitates cellular internalization and can minimize structural interference with intracellular activities and processes if designed and used correctly. Here we review various recent nanotechnologies that have been applied or are of particular relevance to the neural sensory retina and optic nerve. We discuss functionalized nanoparticles for molecular sensing and diagnostics, focusing on cellular imaging and molecular detection, and nanotherapeutic technologies, with particular attention to nanoparticle treatements and drug release systems.

1.1 Introduction

Conceptualizing the nanoscale is difficult; nine orders of magnitude separate it from the macro world associated with the meter, and three orders of magnitude from the familiar micron scale. To give a feel for this, consider that a 75-year lifespan equates to a 2.4-second nano-life, and a nano-United States would be just 9600 m^2 or about 2.4 acres [1].

A comprehensive treatment of nanotechnology applied to the nervous system and neural structures is beyond the scope of a single review. As such, we have focused on recent work aimed at sensing molecular and cellular function (nanodiagnostics) and nanotherapeutics relevant to the neural retina and optic nerve. Interested readers are directed to other reviews that discuss nanotechnology applied to the central nervous system and neuroscience more generally [2-6].

1.2 Functionalzied nanoparticles for molecular sensing and diagnostics

1.2.1 Cellular imaging

A considerable amount of work focuses on the use of nanoparticles for neuroimaging, both clinically and as a research tool for investigating cell biology and disease mechanisms. On the research side the use quantum dots (QDs) in particular allows investigators to make observations and measurements at sub-cellular levels with spatial resolution not previously possible. QDs are typically semiconductor nanocrystals on the order of 10 nanometers in diameter, and are often capped with polymers for bioconjugation and enhanced biocompatability (Figure 1.1). The particles exhibit extremely narrow emission peaks (tens of nanometers)

that can be tuned across the visible spectrum, as well as into the ultraviolet (UV) and infrared (IR), while maintaining broad absorption spectra that increase into the UV. This permits the excitation of many distinct QDs with a single source wavelength. QDs provide extremely high signal-to-noise ratios and exhibit photostability nearly 100 times greater than traditional fluorophores (i.e. they do not photobleach as quickly). Furthermore, individual QDs are bright enough to be resolved with conventional microscopic techniques [7]. These qualities have encouraged a wealth of research exploring the use of QDs in cell biology, including within the contexts of neurobiology and ophthalmology.

Winter et al. conjugated IgG secondary antibodies and specific RGD sequences to QDs in order to target integrins expressed in neuroblastoma blood vessels. The IgG-QD conjugates bound to primary integrin-specific antibodies, while the RGD-QD particles were directly recognized by integrins [8]. Pathak et al. optimized protocols for specific labeling of neural cells, and produced detailed cellular structural images of neurons and glial cells using antibody-conjugated QDs (see Figure 2 in [9]) [9,10]. More recently, the same group showed the utility of their methods for analyzing glial scar in a rodent model of retinal degeneration [11].

The work of Dahan et al. presents the utility of single QD resolution with optical microscopy. The group was able to track individual glycine receptors on cultured spinal cord neurons. Using various forms of image analysis, they were able to identify distinct receptor diffusion domains and diffusion coefficients that defined distinct synaptic, peri-synaptic, and extra-synaptic regions of glycine receptor clustering. Interestingly, follow-up electron microscopy (EM) of the same preparations provided exact receptor localization that complimented their optical imaging. This was possible using silver enhancement of the QD heavy metal cores

EM [12].

In a similar application, Cui et al. tracked the transport of nerve growth factor (NGF) along axons of rat dorsal root ganglion cells in culture. When incubated with retinal ganglion cells, NGF-QD conjugates were internalized in endosomes at axon terminals and directed towards the cell body at ∼1.3um/s. QD photostability enabled long term observation and the detection of frequent pauses in endosomal motion. The observation of simultaneous pauses in local regions indicated the possible influence of the local cyto-structure in trafficking. Additionally, the authors determined that the majority of endosomes contained single NGF-QD conjugates (i.e. a single NGF dimer) [13]. This was possible because single QDs blink randomly when observed with optical microscopy, but the effect gets masked in clusters.

Jayagopal et al. exploited QDs in vivo using different antibody-QD conjugates with distinct emission spectra in concert to monitor cell adhesion molecules (CAMs) in rat retinal endothelium from both normal and diabetic retinas. Functionalized QDs targeted PECAM-1, ICAM-1, and VCAM-1 in vivo using fluorescence angiography, and showed that diabetic rats expressed increased levels ICAM-1 and VCAM-1 with no appreciable changes in PECAM-1. In the same study, these authors labeled endogenously circulating and adherent leukocytes using RP-1 and CD45 antibody-QD conjugates in diabetic rats and rats with uveitis. Both models exhibited leukocyte rolling and leukostasis in capillaries. The findings were confirmed through analysis of retinal whole mounts of the same preparations [14].

Although chemically functionalized QDs are particularly promising for high resolution fluorescent imaging, other nanoparticles have also been used for this purpose. For example, 80 nm silver nanoparticles were used to image the sensory

retina. The nanoparticles were immersed in a solution of dextran-conjugated Oregon Green 488 or rhodamine, relying on nonspecific adsorption to load them with dye. A modified gene gun fired these particles over retinal whole mounts, staining cells through to the photoreceptor layer, while maintaining 98%viability [15].

A number of nanoparticle-based approaches may also enhance optical coherence tomography (OCT) of the retina [16]. Engineered nanoparticles can cause additional absorption, reflection, and internal scattering, thereby increasing OCT image contrast. Lee et al. described the use of oil-filled microspheres to this end [17]. These spheres were 0.2-15 μm in diameter with 50 nm shells incorporating melanin, carbon, or gold nanoparticles in bovine serum albumin (BSA). All particles exhibited absorption and scattering cross-sections on the order of 10-8 cm2. As a proof of concept, the gold-containing spheres were injected into mice ($\sim$8.5x106 spheres). Clearance of particles occurred through the liver, and a marked difference in OCT images was visible between livers with and without contrast agent. Cang and colleagues [18, 19] explored the use of gold nanocages as an alternative contrast agent. The 35 nm cages exhibited strong absorption of near infrared light, useful for deep tissue penetration. The scattering and absorption cross-sections were roughly 1.6x10-11 cm2 and 1.1x10-10 cm2, respectively (comparable to the microspheres when compared to actual cross-sectional area). Moreover, their smaller size could permit more efficient delivery, and the natural affinity of thiols for gold surfaces provides a simple route for bioconjugation. Exploiting this for targeted delivery to desired subpopulations of cells could significantly improve OCT diagnostic capacity.

Magnetic nanoparticles (MNPs) can provide contrast enhancement to OCT, as well, but through a different mechanism. By modulating an external magnetic field, Oldenburg et al. vibrated iron oxide nanoparticles to produce periodic

changes in local light scatter. By comparing the spatial variations in OCT signal amplitude they were able to pinpoint particle locations and differentiate, in vitro, between macrophages that incorporated particles and those that failed to do so [20]. Other recent work applied this magnetomotive OCT (MMOCT) to silicone tissue phantoms and excised rat mammary tumors. MNPs were detectable at concentrations as low as 27 μg/g, and tumors immersed in saline solution at 4 mg MNP/g displayed visible signal within 15min [21].

1.2.2 Molecular detection

In addition to imaging applications, nanotechnology can provide highly sensitive detectors with great potential for research of the retina and optic nerve. Conceptually, these nanosensors are relatively simple: they generate some measurable response dependent on the presence of another factor, either chemical (i.e. an ion or molecule) or physical (e.g. an applied voltage). The most prevalent of these devices rely on changes in fluorescence spectra, often involving forms of resonance energy transfer (RET) in nanoparticle or protein-based systems. Shifts in surface plasmon resonance (SPR) of gold and silver nanoparticles are also frequently exploited (Figure 1.2). In systems based on RET, a fluorescent donor is excited by a source wavelength of light. This excitation energy can then be non-radiatively transferred to another molecule or particle (acceptor) that absorbs in the emission spectrum of that donor. The distance and angle between the donor and acceptor determine the efficiency of transfer, and these parameters are made to vary in the presence of the desired factor [22, 23]. Contrary to RET, surface plasmon resonance does not require a donoracceptor pair. The metal nanoparticle has a distinct spectral peak at which incident light is absorbed and later reemitted or dissipated thermally. This peak depends greatly on the conditions at the particle surface

(specifically the dielectric constant), and hence can be shifted by nearby molecular interactions. SPR can be measured directly or used to enhance the fluorescence of acceptors excited by the SPR spectrum of a given NP [24].

For protein-based systems applicable to ophthalmic research, genetically encoded sensors (GESs) offer a powerful way to track cellular activity in vivo and in situ. One major advantage of these devices is their ability to report cellular activity throughout the cells lifetime without repeated application of externally synthesized particles [25-39]. A particularly important class of GESs, developed through the efforts of a number of labs, notably Roger Tsiens, exploits the activity of calmodulin (CaM). These GESs detect calcium (Ca^{2+}) and come in two flavors: single fluorophore-based and Frster RET (FRET)-based (Figure 1.2). The single fluorophore sensors use cyclically permuted green fluorescent proteins (GFPs) with internal CaM sequences (Camgaroo, G-CaMP, and Pericam). Changes in CaM conformation distort protein structure and alter fluorescence. The FRET sensors (called Cameleon sensors) include two engineered GFPs separated by a linker domain of CaM and a modified M13 domain of myosin light chain kinase. Sufficient Ca^{2+} causes CaM to bind the M13 domain and shift the relative positions of the fluorophores, thereby perturbing FRET efficiency. The most robust system (version D1) yields a dynamic range of 0.1 μM to 1 mM ($K_d \sim 70$ μM). It is important to note that CaM interacts with many neuronal proteins, and though modifications to the incorporated domains should limit cross-talk, such problems may still arise [25-29].

Oliver Griesbeck and colleagues developed troponin C (TnC) Ca^{2+} sensors as an alternative to CaM-based ones. TnC is not known to interact specifically with other proteins endogenous to neurons, and hence is preferable to CaM. In TnC-based sensors, the presence of Ca^{2+} induces a conformational change in TnC,

reducing the distance between cyan and yellow fluorescent proteins (CFP and YFP) (Figure 1.3). The best of these sensors are effective above $\sim$0.5 μM Ca^{2+} and saturate at 100 μM ($K_d \sim 2$ μM) [30-32].

Genetic encoding has also been used to create voltage sensors (Figure 1.4). The first such sensor was a simple gene fusion between GFP and a modified (non-conductive) Drosophila Shaker K^+ channel protein, called FlaSh. An improved sensor called VSFP1 relies on the voltage-dependent conformation of the S4 domain of another voltage-gated K^+ channel, Kv2.1, to alter FRET efficiency between fused CFP and YFP. Another improved sensor, SPARC, has GFP fused internally to rat skeletal muscle sodium (Na^+) channels. Fluorescence increases rapidly in milliseconds following the depolarization of a cell for both sensors, but the resulting shifts are only $\sim$1%. Mammalian cell expression is also poor, which makes these sensors difficult to employ effectively [33-37].

Current work is taking advantage of voltage-sensitive domains that maintain their function in the absence of other transmembrane domains and without multimerization, providing more compact sensors. Reducing the gene length can increase the production rate and decrease the load on the cell, allowing for better expression. It also avoids the issue of fluorescence inhibition due to collisions with other subunits. In particular, ciona intestinalis voltage-sensor-containing phospatase (Ci-VSP), which is not an ion channel, is homologous to the voltage-sensitive domain of the Kv channel, but monomeric. Being of heterologous origin, it may also avoid post-translational modifications that would inhibit membrane expression [36, 37].

Chloride (Cl^-) ion GESs have also been developed. While less commonly studied, chloride is also critical to neural systems as GABAergic and glycinergic synapses operate with Cl^--selective channels. The most current instantiation of

such a sensor, developed by Markova et al., operates under the same principles as other FRET GESs, but with CFP and YFP linked by a Cl^--sensitive domain [39]. This GES is an enhanced version of its predecessor, Clomeleon [38,39]. The dynamic range is roughly 5-100mM Cl^- [39].

Genetically encoded sensors have the benefit of many years of evolution behind their engineering. However, proteins are unstable and subject to degradation in biological systems; to perform efficient long-term studies, GESs have to be expressed in the cells of interest. Inserting genes is no always a viable option, so durable nanoparticle counterparts to these genetic devices are needed. Progress is being made, but further development is necessary. Efficient nanoparticle voltage sensors have yet to be developed and calcium sensors have received minimal attention. Some work with CaM bound to silver exhibited Ca^{2+}-dependent SPR shifts, but these were only 2 nm in the presence of 2 mM Ca^{2+} and occurred over tens of seconds [40].

Non-calcium nanoparticle ion sensors, however, do exist. A potassium (K^+) sensor, developed by Lin and coworkers used gold nanoparticles conjugated to 15-crown-5 ethers. K^+ formed a complex with two of these ethers causing functionalized particles to aggregate. This aggregation resulted in an SPR shift that produced a visible color change [41]. C. Y. Chen and colleagues applied this concept to FRET-interacting QDs; the presence of K^+ resulted in FRET exchange. K^+ at $\sim$1.7 mM resulted in $\sim$2.5-fold increase in the acceptor-donor fluorescence ratio [42]. Still, both systems have limitations: they require a freely diffusing multi-particle environment which limits their spatiotemporal resolution and excess Na^+ prevents aggregation, thereby cloaking the presence of K^+ [41, 42].

A few other sensors also deserve mention in the context of neural and retinal research. Prow et al. developed an oxidative stress sensor by conjugating MNPs

with specific transcriptionally activated PCR products (TAPs) (Figure 1.5). The TAPs coded for enhanced GFP (eGFP) under control of an enhanced antioxidant response element (ARE). The particles were coated with lipofectamine and transfected into retinal endothelial cells. Cells under oxidative stress activated transcription of ARE-driven genes, increasing fluorescence in transfected cells; the number of cells expressing GFP increased $\sim$20% under stress [43]. This research was extended to in vivo sensing in rats [44]. Oxidative stress in rat retinas was compared between normal and diabetic rats. Diabetic retinas displayed visibly greater GFP expression 3 days after subretinal injection. The group acknowledged the potential for incorporating genes for proteins that scavenge reactive oxygen species (ROSs), which are particularly damaging to photoreceptors.

Another interesting sensor was developed for amine-containing neurotransmitters like dopamine. Radu and coworkers developed this sensor using mesoporous silica nanoparticles (see Figure 2 in [45]). The particles were coated with poly(lactic acid) (PLA) and the walls of the pores were lined with *o*-phthalic hemithioacetal (OPTA). OPTA reacts with amine containing molecules to produce a fluorescent product. The PLA acted as barrier to limit what molecules could pass, and the coating was used to distinguish between dopamine and glutamate, reducing their reaction rates by a factor of 4 and 57, respectively at pH 7.4 [45]. The system was not specific, though: any small amine with limited negative charge could penetrate the particle and react.

1.3 Nanotherapeutic technologies

1.3.1 Nanoparticle-based release systems

Nanotechnology has also found many therapeutic uses, particularly in the transport and release of drugs, genes, and even cells. Many nanoparticles are easy to conjugate and possess a large reactive surface. This enables their development and use in targeted systems, using antibodies or receptor ligands, for example. Nanoparticle systems can be engineered with different internal and external properties, permitting the transport of hydrophobic materials in aqueous environments. They can stabilize drugs in vivo, making them more potent. Nanoparticles can be designed for long residence times and degradation rates in the body, tailoring their clearance. Furthermore, their tiny size provides for efficient systemic administration. The enormous potential in neuromedicine alone has generated too much literature for a single review. Here, we limit our discussion to promising approaches relevant to ophthalmic research (Figure 1.6).

1.3.2 Small molecule and protein delivery

Nanodelivery of drugs has been investigated for a number of ophthalmic disorders including cytomegalovirus (CMV) infection, diabetic retinopathy, uveitis, uveoretinitis, age-related macular degeneration (AMD), and various forms of cancer. For CMV, Merodio et al. explored albumin nanoparticles for delivery of ganciclovir (GCV). Rats injected intravitreally with 25 μg of free drug displayed increased vasodilation and slight inflammation one week post-injection, while no negative responses were observed for equivalent nanoparticle doses. Particle safety was further confirmed through a lack of autoimmune uveoretinitis; retinal sections stained for arrestin and rhodopsin, associated with the disorder, showed no change

in expression. Additionally, it particles were found to sustain release over ten days, at which point 40% of the drug remained. Release was not constant, though, as 40%was released within the first hour [46].

Adibkia and colleagues created methylprednisolone acetate (MPA) loaded nanoparticles to mitigate endotoxin-induced uveitis. The Eudragit® RS100 polymer nanoparticles, ∼300-600 nm in size, were tested in vitro and found to release 60-70% of encapsulated MPA at a relatively constant rate from hours 2 through 12, with essentially all drug released by 12 hours. Particles were administered in vivo to rabbits with lipopolysaccharide (LPS)-induced uveitis as 20 μL eye drops at 0.5% MPA, with 3 drops given over 12 hrs. Both nanoparticles and MPA alone showed significant reduction in inflammation over a 36 hr period of observation, but nanoparticles produced a statistically more dramatic effect. Additionally, leukocyte counts in aqueous humor were significantly reduced with the nanoparticle treatment (∼200/μL) relative to free MPA (∼1200/L) or untreated controls (∼1700/L) [47].

Eudragit® polymers have also been used to encapsulate gliclazide, a second generation hypoglycemic drug, for use in diabetic retinopathy. Eudragit® L100-gliclazide (EuLG) and Eudragit® RSPO-gliclazide (EuRG) nanoparticles were prepared. Optimal process conditions yielded 520 nm EuLG nanoparticles with 90% encapsulation efficiency (fraction of total drug encapsulated) and 66% drug loading (amount of drug relative to particle mass), and 120 nm EuRG nanoparticles with 96% encapsulation and 56% loading. Experiments were performed on streptozotocin-induced diabetic rats. After oral administration of glucose (2g/kg), EuLGs reduced serum glucose levels by as much as 53% relative to controls. Performance was significantly better than both free gliclazide (∼30%) and EuRG treatments (∼33%). All gliclazide formulations (1.33 mg/kg) showed significant

glucose level reduction relative to controls during the first 6 hrs after glucose administration [48].

For uveoretinitis, two different systems have been developed: Tamoxifen (TAM)-loaded and betamethasone phosphate (BMP)-loaded nanoparticles. De Kozak et al. encapsulated TAM in poly(ethylene glycol-co-hexadecyl cyanoacetate) (PEG-PHDCA). The ∼112nm particles were injected intravitreally in rats with a total TAM dose of 0.25 μg. Rats presented experimental autoimmune uveoretinitis (EAU) induced by arrestin and Mycobacterium tuberculosis H37Ra.l. Nanoparticles were observed in the retinal pigment epithelium (RPE) by three days post-injection (17 days after EAU induction), throughout which time clinical EAU scores were significantly reduced. At the end of this timeframe, nanoparticle-treated rats scored <2.5, while no-treatment contols and those treated with free TAM (0.20 μg) scored ∼3.5 [49].

The BMP system was produced by Sakai and coworkers and consisted of PLA nanoparticles also used to treat EAU rats; however, administration was by tail vein injection. Histological analysis of retinal slices indicated that structural integrity of untreated retinas was visibly compromised, while BMP treated retinas maintained cytoarchitecture. Clinical EAU scores reached a maximum of ∼4 by day 17 in untreated rats. Nanoparticle treatment (100 μg BMP) or treatment with 500 μg free BMP produced scores of ∼2. Free BMP at 100 μg showed little effect [50].

Another glucocorticoid, dexamethasone (DM), has been transported by multiple different nanocarriers. Xu and coworkers created DM acetate poly(lactic-co-glycolic acid) (PLGA) nanoparticles ∼250 nm in diameter with ∼52% DM encapsulation. DM release in vitro was completed over 40 days in two relatively linear regimes, 45% occurring during the first 10 days and the remaining 55%

over the following 30. Nanoparticles were injected intravitreally in rats with laser-induced choroidal neovascularization (CNV). A 100 μg particle dose showed an initial jump in DM concentration day 1 to roughly 8 mg/L. This declined to 2-3 mg/L by day 7, where it remained until day 28. Other dosages followed the same basic pattern. Fluorescein fundus angiography of control rats showed leakage in $\sim$65% of CNV lesions on days 14 and 56, while treated rats showed leakage in 28% and 25%, respectively. A 400 μg nanoparticle treatment reduced leakage below 8% for both days. Lesion site thickness, inferred from eosin and hematoxylin stained slices, was also significantly reduced by nanoparticle injection [51].

Hashida et al. developed liposomal carriers for DM. These were a collection of phospholipids, glycosphingolipids, cholanic acid, and cholesterol crosslinked to human serum albumin (HSA). The HSA patches were modified to present Sialyl Lewis X (SLX), which targeted liposomes to P and E-selectin. These selectins are over-expressed in vascular endothelial cells during inflammation. Liposomes were injected intravenously into EAU and control mice. Only SLX-bearing liposomes targeted retinas, and this targeting was much more extensive in EAU mice. Target confirmation was obtained through injection of anti-P and anti-E-selectin antibodies, which significantly reduced retinal localization. Retinal DM concentrations in EAU mice treated with liposomes (total of 2 μg DM) were $\sim$14 ng DM/mg wet tissue, while only $\sim$7 ng/mg in those treated with 1mg of free DM. Free DM was present at higher concentrations in other tissues, whereas liposome-delivered DM was only detectable in the eye and liver (1.4 ng/mg). RNA analysis determined EAU to be mediated comparably by the 2 μg DM liposome treatment and the 1mg free DM treatment [52].

One of the most intensively researched topics in ophthalmic medicine is the arresting and reversing of neovascularization, and nanodelivery has been employed

to this end. Hammady et al. encapsulated endostatin and paclotaxel in PLA particles conjugated to a synthetic analog of SLX (sSLX). The nanoparticles were ∼220 nm with optimal loading efficiencies of ∼73% for endostatin (at 1.5 μg/mg polymer) and ∼80% for paclitaxel (at 40 μg/mg). Testing in vitro was performed with human umbilical vascular endothelial cells (HUVECs). Experimental populations were incubated with LPS to induce angiogenic behavior. Quantification of particles in cell lysates confirmed the targeting ability of sSLX; endocytosis increased greater than 3-fold for functionalized nanoparticles in the presence of LPS. Without LPS, this increase was only ∼20%. HUVEC proliferation was not affected by unloaded nanoparticles, but inhibited by drug-loaded nanoparticles. Nanoparticle inhibition was significantly greater than that of free drug [53].

Chitosan nanoparticles have been used for a similar purpose. Kim and coworkers created 5 cholanic acid-modified glycol chitosan nanoparticles (∼200nm) doped with short RGD peptide sequences. Anti-angiogenic activity was examined by vascularization of a Matrigel® mixture injected into the backs of mice. Angiogenesis was induced by application of bFGF (500 ng/mL), and RGD treatments were applied at ∼100 μg/mL. Gel hemoglobin content was analyzed after 10 days to determine vascularization. Free RGD reduced 540 nm absorbance ∼50%, while nanoparticles reduced absorbance ∼70%. B16F10 tumor-bearing (100 mm^3) mice were administered an intratumoral RGD dose of 10 mg/kg 20 times over 8 days. Day 12 tumor volumes for were 7000 mm^3 for controls, 4500 mm^3 for free peptide treatment, and 2500 mm^3 for nanoparticle treatment. Angiogenic behavior, assessed by CD31 expression in tumor blood vessels, was suppressed nearly 80% for nanoparticles, while <60% for free peptide [54].

The wide use of photodynamic therapy (PDT) to treat neovascularization has prompted a fair amount of nanoresearch, as well. Visudyne®, which

is FDA-approved, is a liposomal system that carries the photosensitizer (PS) verteporfin. Oxidative degradation of the liposome occurs during light exposure, releasing ROSs produced by excitation of verteporfin. A more advanced system was composed of 1,2-bis[10-(2,4-hexadienoyloxy)decanoyl]-sn-glycero-3-phosphocholine (bis-SorbPC), other phospholipids, poly(ethylene glycol) (PEG)-modified lipids, and cholesterol. The bis-SorbPC could be cross-linked under UV irradiation, which destabilized the membranes, separating the PEG lipids from the bis-SorbPC and forming regions of micellar structure. Complete bis-SorbPC crosslinking yielded a release rate of $\sim$0.1%/sec for encapsulated 8-aminonaphthalene-1,3,6-trisulfonic acid (ANTS) [55, 56].

1.3.3 Gene and oligonucleotide delivery

The eye has recruited much attention with regard to gene and oligonucleotide delivery, due to a number of relevant diseases and an ease of access and observation. As nanocarriers can be applied similarly in this field, a fair amount of research has been dedicated to this. As a proof-of-concept for one system, Naash and colleagues transfected mice with DNA nanoparticles formed from a mixture of GFP-plasmid DNA and N-terminal cysteine polylysines (30-mers) conjugated to 10 kDa PEG-maleimides (CK_{30}PEG10). The DNA interacted electrostatically with the polylysines to produce PEG-capped nanorods with DNA/polylysine cores. The presence of acetate counter-ions produced elongated rods with <8nm diameters (AcNPs), while trifluoroacetate produced compact ellipsoids with <18nm minor diameters (FAcNPs). Mice were given intravitreal injections of nanoparticles or naked plasmid (both 0.6 μg DNA). Quantitative reverse transcription-PCR (qRT-PCR) two days later revealed nanoparticle transfection to be significantly more pronounced than naked plasmid: $\sim$1000-fold in the lens, and 10-100-fold

in the retina. Equivalent sub-retinal injection directed most expression to the retina: ∼1000-fold that of naked plasmid. For both injection methods, only AcNPs were able to penetrate much distance into surrounding tissue. Electroretinography (ERG) of experimental and control eyes 30 days after injection suggested no long term damage or toxicity from treatment [57].

The Naash group extended use of the CK_{30}PEG10 system to target the retinal degeneration slow (rds) gene, associated autosomal dominant retinitis pigmentosa (RP). The goal was to supplement RDS expression in rds+/- mice to prevent characteristic photoreceptor degeneration. Treatment consisted of 0.92 μg DNA (nanoparticle or free plasmid) injected sub-retinally in mice at postnatal day 5. The RDS cDNA was provided under two different promoters: chick -actin (CBA; ubiquitous) and interphotoreceptor retinoid-binding protein (IRBP; photoreceptor-specific). Expression was determined by qRT-PCR of whole eye mRNA. On day 2, expression of normal RDS mRNA was significantly greater for nanoparticle treatments, a factor of 3-4, while expression was unaltered in saline and free plasmid controls. This enhancement reduced to around 2-fold by day 30, but was maintained at this level over 120 days of observation. Sizeable increases in rhodopsin and S-opsin expression (∼4 and 2-fold, respectively) were also observed on day 30, suggesting potential phenotypic rescue. ERG response amplitudes were significantly increased for nanoparticle treatments through day 30. Plasmids under IRBP promoter control maintained this significance through day 120. Improvements in outer segment (OS) shape and orientation were also observed in retinal slices of nanoparticle-treated mice (see Figure 5 in [58]) [58].

Dos Santos et al. tested an alternative DNA nanoparticle for anti-TGF-2 activity. Cationic polyethylenimine (PEI) was used to compact TGFβ-2 antisense oligonulceotide. The system was intended for diseases associated with excessive

glial proliferation, like vitreoretinopathy. The most promising constructs were studied in vitro with rat Müller cells (RMCs). Nanoparticles were observed in 70% of cells after 6 hours of incubation in 200 nM particle solution. Cell viability was only reduced to 90%, but proliferation was affected dramatically. The number of viable treated cells at 72 hours was <50% of the controls, amounting to <3-fold increase in cell number. RT-PCR confirmed significant reduction in TGFβ-2 mRNA, ∼40% less than untreated cells and ∼20% less than naked DNA controls. Nanoparticle-treated cells expressed <50% of the TGFβ-2 present in controls. Treatment was also examined in rats via intravitreal injection of 500 pmol of compacted DNA tagged with FITC. Naked DNA was no longer detectable after 24hrs while nanoparticles were still present after 3 days. At this point they primarily colocalized with glial cells at the inner limiting membrane [59].

Yun Mo and coworkers encapsulated genes for superoxide dismutase 1 (SOD1) and enhanced YFP (eYFP) in albumin nanoparticles. SOD1 functions to reduce oxidative stress, and could provide a generic therapy for a number of retinal diseases, including uveitis, diabetic retinopathy, and AMD. Optimal formulations produced ∼120nm particles with ∼80% efficiency. These nanoparticles maintained relatively constant release in vitro over the course of 6 days after an initial burst release of ∼20%. In culture with ARPE-19 cells, the particles were completely internalized at 0.1mg/mL (greater than transfection doses) and produced no toxic effect. Nanoparticle transfection of 1 μg DNA resulted in ∼85% of cells fluorescing. Lipofectamine® yielfded only ∼15% and naked plasmid was ineffective. Nanoparticle treatment with 5 μg DNA increased SOD activity ∼5.5 times, while the equivalent Lipofectamine® dose increased activity ∼4.5 times. Intravitreal injection of nanoparticles with 130 ng DNA yielded measurable protein expression in mouse retinas within two days. This disappeared by day seven,

though, indicating that optimization would be needed for long-term expression [60].

1.3.4 Nanoparticle treatments

In some cases, nanoparticles themselves can act as therapeutics. For instance, ceria nanoparticles act as antioxidants. These particles can be engineered with a large number of oxygen vacancies and switchable oxidative states, making them potent ROS scavengers with regenerable activity. In addition, their large surface area provides many active sites [61-63]. The McGinnis group showed these particles prevent the rise of ROSs in primary rat retinal neuron cultures and prevent vision loss in vivo from overexposure to bright light. Cultured neurons incubated at 5nM particle concentration for at least 12 hours exhibited a significant decrease, >50%, in hydrogen peroxide-induced ROSs. Retinal degeneration in vivo was assessed via outer nuclear layer (ONL) thickness. Six hours of 2700 lux exposure resulted in <20% thickness loss for rats treated intravitreally with 0.2 pmol of nanoparticles, while untreated loss was ∼50%. These doses salvaged >50% of ERG amplitudes, while untreated rats retained only ∼25% [63].

Other nanoparticle treatments can be used impede tumor and blood vessel growth [64-71]. The Kataoka group, for example, developed two 3rd generation poly(benzyl ether) functionalized porphyrin (DP) dendrimers for PDT. One was cationic ((+)DP) and the other anionic ((-)DP) (see Figure 1 in [65]). Both dendrimers were significantly less toxic under dark conditions than protoporphyrin controls. Under 90J/cm2 visible light irradiation, (+)DP was able to achieve 50% phototoxic cell death (LLC cells) at 0.047 μM (a dose with negligible dark toxicity), which was less than 3% of the necessary protoporphyrin dose. The (-)DP was less effective (50% at 36 μM) presumably due to electrostatic repulsion from the

cells [65]. To compensate, the authors incorporated poly(ethylene glycol)-block-poly(L-lysine) (PEGPL) as an encapsulant. This shielded the charge and promoted internalization, resulting in a 280-fold increase in phototoxicity, with no detectable increase in dark toxicity. This micellar system was administered in 0.6 mg doses via tail vein injection to rats with laser-induced CNV. Both free (-)DP and micelles localized to CNV regions, but free dendrimer was cleared within 24hours, while micelles remained. PDT (50J/cm2) 15min post-injection provided no increase in lesion closure for free (-)DP relative to the controls (∼20-30%). However, PDT up to 4 hours after micelle injection yielded 70-80% closure. Skin phototoxicity of the micelles was compared to an equivalent (clinically used) formulation of FDA-approved Photofrin® 4 hours after injection. Micelles produced no macroscopic effect, while Photofrin® treatment resulted in visible tissue damage [66].

1.4 Discussion

Despite the diversity of nanoresearch, both in ophthalmology and other fields, certain trends are emerging. Nanotechnology has been evolving to more complicated multiplexed systems. The properties of individual materials are often not enough to provide the desired behaviors, and hybrid devices will likely dominate future research. The addition of targeting and membrane-penetrating molecules may be particularly prevalent: targeting contrast agents or QDs to angiogenic cells would improve neovascular imaging; targeting ion sensors to ion channels and neurotransmitter sensors to synapses would facilitate neuronal studies. This is even more critical for therapeutics. For example, photodynamic nanosystems should only be internalized by angiogenic or tumorogenic cells. This is particularly crucial for metastatic cancers, where intratumoral injection is not an option,

and CNV, where photoreceptor damage must be avoided. The incorporation of cell-penetrating peptides and polycationic peptides can promote delivery across cell membranes, which is necessary for most treatments to be efficient. Improved delivery amounts to lower therapeutic doses, which is cost-effective and reduces side effects.

Other trends are also emerging. In sensor systems, FRET has become the predominant form of reporting, given its ability to produce dramatic signal shifts with small conformational changes and the potential for ratiometric analysis. While genetically encoded FRET sensors will continue to improve, synthetic sensors will likely see the most attention, and much of this will probably be devoted to QDs given their favorable attributes. Nanosurface energy transfer (NSET) (Figure 1.2), which relies on metal nanoparticle acceptors (e.g. gold or silver), may see greater use as well. While it does not permit ratiometric analysis, it functions over greater distances than FRET, making it particularly useful for large QDs (red and IR-emitting). The stability of the metal acceptor also complements a QD donor, permitting long visualization time frames. Moreover, NSET may be used to enhance FRET distances by acting as an intermediary between donor and acceptor fluorophores, which is certain to be exploited, as it retains the ratiometric property of FRET and gains the functional range of NSET [22, 23].

As for nanodelivery, the extensive array of nanovehicles will probably narrow and homogenize as approaches become standardized. Generic transport vessels, like liposomes and polymer micelles will probably remain popular. They combine biocompatibility with the ability to encapsulate many different types of drugs. Their manufacture is often facilitated by self-assembly, and they can be tuned to degrade at different rates by varying component ratios and crosslink densities. Additionally, their surfaces can often be easily modified to enable tar-

geting and improved (or diminished) cell penetration and protein binding. PEG and PLGA will probably maintain their prevalence in such systems as component polymers due to their versatility and availability. The use of temperature-sensitive poly(N-isopropyl acrylamide) (pNIPAAm) and other environmentally-responsive polymers may also become more popular, permitting controlled release under specific conditions.

The remarkable success of cationic polymers (particularly CK_{30}PEG10) in compacting and transfecting DNA suggests their continued development and application in gene delivery. In a similar vein, there may be development of biostable vesicles that house and protect their own genomes while taking advantage of host cell machinery. Such systems could provide stable therapeutic activity while isolating their DNA from the host. This would permit subsequent removal, if treatment needed to be modified. One could imagine this being achieved through activation of genes for vesicle-degrading enzymes or DNAses to destroy transfected sequences.

Gold nanoparticles and MNPs will also see further use, given their biocompatibility and versatility. In addition to uses already discussed, for example, the application of magnetic nanoparticles to retinal tissue engineering is a nascent concept being explored by several investigators. With appropriate external fields, MNP-loaded cells may be manipulated to achieve tissue architectures and cell densities difficult for conventional scaffold technologies [72, 73]. Self-assmebling peptide nanofiber scaffolds (SAPNS) will probably see increased application to tissue engineering and regenerative medicine, as well. Recent work has already demonstrated their potential for axonal regeneration [74, 75].

Ultimately, a combination of primary research and safety evaluation will determine which nanotechnologies reach the clinic. The retina and optic nerve are excellent strategic targets for such advanced systems, and although it remains

to be seen which technologies will have the highest impact, there exists a unique potential for the development of very novel approaches to detection, diagnosis, and treatment.

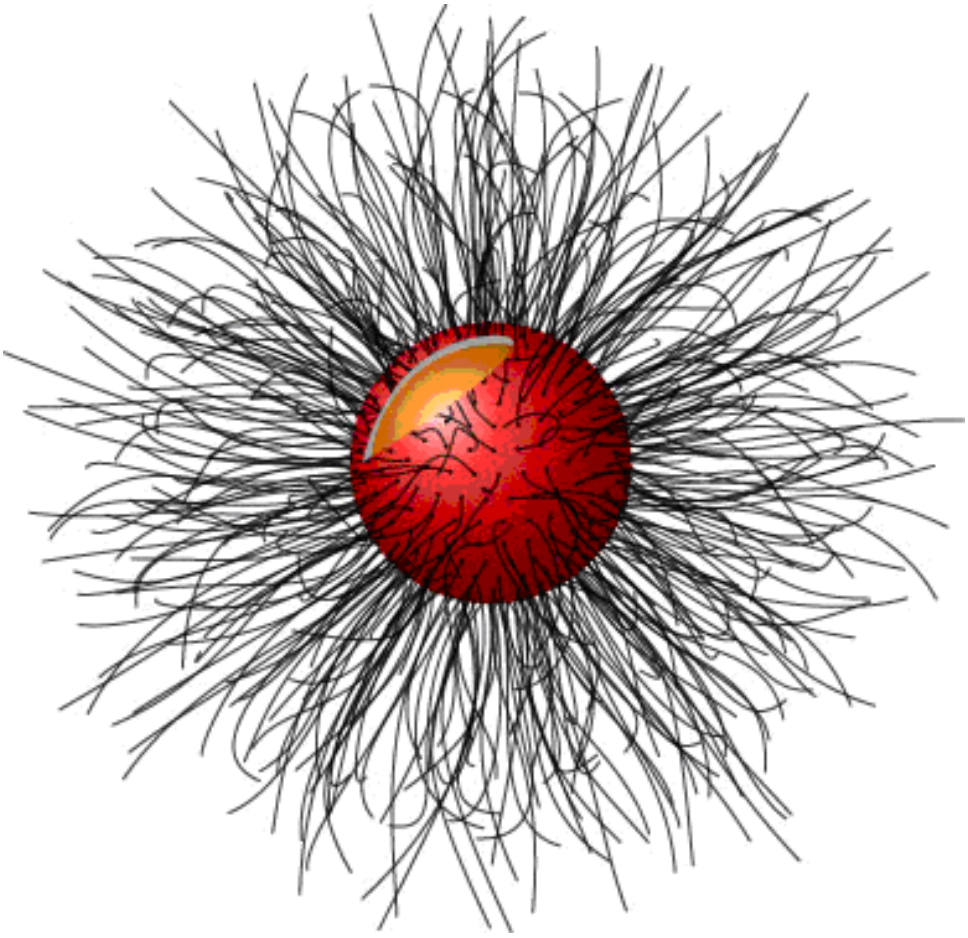

Figure 1.1: Typical quantum dot structure. The semicondutor nanocrystal core (orange) is coated with a second semiconductor shell (red), which helps to insulate the core from the environment. A third polymer layer (black) is often incorporated to further shield the QD, while providing biocompatibility and solubility. This layer may also simplify bioconjugation.

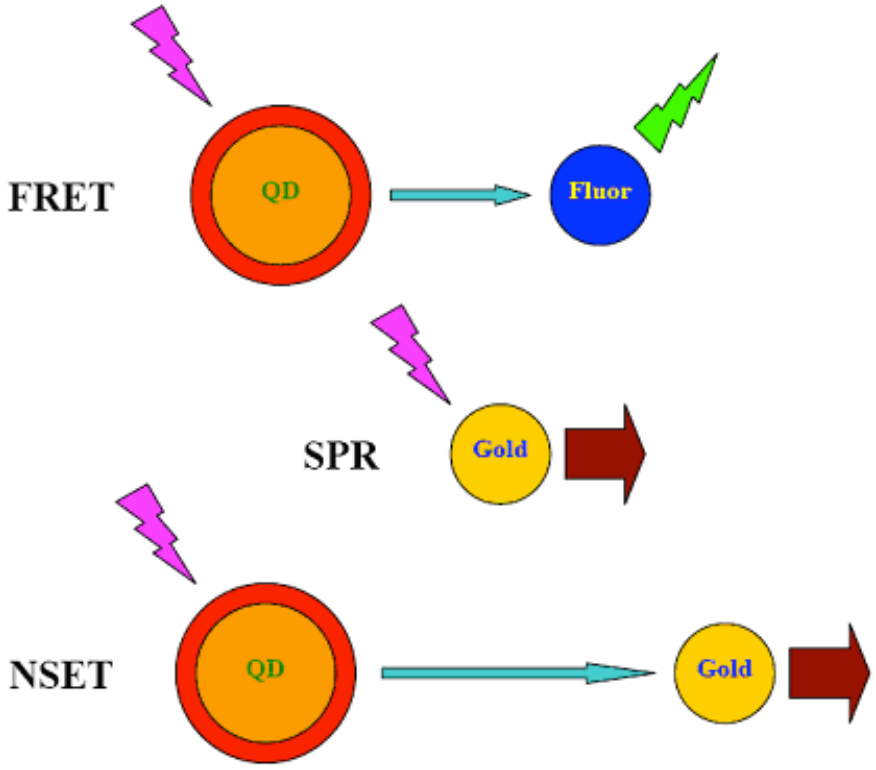

Figure 1.2: Energy transfer and plasmon resonance. In FRET, the donor QD absorbs a photon and transfers the energy to an acceptor fluorophore, which then emits a lower energy photon. In SPR, a metal nanoparticle absorbs a photon and typically dissipates the energy thermally. In NSET, QD donor energy is transferred to a metal nanoparticle and then dissipated as heat. NSET has a greater range than FRET due to the metal surface acting as a 2D array of dipoles.

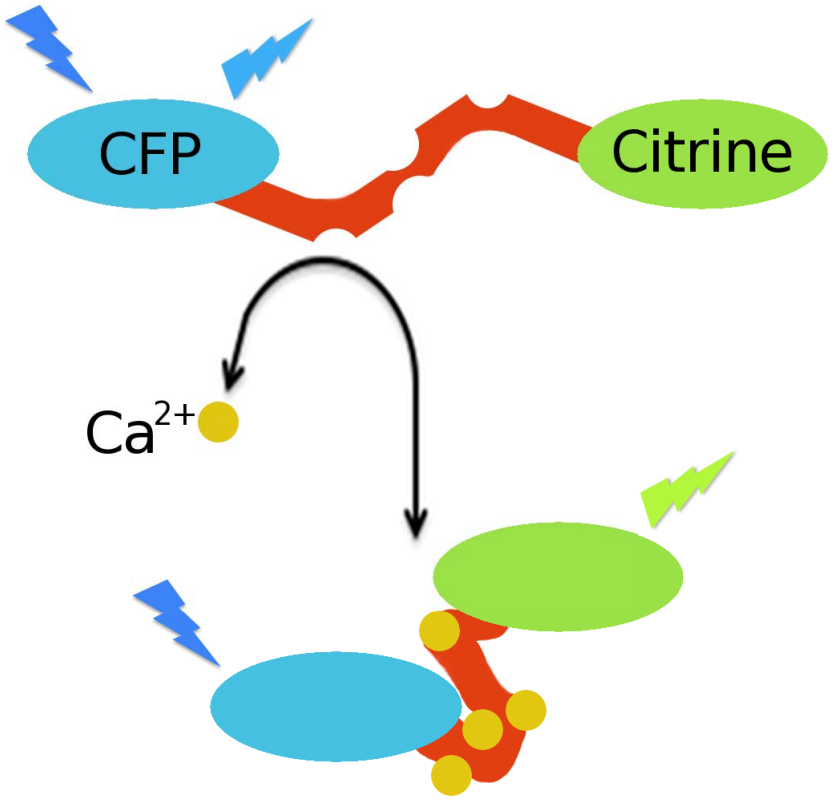

Figure 1.3: Schematic representation of the TnC-based sensor. In the absence of calcium, incoming 432nm light is absorbed by the CFP and emitted at 476 nm. After binding calcium, the troponin C undergoes a conformational change, enabling FRET between the CFP and Citrine. Incoming 432 nm light is absorbed by the CFP and emitted by the Citrine at 528 nm.

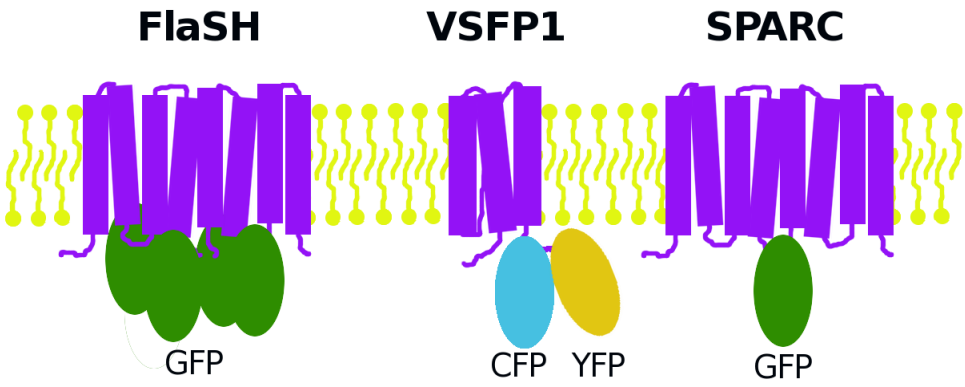

Figure 1.4: Illustration of the genetically encoded voltage sensors in bilipid membrane.

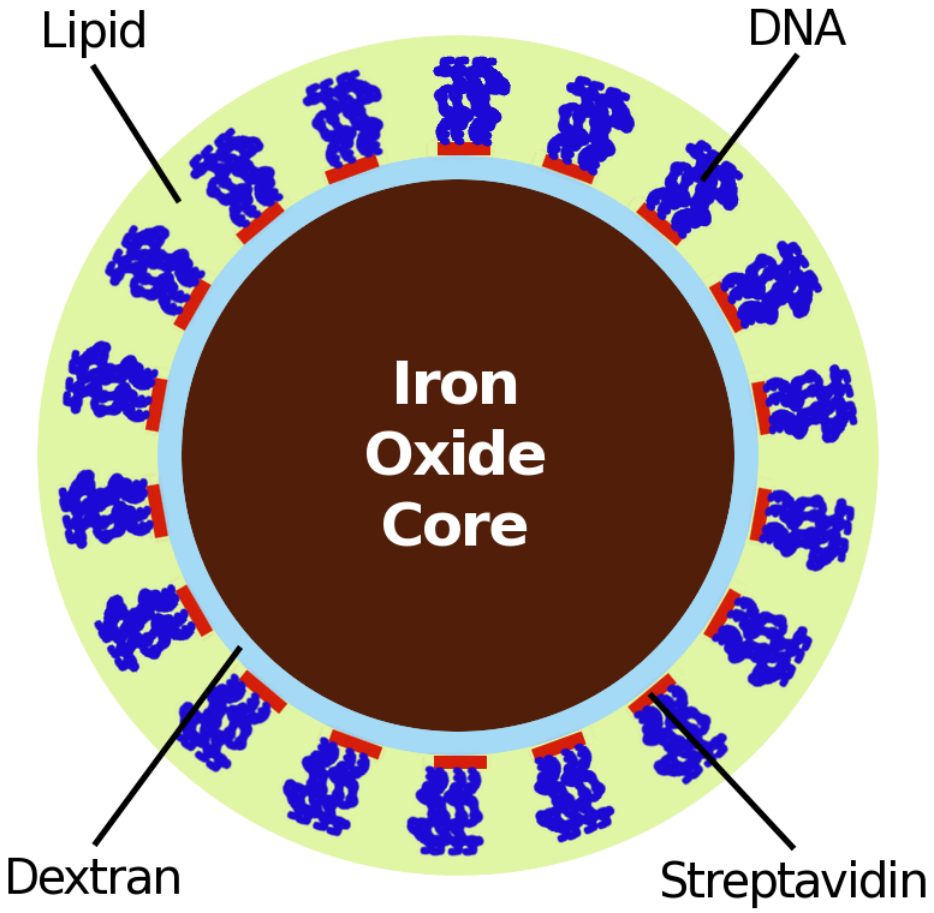

Figure 1.5: Illustration of a TAP-conjugated MNP coated with lipid.

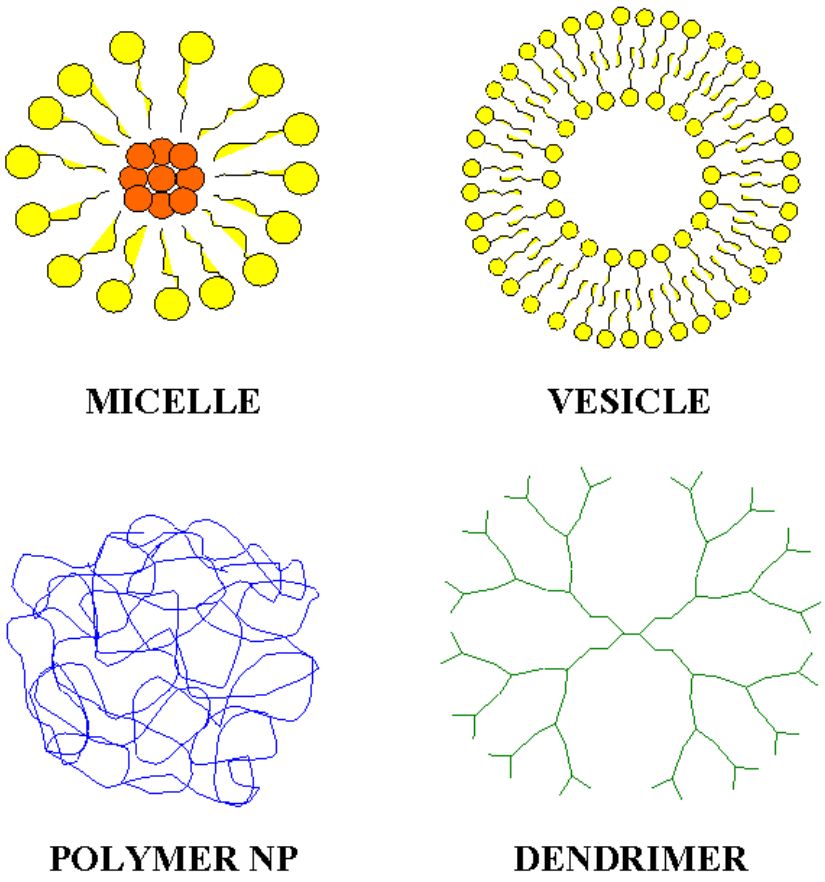

Figure 1.6: Nanodelivery systems. Micelles generally encapsulate hydrophobic drugs at their core, while the hydrophilic surface enables aqueous distribution. Vesicles can be polymer or lipid-based and typically carry an aqueous phase internally that is isolated from the external environment. Polymer nanoparticles can encapsulate hydrophobic or hydrophilic drugs depending on the subunits; often they are partially cross-linked to improve stability. Highly branched dendrimer molecules can interact electrostatically with loaded drug or possess hydrophobic cores for nonpolar loads, solubilized by charged or polar branch termini (or the presence of amphiphiles). Sizes typically follow this pattern: vesicle $>$ micelle $\approx$ polymer NP $>$ dendrimer.

1.5 Acknowledgments

This work was supported by NIH grant NS054736.

Chapter 1, in full, is currently in preparation for submission. Blumling, James P.; Silva, Gabriel A. Diagnostic and therapeutic nanotechnologies with applications to the retina and optic nerve. The dissertation author was the primary author of this material.

1.6 References

1. United Nations. Statistical Division. *Demographic yearbook. Annuaire dmographique*, 68-77, 2006.

2. GA Silva. Introduction to nanotechnology and its applications to medicine. *Surgical Neurology*, 61(3):216-220, 2004.

3. GA Silva. Nanotechnology approaches for the regeneration and neuroprotection of the central nervous system. *Surgical Neurology*, 63(4):301-306, 2006.

4. GA Silva. Neuroscience nanotechnology: Progress, opportunities and challenges. *Nature Reviews Neuroscience*, 7(1):65-74, 2006.

5. GA Silva. Nanotechnology approaches for drug and small molecule delivery across the blood brain barrier. *Surgical Neurology*, 67(2):113-116, 2007.

6. GA Silva. Nanotechnology approaches to crossing the blood-brain barrier and drug delivery to the CNS. *Bmc Neuroscience*, 9(Supplement 3):S4, 2008.

7. MA Walling, JA Novak, and JR Shepard. Quantum dots for live cell and in vivo imaging. *International Journal of Molecular Science*, 10(2):441-91, 2009.

8. JO Winter, TY Liu, BA Korgel, and CE Schmidt. Recognition molecule directed interfacing between semiconductor quantum dots and nerve cells. *Advanced Materials*, 13(22):16731677, Jan 2001.

9. S Pathak, E Cao, MC Davidson, SH Jin, and GA Silva. Quantum dot applications to neuroscience: New tools for probing neurons and glia. *Journal of Neuroscience*, 26(7):18931895, Jan 2006.

10. S Pathak, MC Davidson, and GA Silva. Characterization of the functional binding properties of antibody conjugated quantum dots. *Nano Letters*, 7(7):18391845, Jan 2007.

11. S Pathak, R Tolentino, K Nguyen, L DAmico, E Barron, L Cheng, WR Freeman, and GA Silva. Quantum dot labeling and imaging of glial fibrillary acidic protein intermediate filaments and gliosis in the rat neural retina and dissociated astrocytes. *Journal of Nanoscience and Nanotechnology*, 9(8):5047-5054, Jan 2009.

12. M Dahan, S Levi, C Luccardini, P Rostaing, B Riveau, and A Triller. Diffusion dynamics of glycine receptors revealed by single-quantum dot tracking. *Science*, 302(5644):442445, Jan 2003.

13. B Cui, C Wu, L Chen, A Ramirez, EL Bearer, W-P Li, WC Mobley, and S Chu. One at a time, live tracking of ngf axonal transport using quantum dots. *Proceedings of the National Academy of Sciences of the United States of America*, 104(34):1366613671, Jan 2007.

14. A Jayagopal, PK Russ, and FR Haselton. Surface engineering of quantum dots for in vivo vascular imaging. *Bioconjugate Chemistry*, 18(5):14241433, Jan 2007.

15. R Roizenblatt, JD Weiland, S Carcieri, GT Qiu, M Behrend, MS Humayun, and RH Chow. Nanobiolistic delivery of indicators to the living mouse retina. *Journal of Neuroscience Methods*, 153(1):154161, Jan 2006.

16. MEJ van Velthoven, DJ Faber, FD Verbraak, TG van Leeuwen, and MD de Smet. Recent developments in optical coherence tomography for imaging the retina. *Progress in Retinal and Eye Research*, 26(1):57-77, Jan 2007.

17. TM Lee, AL Oldenburg, S Sitafalwalla, DL Marks, W Luo, FJ-J Toublan, KS Suslick, and SA Boppart. Engineered microsphere contrast agents for optical coherence tomography. *Optics Letters*, 28(17):15468, Sep 2003.

18. J Chen, F Saeki, BJ Wiley, H Cang, MJ Cobb, ZY Li, L Au, H Zhang, MB Kimmey, XD Li, and YN Xia. Gold nanocages: Bioconjugation and their potential use as optical imaging contrast agents. *Nano Letters*, 5(3):473477, Jan 2005.

19. H Cang, T Sun, Z-Y Li, J Chen, BJ Wiley, Y Xia, and X Li. Gold nanocages as contrast agents for spectroscopic optical coherence tomography. *Optics Letters*, 30(22):304850, Nov 2005.

20. AL Oldenburg, JR Gunther, and SA Boppart. Imaging magnetically labeled cells with magnetomotive optical coherence tomography. *Optics Letters*, 30(7):7479, Apr 2005.

21. AL Oldenburg, V Crecea, SA Rinne, and SA Boppart. Phase-resolved magnetomotive oct for imaging nanomolar concentrations of magnetic nanoparticles in tissues. *Optics Express*, 16(15):1152511539, Jul 2008.

22. TL Jennings, MP Singh, and GF Strouse. Fluorescent lifetime quenching near d = 1.5 nm gold nanoparticles: probing nset validity. *Journal of the American Chemical Society*, 128(16):54625467, Apr 2006.

23. CS Yun, A Javier, T Jennings, M Fisher, S Hira, S Peterson, B Hopkins, NO Reich, and GF Strouse. Nanometal surface energy transfer in optical rulers, breaking the fret barrier. *Journal of the American Chemical Society*, 127(9):31153119, Mar 2005.

24. J Homola, SS Yee, and G Gauglitz. Surface plasmon resonance sensors: review. *Sensors and Actuators B: Chemical*, 54(1-2):3-15, Jan 1999.

25. A Miyawaki, J Llopis, R Heim, JM McCaffery, JA Adams, M Ikura, and RY Tsien. Fluorescent indicators for ca2+ based on green fluorescent proteins and calmodulin. *Nature*, 388(6645):882887, Aug 1997.

26. T Nagai, A Sawano, ES Park, and A Miyawaki. Circularly permuted green fluorescent proteins engineered to sense ca2+. *Proceedings of the National Academy of Sciences of the United States of America*, 98(6):31973202, Jan 2001.

27. J Nakai, M Ohkura, and K Imoto. A high signal-to-noise ca2+ probe composed of a single green fluorescent protein. *Nature biotechnology*, 19(2):137141, Jan 2001.

28. AE Palmer, C Jin, JC Reed, and RY Tsien. Bcl-2-mediated alterations in endoplasmic reticulum ca2+ analyzed with an improved genetically encoded fluorescent sensor. *Proceedings of the National Academy of Sciences of the United States of America*, 101(50):1740417409, Jan 2004.

29. AE Palmer and RY Tsien. Measuring calcium signaling using genetically targetable fluorescent indicators. *Nature Protocols*, 1(3):1057 1065, Jan 2006.

30. N Heim and O Griesbeck. Genetically encoded indicators of cellular calcium dynamics based on troponin c and green fluorescent protein. *Journal of Biological Chemistry*, 279(14):1428014286, Jan 2004.

31. M Mank, DF Reiff, N Heim, MW Friedrich, A Borst, and O Griesbeck. A fret-based calcium biosensor with fast signal kinetics and high fluorescence change. *Biophysical Journal*, 90(5):17901796, Jan 2006. 2006;90:1790-1796.

32. O Garaschuk, O Griesbeck, and A Konnerth. Troponin c-based biosensors: A new family of genetically encoded indicators for in vivo calcium imaging in the nervous system. *Cell Calcium*, 42(4-5):351361, Jan 2007.

33. MS Siegel and EY Isacoff. A genetically encoded optical probe of membrane voltage. *Neuron*, 19(4):735741, Jan 1997.

34. G Guerrero, MS Siegel, B Roska, E Loots, and EY Isacoff. Tuning flash: Redesign of the dynamics, voltage range, and color of the genetically encoded optical sensor of membrane potential. *Biophysical Journal*, 83(6):3607 3618, Jan 2002.

35. Dimitar Dimitrov, You He, Hiroki Mutoh, Bradley J Baker, Lawrence Cohen, Walther Akemann, and Thomas Knopfel. Engineering and char- acterization of an enhanced fluorescent protein voltage sensor. *PLoS ONE*, 2(5):e440, Jan 2007.

36. BJ Baker, H Mutoh, D Dimitrov, W Akemann, A Perron, Y Iwamoto, L Jin, LB Cohen, EY Isacoff, VA Pieribone, T Hughes, and T Knopfel. Genetically encoded fluorescent sensors of membrane potential. *Brain Cell Biology*, 36(1-4):5367, Jan 2008.

37. A Lundby, H Mutoh, D Dimitrov, W Akemann, and T Knopfel. Engineering of a genetically encodable fluorescent voltage sensor exploiting fast ci-vsp voltage-sensing movements. *PLoS ONE*, 3(6):e2514, Jan 2008.

38. T Kuner and GJ Augustine. A genetically encoded ratiometric indicator for chloride: capturing chloride transients in cultured hippocampal neurons. *Neuron*, 27(3):447459, Jan 2000.

39. O Markova, M Mukhtarov, E Real, Y Jacob, and P Bregestovski. Genetically encoded chloride indicator with improved sensitivity. *Journal of Neuroscience Methods*, 170(1):6776, Jan 2008.

40. WP Hall, JN Anker, Y Lin, J Modica, M Mrksich, and RP van Duyne. A calcium-modulated plasmonic switch. *Journal of the American Chemical Society*, 130(18):58365837, Jan 2008.

41. SY Lin, SW Liu, CM Lin, and CH Chen. Recognition of potassium ion in water by 15-crown-5 functionalized gold nanoparticles. *Analytical Chemistry*, 74(2):330335, Jan 2002.

42. CY Chen, CT Cheng, CW Lai, PW Wu, KC Wu, PT Chou, YH Chou, and HT Chiu. Potassium ion recognition by 15-crown-5 functionalized cdse/zns quantum dots in h2o. *Chemical Communications*, (3):263265, Jan 2006.

43. T Prow, R Grebe, C Merges, J Smith, D McLeod, J Leary, and G Lutty. Nanoparticle tethered antioxidant response element as a biosensor for oxygen induced toxicity in retinal endothelial cells. *Molecular Vision*, 12(67-69):616625, Jan 2006.

44. TW Prow, I Bhutto, R Grebe, K Uno, C Merges, DS Mcleod, and GA Lutty. Nanoparticle-delivered biosensor for reactive oxygen species in diabetes. *Vision Research*, 48(3):478485, Jan 2008.

45. DR Radu, CY Lai, JW Wiench, M Pruski, and VSY Lin. Gatekeeping layer effect: A poly(lactic acid)-coated mesoporous silica nanosphere-based fluorescence probe for detection of amino-containing neurotransmitters. *Journal of the American Chemical Society*, 126(6):16401641, Jan 2004.

46. M Merodio, JM Irache, F Valamanesh, and M Mirshahi. Ocular disposition and tolerance of ganciclovir-loaded albumin nanoparticles after intravitreal injection in rats. *Biomaterials*, 23(7):15871594, Jan 2002.

47. Khosro Adibkia, Yadollah Omidi, Mohammad R Siahi, Ali R Javadzadeh, Mohammad Barzegar-Jalali, Jaleh Barar, Nasrin Maleki, Ghobad Mohammadi, and Ali Nokhodchi. Inhibition of endotoxin-induced uveitis by methylprednisolone acetate nanosuspension in rabbits. *Journal of Ocular Pharmacology and Therapeutics*, 23(5):421432, Jan 2007.

48. Padma V Devarajan and Ganeshchandra S Sonavane. Preparation and in vitro/in vivo evaluation of gliclazide loaded eudragit nanoparticles as a sustained release carriers. *Drug Development and Industrial Pharmacy*, 33(2):101111, Jan 2007.

49. Y de Kozak, K Andrieux, H Villarroya, C Klein, B Thillaye-Goldenberg, MC Naud, E Garcia, and P Couvreur. Intraocular injection of tamoxifen-loaded nanoparticles: a new treatment of experimental autoimmune uveoretinitis. *European Journal of Immunology*, 34(12):37023712, Jan 2004

50. T Sakai, H Kohno, T Ishihara, M Higaki, S Saito, M Matsushima, Y Mizushima, and K Kitahara. Treatment of experimental autoimmune uveoretinitis with poly(lactic acid) nanoparticles encapsulating betamethasone phosphate. *Experimental Eye Research*, 82(4):657663, Jan 2006.

51. J Xu, Y Wang, Y Li, X Yang, P Zhang, H Hou, Y Shi, and C Song. Inhibitory efficacy of intravitreal dexamethasone acetate-loaded plga nanoparticles on choroidal neovascularization in a laser-induced rat model. *Journal of Ocular Pharmacology and Therapeutics*, 23(6):527539, Jan 2007.

52. N Hashida, N Ohguro, N Yamazaki, Y Arakawa, E Oiki, H Mashimo, N Kurokawa, and Y Tano. High-efficacy site-directed drug delivery system using sialyl-lewis x conjugated liposome. *Experimental Eye Research*, 86(1):138149, Jan 2008.

53. T Hammady, J-M Rabanel, RS Dhanikula, G Leclair, and P Hildgen. Functionalized nanospheres loaded with anti-angiogenic drugs: cellular uptake and angiosuppressive efficacy. *European Journal of Pharmaceutics and Biopharmaceutics*, 72(2):418-427, Jan 2009. Special Section: Biological Barriers and Nanomedicine- Advanced Drug Delivery and Predictive non vivo Testing Technologies 2009;72:418-427.

54. J-H Kim, Y-S Kim, K Park, E Kang, S Lee, HY Nam, K Kim, Jae H Park, DY Chi, R-W Park, I-S Kim, K Choi, and IC Kwon. Self-assembled glycol chitosan nanoparticles for the sustained and pro- longed delivery of antiangiogenic small peptide drugs in cancer therapy. *Biomaterials*, 29(12):19201930, Jan 2008.

55. B Bondurant, A Mueller, and DF OBrien. Photoinitiated destabilization of sterically stabilized liposomes. *Biochimica et Biophysica Acta - Biomembranes*, 1511(1):113 122, Jan 2001.

56. A Mueller, B Bondurant, and DF OBrien. Visible-light-stimulated destabilization of peg-liposomes. *Macromolecules*, 33(13):47994804, Jan 2000.

57. R Farjo, J Skaggs, AB Quiambao, MJ Cooper, and MI Naash. Efficient nonviral ocular gene transfer with compacted dna nanoparticles. *PLoS ONE*, 1(1):e38, Jan 2006.

58. X Cai, Z Nash, SM Conley, SJ Fliesler, MJ Cooper, and MI Naash. A partial structural and functional rescue of a retinitis pigmentosa model with compacted dna nanoparticles. *PLoS ONE*, 4(4):e5290, Jan 2009.

59. ALG dos Santos, A Bochot, N Tsapis, F Artzner, RA Bejjani, B Thillaye-Goldenberg, Y de Kozak, E Fattal, and F Behar-Cohen. Oligonucleotide-polyethylenimine complexes targeting retinal cells: Structural analysis and application to anti-tgf beta-2 therapy. *Pharmaceutical Research*, 23(4):770781, Jan 2006.

60. Y Mo, ME Barnett, Ds Takemoto, H Davidson, and UB Kompella. Human serum albumin nanoparticles for efficient delivery of cu, zn superoxide dismutase gene. *Molecular Vision*, 13(80-85):746757, Jan 2007.

61. S Deshpande, S Patil, SVNT Kuchibhatla, and S Seal. Size dependency variation in lattice parameter and valency states in nanocrystalline cerium oxide. *Applied Physics Letters*, 87(13):133113, Jan 2005.

62. GA Silva. Nanomedicine - seeing the benefits of ceria. *Nature Nanotechnology*, 1(2):92-94, Jan 2006.

63. J Chen, S Patil, S Seal, and JF McGinnis. Rare earth nanoparticles prevent retinal degeneration induced by intracellular peroxides. *Nature Nanotechnology*, 1(2):142150, Jan 2006.

64. I Roy, TY Ohulchanskyy, HE Pudavar, EJ Bergey, AR Oseroff, J Morgan, TJ Dougherty, and PN Prasad. Ceramic-based nanoparticles entrapping water-insoluble photosensitizing anticancer drugs: A novel drug-carrier system for photodynamic therapy. *Journal of the American Chemical Society*, 125(26):78607865, Jan 2003.

65. N Nishiyama, HR Stapert, GD Zhang, D Takasu, DL Jiang, T Nagano, T Aida, and K Kataoka. Light-harvesting ionic dendrimer porphyrins as new photosensitizers for photodynamic therapy. *Bioconjugate Chemistry*, 14(1):5866, Jan 2003.

66. R Ideta, F Tasaka, WD Jang, N Nishiyama, GD Zhang, A Harada, Y Yanagi, Y Tamaki, T Aida, and K Kataoka. Nanotechnology-based photodynamic therapy for neovascular disease using a supramolecular nanocarrier loaded with a dendritic photosensitizer. *Nano Letters*, 5(12):24262431, Jan 2005.

67. ME Wieder, DC Hone, MJ Cook, MM Handsley, J Gavrilovic, and DA Russell. Intracellular photodynamic therapy with photosensitizer-nanoparticle conjugates: cancer therapy using a 'trojan horse. *Photochemistry & Photobiological Sciences*, 5(8):727734, Jan 2006.

68. DC Hone, PI Walker, R Evans-Gowing, S FitzGerald, A Beeby, I Chambrier, MJ Cook, and DA Russell. Generation of cytotoxic singlet oxy- gen via phthalocyanine-stabilized gold nanoparticles: A potential delivery vehicle for photodynamic therapy. *Langmuir*, 18(8):29852987, Jan 2002.

69. D Gao, RR Agayan, H Xu, MA Philbert, and R Kopelman. Nanoparticles for two-photon photodynamic therapy in living cells. *Nano Letters*, 6(11):23832386, Jan 2006.

70. R Kopelman, YEL Koo, M Philbert, BA Moffat, GR Reddy, P McConville, DE Hall, TL Chenevert, MS Bhojani, SM Buck, A Rehemtulla, and BD Ross. Multifunctional nanoparticle platforms for in vivo mri enhancement and photodynamic therapy of a rat brain cancer. *Journal of Magnetism and Megnetic Materials*, 293(1):404-410, Jan 2005.

71. F Yan and R Kopelman. The embedding of meta-tetra(hydroxyphenyl)-chlorin into silica nanoparticle platforms for photodynamic therapy and their singlet oxygen production and ph-dependent optical properties. *Photochemistry and Photobiology*, 78(6):587591, Jan 2003.

72. A Ito, E Hibino, C Kobayashi, H Terasaki, H Kagami, M Ueda, T Kobayashi, and H Honda. Construction and delivery of tissue-engineered human retinal pigment epithelial cell sheets, using magnetite nanoparticles and magnetic force. *Tissue Engineering*, 11(3-4):489496, Jan 2005.

73. Manuel Arruebo, Rodrigo Fernandez-Pacheco, M. Ricardo Ibarra, and Jesus Santamaria. Magnetic nanoparticles for drug delivery. *Nano Today*, 2(3):22-32, Jan 2007.

74. RG Ellis-Behnke, YX Liang, SW You, DKC Tay, SG Zhang, KF So, and GE Schneider. Nano neuro knitting: Peptide nanofiber scaffold for brain repair and axon regeneration with functional return of vision. *Proceedings of the National Academy of Sciences of the United States of America*, 103(13):50545059, Jan 2006.

75. J Guo, H Su, Y Zeng, Y-X Liang, WM Wong, RG Ellis-Behnke, K-F So, and W Wu. Reknitting the injured spinal cord by self-assembling peptide nanofiber scaffold. *Nanomedicine: Nanotechnology, Biology and Medicine*, 3(4):311321, Jan 2007.

Chapter 2

Targeting the brain: advances in drug delivery

Abstract

The blood-brain barrier (BBB) represents a significant obstacle for drug delivery to the brain. Many therapeutics with potential for treating neurological conditions prove incompatible with intravenous delivery simply because of this barrier. Rather than modifying drugs to penetrate the BBB directly, it has proven more efficacious to either physically bypass the barrier or to use specialized delivery vehicles that circumvent BBB regulatory mechanisms. Controlled-release intracranial polymer implants and particle injections are the clinical state of the art with regard to localized delivery, although these approaches can impose significant surgical risks. Focused ultrasound provides a non-invasive alternative that may prove more desirable for acute treatment of brain tumors and other conditions requiring local tissue necrosis. For targeting the brain as a whole, cell-penetrating peptides (CPPs) and molecular trojan horses (MTHs) have demonstrated particular ability as delivery molecules and will likely see increased application. CPPs are not brain specific but offer the potential for efficient traversal of the BBB, and tandem systems with targeting molecules may produce extremely effective brain drug delivery tools. Molecular trojan horses utilize receptor-mediated transcytosis to transport cargo and are thus limited by the quantity of relevant receptors; however, they can be very selective for the BBB endothelium and have shown promise in gene therapy.

2.1 Introduction

Access to the central nervous system (CNS) is strictly regulated by three general barriers: the arachnoid epithelium (AE), the choroid plexus epithelium (CPE), and the blood-brain barrier (BBB) comprised of the cerebrovascular endothelium. The AE and CPE separate the blood from the cerebrospinal fluid (CSF), while the BBB, as its name implies, directly separates the blood from the cells of the brain [1]. The selectivity of these barriers, fundamental to their role in CNS protection and physiology, is likewise fundamental to the difficulty in treating CNS diseases with traditional systemic pharmaceutical delivery. The BBB is the primary concern for a conventional approach, as it provides the only means of direct access to nearly every cell in the brain. Yet this barrier presents great restrictions on the size and form of any pharmacologic agent intended to reach the brain at a sufficient concentration. The tight junctions between cells of the BBB provide essentially no access to the brain, permitting limited penetration to only very small polar molecules. For passive diffusion through the cells themselves, the molecules need to be lipophilic and $\lesssim$400 Da in mass. In fact, only 2% of small molecule drugs pass through the BBB [2, 3].

In order to overcome these severe limitations, it is necessary to either bypass the BBB altogether, or to facilitate passage across it via controlled exploitation of the barrier's constituent molecules. We divide these delivery approaches into three general categories: transcranial, transnasal, and transvascular (see Figure 1.1). Transcranial systems typically require a craniotomy or drilling into the skull to expose a desired region of the brain where the drug of choice will be introduced. Transnasal delivery consists of injection into the nasal cavity and subsequent transport across the nasal epithelium directly to the olfactory bulbs of the brain. The broadest in scope, tranvascular approaches couple injection into the systemic cir-

culation with techniques for BBB disruption or circumvention.

2.2 Transcranial Delivery

Perhaps the most straightforward approach to overcoming the BBB is to bypass it entirely. One can inject drug directly, or surgically install an implant at a desired site in the brain and have the local environment receive controlled doses over an extended period of time. The benefits of the transcranial approach include: the avoidance of systemic exposure to high levels of drug just to get sufficient amounts across the BBB; the ability to provide acute or long-term delivery to highly localized regions of the brain; and the ability to use the desired pharmaceutical in its unaltered form, rather than having to expend great efforts specially derivitizing it for brain targeting. There are of course negatives to this methodology as well. The potential complications from neurosurgery are severe, ranging from infection to physical brain trauma. Additionally, localized delivery can easily be a hindrance; delivery to the entire brain via transcranial techniques is exceedingly difficult.

2.2.1 Intracerebroventricular and Intrastriatal Injection

The most common bolus transcranial injections are intracerebroventricular (ICV) injections. ICV administration depends on the diffusion of drug from the cerebrospinal fluid (CSF) through the ependymal layer to the rest of the brain [2]. The technique has been utilized frequently in studying the CNS response to various drugs and other therapeutics. For example, ICV delivery of vascular endothelial growth factor (VEGF) delayed the onset of model amyotrophic lateral sclerosis (ALS) in rats [4]. ICV injection of streptozotocin elucidated a correlation

between oxidative stress and cognitive impairment, a suspect in the advancement of Alzheimer's disease (AD) [5]. Interleukin (IL)-1 has also been injected in this fashion and been found to increase systemic levels of IL-6 [6]. Likewise, kisspeptin was shown to elevate plasma levels of leutenizing hormone (LH) [7]. Centrally-induced systemic effects have to be considered carefully, though, as ICV injection also delivers a large quantity of drug to the circulatory system. In fact, a study on the distribution of leptin after ICV injection noted that, after 20 minutes, levels of circulating leptin equaled or exceeded that of intravenous injection [8]. This points to one of the main issues concerning ICV: efflux of the molecule of interest often occurs more quickly than diffusion to the brain tissue. The CSF is completely cycled every 4 to 5 hours, making ICV injection an efficient, albeit generally undesired, technique for gradual delivery throughout the entire body [2].

Injection into the striatum of humans may not be the most desirable approach to delivery, requiring penetration to the center of the brain. However, it is not an uncommon injection site for viral vector experiments *in vivo*, and has shown some promising results [9-12]. For example, lentiviral transfection of a gene for glial-derived neurotrophic factor (GDNF) was able to prevent neurodegeneration in primate models of Parkinson's disease (PD) [9]. Adeno-associated viral delivery of aspartoacylase to mouse models of Canavan disease (CD) prevented stereotypical degeneration of the thalamus [10], and a variation of this protocol has been considered for human testing [13].

2.2.2 Convection-Enhanced Delivery

Convection-Enhanced Delivery (CED) attempts to overcome the slow diffusion problem of bolus injections. Slow continuous injection of fluid generates bulk flow, which accelerates permeation of the CSF and/or brain interstitium. Indeed,

CED can significantly improve distribution within brain tissue [14, 15]. However, it is still more or less a local delivery method, and the exact extent of distribution is dependent on the site of injection and various characteristics of the delivery vehicle used, such as size, surface motifs, and charge. For example, neutral liposomes under 100 nm in diameter and coated with poly(ethylene glycol) (PEG)-like molecules tend to penetrate tissue more effectively than others [16, 17]. Still, the extended volume of tissue penetration has, for example, enabled targeted delivery to tumors: epidermal growth factor (EGF) has been shown to selectively localize to EGF-receptor positive gliomas [18]. CED has inspired a wealth of research, particularly in the treatment of various brain cancers [17, 19]. But it has also been applied in conjunction with gene therapies, such as adeno-associated viral (AAV) delivery vectors [20, 21]. Such a delivery system has notably been developed as part of a treatment for PD, and recently entered phase I trials. The transfected gene encodes human aromatic L-amino acid decarboxylase (hAADC) which can convert L-dopa treatments into dopamine [22]. CED-based delivery of GDNF for PD treatment has also recently undergone phase I trials [23]. Despite the burgeoning successes with PD, CED in cancer treatment has proven somewhat limited. This is likely due to imperfect permeation of tumors, and has underscored the need for real-time imaging of CED infusions [19, 24]. A likely contributor to incomplete delivery is the poor clearance of fluid in the brain resulting in preferential flow along the white matter tracts [2].

2.2.3 Implants and Controlled Release

Polymer implants within the brain represent another form of transcranial drug delivery. The advent of controlled-release polymers, pioneered by the work of Robert Langer and Henry Brem, provided the foundation for implant-

based brain drug delivery. The main benefit of these systems is their ability to locally deliver controlled amounts of a given molecule over an extended period of time. However, delivery is completely restricted to the local environment surrounding the implant, with drug concentrations falling to ∼10% within half a millimeter [2]. The most effective controlled-release polymers incorporate biodegradability and a propensity for surface erosion rather than bulk erosion. The latter ensures stable temporal release profiles. The prototypical hydrophobic system is a copolymer of poly(bis(*p*-carboxy-phenoxy)propane) anhydride and sebacic acid (PCPP-SA) and was initially developed to release N,N-bis(2-chloroethyl)-N-nitrosourea (BCNU) for treatment of malignant gliomas [25-31]. The analogous implant for water-soluble molecules consists of fatty acid dimers and sebacic acid (FAD-SA) [32]. It has been utilized to deliver another chemotherapeutic agent, 4-hydroperoxycyclophosphamide [33]. Injectable systems have also been developed. Polymer microspheres composed of gelatin and chondroitin sulfate were used to deliver IL-2, through enzymatically controlled degradation (presumably enhanced in overactive tumor regions) [34]. Virus-loaded microparticles composed of biodegradable poly(lactic-*co*-glycolic) acid (PLGA) were able to deliver virus over an extended period of time and avoid the immune reactions associated with high-titer injections [11]. Another system utilized stable nanoliposomes of cholesterol, 1,2-distearoyl-*sn*-glycero-3-phosphocholine (DSPC), and 1,2-distearoyl-sn-glycero-3-phosphoethanolamine-N-[methoxy(poly(ethylene glycol))-2000] (PEG-DSPE). After initial delivery via CED, the liposomes released chemotherapeutic camptothecin-11 (CPT-11) consistently for up to two months [17].

In spite of the promise of these systems, ethylene-vinyl acetate copolymers (EVAc) are perhaps the most pervasive in research for sustained release in the

brain, likely due to their ease of manufacture. Among other things, they have been used to deliver BCNU (like PCPP-SA) [33], dopamine for PD treatment [25], nerve growth factor (NGF) for AD [35], phenytoin for seizure control [36], and ibuprofen and nitric oxide to inhibit post-hemorrhagic cerebral vasospasm [37, 38]. However, EVAc systems lack one critical feature of their more complex counterparts: they are not biodegradable [33]. Depending on the ultimate goal, this can be a benefit or a detriment but must be taken into account, as drug release will be less temporally stable due to decreasing drug concentration in the delivery matrix.

2.3 Transnasal Delivery

Transnasal delivery avoids the risks associated with surgery, but still provides a way to bypass the BBB. The olfactory region of the nasal mucosa is unique in providing direct access to the brain and CSF without the BBB intervening. Drug molecules can diffuse through the nasal epithelium directly to the CSF or to the olfactory lobes of the brain. The CSF route is of course less desirable, leading to the same problems associated with ICV injection. Despite the lack of BBB, it should be noted that BBB-like diffusion barriers still exist in the nasal epithelium. For example, the presence of dense tight junctions between cells inhibits paracellular diffusion, and membrane efflux proteins, like P-glycoprotein (Pgp), actively remove certain molecules that diffuse transcellularly. Co-injection of Pgp inhibitors, though, can mitigate efflux [39-41].

Regardless of these barriers, a number of studies have shown direct transport of various molecules: insulin, angiotensin, arginine-vasopressin, and adrenocorticotropin have been delivered to the human brain after nasal administration, which would fail to cross the BBB in pharmacologically relevant quantities intra-

venously [40]. Dopamine has also been shown to reach the olfactory lobes of mice [41, 42]. It is important to consider though that the bioavailability of these drugs in brain tissue is typically still less than 1% [41]. Additionally, in some cases, reports of higher than expected delivery to the brain could be a result of damage to the nasal epithelium due to excessive fluid volume of injected treatments [2]. For example, plasmid DNA was found to reach the mouse brain quite effectively via intranasal injection of a 20 uL treatment [43]. Administering such a volume is not uncommon, but it represents $\sim 2/3$ the entire volume of the mouse nasal cavity [44]. For effective single-dose treatments, though, temporary damage to the nasal mucosa may be warranted.

More complex delivery systems incorporate absorption enhancers in an attempt to improve delivery through the nasal epithelium. A number of absorption enhancers have been determined, acting through a diverse array of mechanisms: phosphlipids like didecanoyl-L-α-phosphatidylcholine, surfactants like laureth-9, bile salts like sodium glycocholate, cationic polymers like chitosan, lipids like oleic acid, and cyclodextrins [45, 46]. These molecules are often included in emulsions and nanoparticles (NPs) to improve their efficacy as delivery vehicles. Microemulsions of Labrafil M 1944CS, Cremaphor RH, and ethanol were used to transport nimodipine in rats, offering potential therapies for cerebrovascular spasms, strokes, and migraines [47]. Similarly, emulsions of triglyceride, polyoxyethylene-35-ricioleate, polysorbate (tween) 80, and propylene glycol showed promise in the delivery of an anticonvulsant, Clonazepam [48]. Risperidone, an antipsychotic, displayed improved delivery in rats within nanoemulsions of capmul MCM, polysorbate 80, transcutol, and propylene glycol mixed with chitosan [49]. A more highly engineered system took advantage of lectin biorecognition of saccharides for improved adhesion to the nasal mucosa. These wheat germ

agglutinin(WGA)-conjugated PEG-poly(lactic acid) (PEG-PLA) NPs bound the N-acetyl-D-glucosamines and sialic acids present among the glycosylated membrane proteins of the nasal epithelium [50]. Many of these approaches display significant potential for transnasal brain drug delivery in rodents. In most cases, though, it is unclear if they will be effective in humans. One must keep in mind that the olfactory region of rodent models represents about 50% of the nasal epithelium, whereas in humans it is only 3-8% [2]. Moreover, the ability to diffuse pharamcolgically active quantities of drug from the olfactory lobes to brain regions of interest is questionable.

2.4 Transvascular Delivery

The most broadly applicable delivery route for delivery to the entire brain is directly across the BBB. The distance between capillaries in the brain is about 40 μm, giving direct access to nearly every cell of the brain [51]. Naturally, this is also the most opportune route for areas that are difficult to access via surgery. However, the selectivity of the BBB is so great as to render traditional pharmacological screening methods impractical. In many cases, CNS active drugs are too large or form too many hydrogen bonds ($>$ 8 results in restricted access). In the latter case, lipidization of the molecule to encourage transcellular passage often results in a molecule too large to pass efficiently or destroys the therapeutic activity [2]. As a result, effective delivery across the BBB typically involves the joint effort of multiple distinct molecules with a host of different tasks. These compound methods can be divided into four general categories (see Figure 1.2): BBB disruption, cell-penetrating peptide transport, carrier-mediated transport, and receptor-mediated transcytosis.

2.4.1 Blood-Brain Barrier Disruption

BBB disruption is relatively straightforward and takes advantage of transient disturbances in the barrier to allow passage of molecules of interest. The most basic approach utilizes solvents, like ethanol and dimethyl sulfoxide (DMSO), or detergents like sodium dodecylsulfate and polysorbate 80, to increase transcellular permeation [2]. Inflammatory agents, including bradykinin, histamine, and arachidonic acid, open tight junctions, thereby increasing paracellular penetration of the BBB [52]. In general, though, gross disruption is avoided or unintended: it permits the entry of undesired molecules, notably albumin, which is toxic to astrocytes; and it can elicit a number of neuropathologic conditions [2]. Still, surfactants are frequently incorporated in emulsions, liposomes, and NPs as stabilizers and enhancers of transmission across the BBB. The side effects warrant care, and special attention should be made to the concentration of these elements in treatment solutions.

A non-chemical approach to BBB disruption involves the use of focused ultrasound (FUS) [53-55]. FUS enables deep-tissue manipulation with minimal effects on near-field tissue. The benefit of such an approach is the ability to non-invasively affect deep tissue, either increasing its susceptibility to various drugs through cavitation or completely thermally ablating cells. Used appropriately in the brain, it causes rapid increase in permeability of the BBB with minimal damage to surrounding tissue. Unfortunately, bone attenuates and distorts the ultrasound waves, so a cranial window is typically opened in the subject, introducing many of the risks associated with surgery [53]. Advances in computation and modeling of wave propagation offer the potential to adjust for the signal disturbance, though, and the possibility of operation at lower frequencies over larger areas can avert the issue altogether [53-58]. This approach is of particular interest in the treatment

of tumors, as necrosis is the goal, so local disruption of the BBB and tissue damage are acceptable. The barrier disruption is enough to allow passage of a large range of molecules and particles, including antibodies and the chemotherapeutic doxorubicin [53, 56]. Additionally, the complementary application of magnetic resonance imaging (MRI) or computed tomography (CT) enables adaptive focusing and guidance of FUS for individual subjects [53, 57, 58].

2.4.2 Carrier-Mediated Transport

The BBB is a very restrictive barrier, so the molecules required by the brain often have to be transported by specific membrane-localized proteins. The characteristics of these transporters' substrates can be utilized in drug design to promote efficient delivery to the CNS. One potential target is the choline transporter. This transporter can carry a variety of different quaternary ammonium-containing molecules across the BBB; certain alkylated nicotine analogs are good examples [59]. The large neutral amino acid carrier (LAT1) is exploited by chemotherapeutic D,L-2-amino-5-bis[(2-chloroethyl)amino]-1,2,3,4-tetrahydro-2-naphthoic acid and D,L-1-amino-7-bis[(2-chloroethyl)amino]-1,2,3,4-tetrahydro-l-naphthoic acid (collectively DL-NAM) and antihypertensive L-α-methyl-3,4-dihydroxyphenylalanine (α-methyldopa) [59, 60]. Other drugs are suspected to have delivery mediated by BBB transporters, including anxiolytic diphenhydramine, antihypertensive clonidine, and analgesic fentanyl, but the exact protein targets are unconfirmed [61].

The BBB also possesses members of the ATP binding cassette (ABC) transporter family that prevent certain molecules from remaining in the brain. Avoiding these efflux proteins can be equally as important as encouraging influx. In fact, many lipophilic molecules fail to reach the brain in sufficient quantity entirely due to protein-mediated efflux. Confirmed BBB ABC transporters are Pgp, multidrug

resistance-associated proteins (MRPs) 1, 2, and 5, and breast cancer resistance protein 1 (BCRP1). To overcome these, the conventional approach is to co-administer ABC blockers [62, 63]. For example, a number of studies have demonstrated the efficacy of some modern Pgp blockers, PSC833 and GF120918 (also blocks BRCP1). Both blockers have been shown to increase uptake of cancer therapeutics vinblastine, colchicine, and paclitaxel [62, 64, 65]. GF120918 has also proven effective with protease inhibitor amprenavir [66] and antifungal itraconazole [67].

While newer ABC blockers are much less toxic than their predecessors, they are generally better suited for short treatment periods than chronic ones. Furthermore, their application permits access of all molecules that the target proteins efflux. It is more desirable to modify the drug itself to prevent efflux while maintaining general tranporter activity. Unfortunately, engineering drugs to this end can be complicated, particularly with Pgp and BCRP1, which act on a wide variety of lipophilic substrates [62, 68].

2.4.3 Receptor-Mediated Transcytosis and Molecular Trojan Horses

BBB membrane receptors may provide the most robust mechanism for transvascular drug delivery. Conjugating a drug or delivery vehicle to the appropriate ligand or peptide, commonly called a molecular trojan horse (MTH) can enable receptor-mediated transcytosis (RMT) [69]. The main advantage of MTHs is the ability to transport large cargoes (like antibodies and NPs) while retaining preference for the BBB. The approach is not without limitation, though. The efficacy of tranport is restricted by the number of target receptors and their rate of turnover. Furthermore, depending on the choice of MTH, targeted receptors may no longer perform their intended function and downstream pathways may be

activated erroneously. These caveats need to be considered during system development, but have not proven detrimental to the advancement and characterization of RMT in brain drug delivery.

The use of receptor ligand mimics and biologically-derived peptides provides a simple means to produce RMT, and has been demonstrated with multiple BBB receptors. Neuronal nicotinic acetylcholine receptors, for example, have been targeted with a 29 amino acid sequence derived from rabies virus glycoprotein (RVG); the efficacy of this approach was demonstrated in the delivery of small interfering RNA (siRNA) to the mouse brain [70]. A less direct RMT system has proven useful for NPs. Particles coated wth polysorbate 80 are believed to adsorb apolipoproteins (Apo) A-1, B, and E, which causes binding of low-density lipoprotein (LDL) receptors of the BBB [71-74]. Biodegradable poly(butyl cyanoacrylate) NPs coated this way have been used to deliver doxorubicin, antinociceptives dalargin, kytorphin, and loperamide [71], and nerve growth factor (NGF) as a putative treatment for PD [72]. Solid lipid NPs (SLNs) have utilized polysorbate 80 for delivery of paclitaxel [75-77] and may present an advantage over standard NPs; SLNs incorporate the detergent directly into their matrix and can avoid the issue of free detergent that may destabilize the BBB separately from RMT, leading to toxicity [77].

Insulin and transferrin receptors (TfRs), present in high density at the BBB, are useful targets for RMT, and their ligands have been exploited to deliver, among other things, oligonucleotide-loaded PEG and polyethylenimine (PEI) NPs [78]. However, it is preferable to avoid competition with endogenous ligand, and this has led to the development of specialized peptidomimetic monoclonal antibodies (mAbs). The development and implementation of these systems: 8D3 for mouse TfR [79], OX26 for rat TfR [80], MAb83-14 for human insulin receptor

(hIR) (for Old World primates) [81], and humanized/chimeric forms of MAb83-14 (collectively, HIRMAbs) [82, 83], has been primarily through the efforts of William Pardridge and colleagues [84]. These molecules selectively target BBB receptors in regions distinct from active binding sites, allowing them to bypass the BBB unnoticed during natural RMT. This attractive feature has led to widespread use in a variety of systems, with notable success delivering large carrier systems like liposomes and NPs.

A fair amount of positive results have been reported in gene and oligonucleotide delivery through mAb RMT [84, 85], though it should be stated that some dispute exists as to whether transgenes are being delivered across the BBB or simply into the BBB [86]. Liposomes of dimethyldioctadecylammonium bromide (DDAB), palmitoyl-2-oleoyl-*sn*-glycerol-3-phosphocholine (POPC), and PEG-DSPE conjugated to OX26 were used to deliver GDNF plasmid, producing significant recovery in rat models of PD [87]. Similar pegylated immunoliposomes (PILs) have been used to transfect genes for tyrosine hydroxylase as a PD therapy [88-90]. 8D3 PILs have delivered genes for luciferase and β-galactosidase for functional confirmation; and likewise HIRMAb PILs have transfected Rhesus monkeys [91]. In a more interesting application of 8D3, a β-glucuronidase gene was delivered to rescue a mouse model of type VII mucopolysaccharidosis, a lysosomal storage disorder [92].

Other Ab systems have been used for RNA therapies: knockdown of epidermal growth factor receptor (EGFR) expression was achieved in human brain tumors implanted within mice. PILs were coupled to both 8D3 and HIRMAb to achieve localized delivery of short hairpin RNA (shRNA) to the tumors [93]. Gene expression in rat brain tumors was inhibited with OX26 bound directly to siRNA [94]. Peptide nucleic acid (PNA)-OX26 conjugates have also been delivered [95].

Trojan horse technology has been applied to protein and drug delivery, as well. PILs have been utilized to deliver chemotherapeutic daunomycin to rats *in vivo* [96, 97]. They have also been loaded with propidium iodide and 5(6)-carboxyfluorescein to confirm and characterize passage through BBB-like barriers *in vitro* and with radiolabeled daunomycin *in situ* [98]. PEG-poly(ϵ-caprolactone) polymersomes were linked to OX26 and used to transport NC-1900, a vasopressin analog, as a therapeutic strategy for AD [99]. Neuroprotective human basic fibroblast growth factor (bFGF) displayed increased uptake in the brain and decreased uptake in peripheral organs when coupled to OX26, with minimal reduction in bFGF receptor affinity [100, 101]. Brain-derived neurotrophic factor (BDNF) was similarly conjugated to enhance BBB transport and improve neuroprotective effects [102, 103]. An active HIRMAb-GDNF fusion protein was recently developed for PD [104], and the 8D3-GDNF analog was observed to cross the mouse BBB [105].

A more complicated dual antibody fusion has been developed, as well. It possesses an amyloid β (Aβ)-binding region at one end, and the HIRMAb insulin receptor-binding region at the other. The central portion includes the CH2/CH3 domain of human IgG, bound by neonatal Fc receptor (FcRn). The functionality is intended to be three-fold: first to penetrate the BBB, then to bind and disaggregate Aβ fibrils, and finally to transport Aβ fragments back to the bloodstream as it is effluxed by FcRn. Blood-to-brain transport was demonstrated in Rhesus monkeys; brain-to-blood transport was demonstrated in rats (whose FcR recognizes human IgG); and disaggregation was demonstrated in mice [106]. The molecule still requires cohesive characterization within a single primate model, though, to determine if it can effectively perform all its functions in sequence.

2.4.4 Cell-Penetrating Peptide Transport

Certain arginine-rich, cell-penetrating peptides (CPPs) can carry a wide variety of loads across membrane barriers like the BBB independent of transporters and receptor-mediated transcytosis, and often independent of standard endocytic pathways [107-109]; the exact method of traversal, though, appears to depend on the properties of the load being carried [110]. The prototypic CPP is the human immunodeficiency virus type 1 (HIV-1) transactivator of transcription (TAT)-derived peptide sequence YGRKKRRQRRR [111]. The efficacy of the TAT peptide in transport across the BBB was demonstrated in 1999 with cumbersome β-galactosidase, penetrating all areas of the mouse brain within 4 hours of intraperitoneal injection [112].

Since then, the application of TAT in brain drug delivery has increased greatly. Intravenous delivery to mice of TAT fused with the anti-apoptotic B-cell lymphoma (Bcl)-X_L protein promoted neuron survival and prevented brain infarction due to transient focal ischemia [113]. A TAT-GDNF fusion was also developed and determined to effectively cross the BBB, though it failed to allay degeneration in mouse models of PD [114]. TAT has even proven effective in delivering NPs and micelles to the brain. Intraperitoneal injection of 7.5 mg TAT-conjugated cadmium sulfide core/manganese zinc sulfide shell (CdS:MnZnS) quantum dots (QDs) permitted gross visualization of rat-brain fluorescence under a handheld ultraviolet (UV) light [115]. Micelles of TAT-PEG-cholesterol ($\lesssim$200 nm diameter) were delivered to rat hippocampi within 5 minutes of tail vein injection. Release from these micelles of encapsulated antibiotic ciprofloxacin was demonstrated to occur over the course of 6 hours *in vitro* [111, 116]. While CPP systems are efficient, their main issue is lack of specificity to the BBB; any preferential delivery is due to high vascular surface area relative to organ volume and choice of injection site.

Additionally, potential loss of drug activity, if directly linked to a CPP, has to be considered in development of these systems.

Progress and Perspective

The need for therapeutic access to the brain has prompted the development of numerous strategies to bypass the BBB. However, no single approach has demonstrated applicability in all situations. When confronting a given pathophysiological condition, it becomes prudent to carefully consider the advantages and disadvantages of each delivery system (see Table 1.1). Transcranial delivery is an extreme option that necessitates surgical risk, but it is the only well-established method for providing high local pharmaceutical concentrations in an arbitrary region of the brain. Furthermore, it can be enhanced with polymer technologies to provide for temporally-controlled drug release. It is unlikely that this delivery tactic will become obsolete in the near future, and the continued advancement of polymer release systems along with improvements in surgical robotics will only expand its application and success.

Transnasal and transvascular delivery are similar with respect to the barriers that must be overcome and the applied techniques likely to be successful, but certain distinctions should be made: transnasal approaches provide more localized delivery, as passage to the brain occurs through the olfactory lobe and spreads from there. This regional targeting may prove difficult to adjust to other areas of the brain, a potentially serious limitation. On the other hand, transnasal strategies may be slightly more amenable to the harsher subset of transvascular methodologies. Transient disruption or damage to the olfactory nasal epithelium, while undesirable in chronic treatment, is unlikely to lead to widespread damage to

the CNS and will provide limited exposure to toxic serum albumin. Furthermore, it may be feasible to block systemic transnasal delivery, significantly improving biodistribution and mitigating pharmacological side effects in peripheral organs.

For situations where gross exposure of the brain to treatment is desirable, or at least acceptable, transvascular delivery is probably the most appropriate choice. While there are still some limitations in regard to the total amount of drug delivered, rapid improvements in delivery vehicles and increased understanding of fundamental BBB biology will likely overcome these issues. The incorporation of CPPs and MTHs has dramatically improved the efficacy and safety of transvascular delivery, though biodistribution concerns still exist in peripheral organs, particularly the spleen and liver. MTHs confer greater specificity to the brain than CPPs, but are limited by target membrane receptor expression and turnover. For gene delivery, MTHs may be sufficient, since small degrees of transfection can still translate to large amounts of protein product, and cell-specific promoters can target expression; however, where higher doses of drugs are needed, CPPs may be a better option. Furthermore, the development and implementation of some of the more sophisticated peptidomimetic mAb MTHs can be a prohibitive expense. It may prove more economical and efficient to develop tandem CPP/targeting systems that utilize CPPs to penetrate the BBB, while capitalizing on other molecules to target therapeutics. Whether or not this is undertaken, the development of multiplexed systems will be unavoidable if transvascular delivery is to evolve from a gross brain drug delivery strategy to a directed approach. FUS is currently the only transvascular method providing true control over delivery location, and its application is mostly limited to tumor treatment.

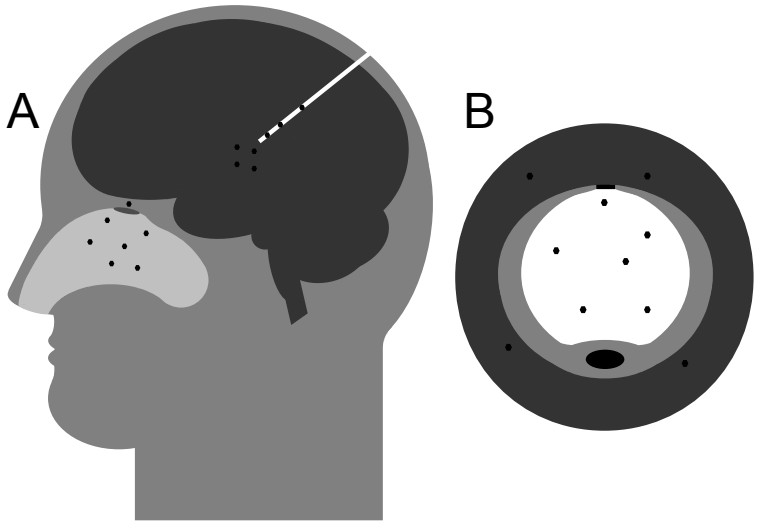

Figure 2.1: General brain drug delivery strategies. (A) Transnasal delivery refers to the passage of drug (small black hexagons) from the nasal cavity (light gray) to the brain (dark gray) through the olfactory epithelium (small gray ellipse within the nasal cavity). Transcranial delivery requires the penetration of the skull into the brain region of interest (white channel) and the direct injection of drug or implantation of a controlled-release device. (B) Transvascular delivery occurs when drug (small black hexagons) passes through the BBB vascular endothelium (light gray cell) from the blood (white) to the brain (dark gray); transport can occur transcellularly, through the cell membranes, or paracellularly, through tight junctions (black rectangle).

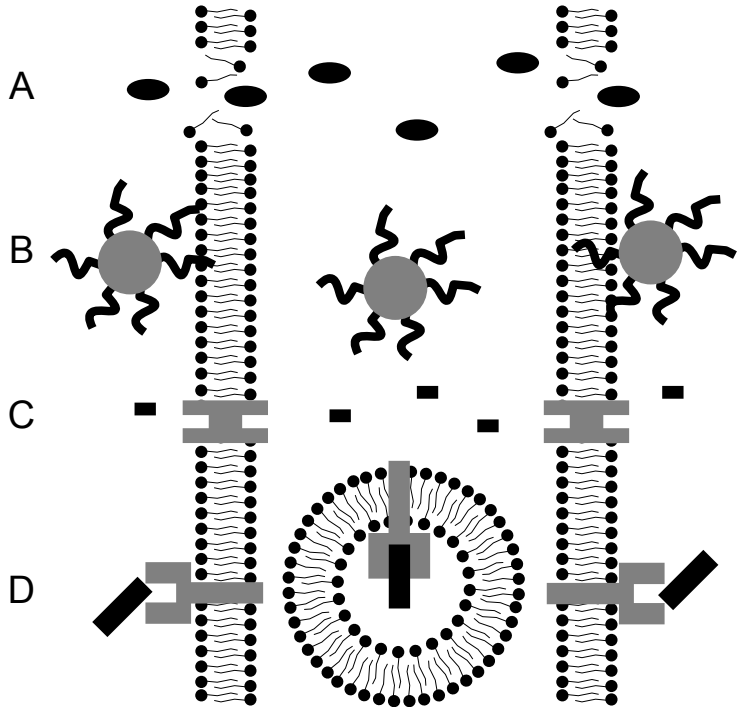

Figure 2.2: Delivery across the blood-brain barrier. Standard approaches to transvascular delivery are illustrated: (A) passage through a disrupted membrane; (B) nanoparticles coated with cell-penetrating peptides; (C) carrier-mediated transport; (D) receptor-mediated transcytosis.

Table 2.1: Comparison of delivery methods across the blood-brain barrier.

Method	Advantages	Disadvantages	Preferred Applications
Intracranial Injection/ Convection Enhanced Delivery	- BBB avoided - Localized	- Delivery near injection only - Surgical risks	- Viral delivery
Intracranial Implant	- BBB avoided - Localized - Prolonged treatment	- Delivery near implant only - Surgical risks	- Brain tumor treatment - Prolonged local delivery
Intranasal Injection	- BBB avoided - No surgery	- Only regions near olfactory lobes accessible - Limited injection volume - Small olfactory region in humans - Presence of BBB-like barrier	- Delivery near olfactory lobes
Focused Ultrasound	- Surgery may be avoided - Localized	- Possible BBB/tissue damage - BBB penetration not selective	- Brain tumor treatment - Transient local delivery
Cell-Penetrating Peptide Coupling	- No surgery - No BBB damage	- Little or no brain specificity - Not localized	- Whole brain therapies
Carrier-mediated transport	- No surgery - No BBB damage - Potential BBB specificity	- Restricted chemical structure of therapeutic - Not localized	- Whole brain therapies
Receptor-Mediated Transcytosis	- No surgery - No BBB damage - Potential BBB specificity	- Restricted by receptor quantity and turnover - Not localized	- Whole brain therapies

2.5 Acknowledgments

This work was supported by grant RO1 NS054736 from the National Institute for Neurological Disorders and Stroke (NINDS) at the National Institutes of Health (NIH).

Chapter 2, in full, is a reprint of the material as it appears in Blumling, James P.; Silva, Gabriel A. "Targeting the brain: advances in drug delivery." *Curr. Pharm. Biotechnol.*, in press. The dissertation author was the primary author of this paper.

2.6 References

1. NJ Abbott, L Rönnbäck, and E Hansson. Astrocyte-endothelial interactions at the blood-brain barrier. *Nature Reviews Neuroscience*, 7(1):41 53, Jan 2006.

2. WM Pardridge. Blood-brain barrier delivery. *Drug Discovery Today*, 12(1-2):54 61, 2007.

3. WM Pardridge. Blood-brain barrier delivery of protein and non-viral gene therapeutics with molecular trojan horses. *Journal of Controlled Release*, 122(3):345348, 2007.

4. E Storkebaum, D Lambrechts, M Dewerchin, MP Moreno-Murciano, S Appel- mans, H Oh, P Van Damme, B Rutten, WY Man, and M De Mol. Treatment of motoneuron degeneration by intracerebroventricular delivery of vegf in a rat model of als. *Nature Neuroscience*, 8(1):8592, 2004.

5. S Shoham, C Bejar, E Kovalev, and M Weinstock. Intracerebroventricular injec- tion of streptozotocin causes neurotoxicity to myelin that contributes to spatial memory deficits in rats. *Experimental Neurology*, 184(2):10431052, 2003.

6. MG De Simoni, M Sironi, A De Luigi, A Manfridi, A Mantovani, and P Ghezzi. Intracerebroventricular injection of interleukin 1 induces high circulating levels of interleukin 6. *Journal of Experimental Medicine*, 171(5):17731777, 1990.

7. MS Irwig, GS Fraley, JT Smith, BV Acohido, SM Popa, MJ Cunningham, ML Gottsch, DK Clifton, and RA Steiner. Kisspeptin activation of gonadotropin releasing hormone neurons and regulation of kiss-1 mrna in the male rat. *Neuroendocrinology*, 80(4):264272, 2005.

8. LM Maness, AJ Kastin, CL Farrell, and WA Banks. Fate of leptin after intracerebroventricular injection into the mouse brain. *Endocrinology*, 139(11):4556 4562, 1998.

9. JH Kordower, ME Emborg, J Bloch, SY Ma, Y Chu, L Leventhal, J McBride, EY Chen, S Palfi, and BZ Roitberg. Neurodegeneration prevented by lentiviral vector delivery of gdnf in primate models of parkinsons disease. *Science*, 290(5492):767773, 2000.

10. R Matalon, S Surendran, PL Rady, MJ Quast, GA Campbell, KM Matalon, SK Tyring, J Wei, CS Peden, and EL Ezell. Adeno-associated virus-mediated aspartoacylase gene transfer to the brain of knockout mouse for canavan disease. *Molecular Therapy*, 7(5):580587, 2003.

11. SJ Beer, JM Hilfinger, and BL Davidson. Extended release of adenovirus from polymer microspheres: potential use in gene therapy for brain tumors. *Advanced Drug Delivery Reviews*, 27(1):5966, 1997.

12. K Mitrophanous, S Yoon, J Rohll, D Patil, F Wilkes, V Kim, S Kingsman, A Kingsman, and N Mazarakis. Stable gene transfer to the nervous system using a non-primate lentiviral vector. *Gene therapy*, 6(11):18081818, 1999.

13. C Janson, S McPhee, L Bilaniuk, J Haselgrove, M Testaiuti, A Freese, DJ Wang, D Shera, P Hurh, and J Rupin. Clinical protocol. gene therapy of canavan disease: Aav-2 vector for neurosurgical delivery of aspartoacylase gene (aspa) to the human brain. *Human Gene Therapy*, 13(11):13911412, 2002.

14. C Mamot, JB Nguyen, M Pourdehnad, P Hadaczek, R Saito, JR Bringas, DC Drummond, K Hong, DB Kirpotin, and T McKnight. Extensive distribution of liposomes in rodent brains and brain tumors following convection-enhanced delivery. *Journal of Neuro-oncology*, 68(1):19, 2004.

15. RH Bobo, DW Laske, A Akbasak, PF Morrison, RL Dedrick, and EH Oldfield. Convection-enhanced delivery of macromolecules in the brain. Proceedings of the National Academy of Sciences, 91(6):20762080, 1994.

16. JA MacKay, DF Deen, and FC Szoka Jr. Distribution in brain of liposomes after convection enhanced delivery; modulation by particle charge, particle diameter, and presence of steric coating. *Brain Research*, 1035(2):139153, 2005.

17. CO Noble, MT Krauze, DC Drummond, Y Yamashita, R Saito, MS Berger, DB Kirpotin, KS Bankiewicz, and JW Park. Novel nanoliposomal cpt-11 infused by convection-enhanced delivery in intracranial tumors: pharmacology and efficacy. *Cancer Research*, 66(5):28012806, 2006.

18. W Yang, RF Barth, DM Adams, MJ Ciesielski, RA Fenstermaker, S Shukla, W Tjarks, and MA Caligiuri. Convection-enhanced delivery of boronated epi- dermal growth factor for molecular targeting of egf receptor-positive gliomas. *Cancer Research*, 62(22):65526558, 2002.

19. MA Vogelbaum. Convection enhanced delivery for the treatment of malignant gliomas: symposium review. *Journal of Neuro-oncology*, 73(1):5769, 2005.

20. P Hadaczek, M Kohutnicka, MT Krauze, J Bringas, P Pivirotto, J Cunningham, and K Bankiewicz. Convection-enhanced delivery of adeno-associated virus type 2 (aav2) into the striatum and transport of aav2 within monkey brain. *Human Gene Therapy*, 17(3):291302, 2006.

21. J Cunningham, P Pivirotto, J Bringas, B Suzuki, S Vijay, L Sanftner, M Kitamura, C Chan, and KS Bankiewicz. Biodistribution of adeno-associated virus type-2 in nonhuman primates after convection-enhanced delivery to brain. *Molecular Therapy*, 16(7):12671275, 2008.

22. JL Eberling, WJ Jagust, CW Christine, P Starr, P Larson, KS Bankiewicz, and MJ Aminoff. Results from a phase i safety trial of haadc gene therapy for parkin- son disease. *Neurology*, 70(21):19801983, 2008.

23. SS Gill, NK Patel, GR Hotton, K OSullivan, R McCarter, M Bunnage, DJ Brooks, CN Svendsen, and P Heywood. Direct brain infusion of glial cell linederived neurotrophic factor in parkinson disease. *Nature Medicine*, 9(5):589595, 2003.

24. MS Fiandaca, JR Forsayeth, PJ Dickinson, and KS Bankiewicz. Image-guided convection-enhanced delivery platform in the treatment of neurological diseases. *Neurotherapeutics*, 5(1):123127, 2008.

25. R Langer. Polymer implants for drug delivery in the brain. *Journal of Controlled Release*, 16(1-2):5359, 1991.

26. H Brem and R Langer. Polymer-based drug delivery to the brain. *Science and Medicine*, 3:5261, 1996.

27. H Brem and P Gabikian. Biodegradable polymer implants to treat brain tumors. *Journal of Controlled Release*, 74(1-3):637, Jul 2001.

28. H Brem, R J Tamargo, A Olivi, M Pinn, J D Weingart, M Wharam, and J I Epstein. Biodegradable polymers for controlled delivery of chemotherapy with and without radiation therapy in the monkey brain. *Journal of Neurosurgery*, 80(2):283290, Feb 1994.

29. C Guerin, A Olivi, JD Weingart, HC Lawson, and H Brem. Recent advances in brain tumor therapy: local intracerebral drug delivery by polymers. *Investigational New Drugs*, 22(1):2737, 2004.

30. EP Sipos, B Tyler, S Piantadosi, PC Burger, and H Brem. Optimizing interstitial delivery of bcnu from controlled release polymers for the treatment of brain tumors. *Cancer Chemotherapy and Pharmacology*, 39(5):383389, 1997.

31. RJ Tamargo, JI Epstein, CS Reinhard, M Chasin, and H Brem. Brain biocompatibility of a biodegradable, controlled-release polymer in rats. *Journal of Biomedical Materials Research*, 23(2):253266, 2004.

32. H Brem, A Domb, D Lenartz, C Dureza, A Olivi, and JI Epstein. Brain biocompatibility of a biodegradable controlled release polymer consisting of anhydride copolymer of fatty acid dimer and sebacic acid. *Journal of Controlled Release*, 19(1-3):325329, 1992.

33. KG Buahin, KD Judy, C Hartke, AJ Domb, M Maniar, OM Colvin, and H Brem. Controlled release of 4-hydroperoxycyclophosphamide from the fatty acid dimer-sebacic acid copolymer. *Polymers for Advanced Technologies*, 3(6):311316, 2003.

34. J Hanes, A Sills, Z Zhao, KW Suh, B Tyler, F DiMeco, DJ Brat, MA Choti, KW Leong, and DM Pardoll. Controlled local delivery of interleukin-2 by biodegradable polymers protects animals from experimental brain tumors and liver tumors. *Pharmaceutical research*, 18(7):899906, 2001.

35. C E Krewson, R Dause, M Mak, and W M Saltzman. Stabilization of nerve growth factor in controlled release polymers and in tissue. *Journal of Biomaterials Science Polymer Edition*, 8(2):103117, Jan 1996.

36. RJ Tamargo, LA Rossell, EH Kossoff, BM Tyler, MG Ewend, and JJ Aryanpur. The intracerebral administration of phenytoin using controlled-release polymers reduces experimental seizures in rats. *Epilepsy Research*, 48(3):145155, 2002.

37. JL Frazier, G Pradilla, PP Wang, and RJ Tamargo. Inhibition of cerebral vasospasm by intracranial delivery of ibuprofen from a controlled-release polymer in a rabbit model of subarachnoid hemorrhage. *Journal of Neurosurgery: Pediatrics*, 101(1):9398, 2004.

38. P Gabikian, RE Clatterbuck, CG Eberhart, BM Tyler, TS Tierney, and RJ Tamargo. Prevention of experimental cerebral vasospasm by intracranial delivery of a nitric oxide donor from a controlled-release polymer: toxicity and efficacy studies in rabbits and rats. *Stroke*, 33(11):26812686, 2002.

39. CL Graff and GM Pollack. Nasal drug administration: potential for targeted central nervous system delivery. *Journal of Pharmaceutical Sciences*, 94(6):1187 1195, 2005.

40. L Illum. Nasal drug delivery: new developments and strategies. *Drug Discovery Today*, 7(23):11841189, 2002.

41. L Illum. Nasal drug deliverypossibilities, problems and solutions. *Journal of Controlled Release*, 87(1-3):187198, 2003.

42. M Dahlin, U Bergman, B Jansson, E Björk, and E Brittebo. Transfer of dopamine in the olfactory pathway following nasal administration in mice. *Pharmaceutical Research*, 17(6):737742, 2000.

43. YK Oh, JP Kim, TS Hwang, JJ Ko, JM Kim, JS Yang, and CK Kim. Nasal absorption and biodistribution of plasmid dna: an alternative route of dna vaccine delivery. *Vaccine*, 19(31):45194525, 2001.

44. EA Gross, JA Swenberg, S Fields, and JA Popp. Comparative morphometry of the nasal cavity in rats and mice. *Journal of Anatomy*, 135(Pt 1):8388, 1982.

45. SS Davis and L Illum. Absorption enhancers for nasal drug delivery. *Clinical Pharmacokinetics*, 42(13):11071128, 2003.

46. MI Ugwoke, RU Agu, N Verbeke, and R Kinget. Nasal mucoadhesive drug delivery: Background, applications, trends and future perspectives. *Advanced Drug Delivery Reviews*, 57(11):16401665, 2005.

47. Q Zhang, X Jiang, W Jiang, W Lu, L Su, and Z Shi. Preparation of nimodipine-loaded microemulsion for intranasal delivery and evaluation on the targeting efficiency to the brain. *International Journal of Pharmaceutics*, 275(1-2):8596, 2004.

48. TK Vyas, AK Babbar, RK Sharma, S Singh, and A Misra. Intranasal mucoadhesive microemulsions of clonazepam: Preliminary studies on brain targeting. *Journal of Pharmaceutical Sciences*, 95(3):570581, 2006.

49. M Kumar, A Misra, AK Babbar, AK Mishra, P Mishra, and K Pathak. Intranasal nanoemulsion based brain targeting drug delivery system of risperidone. *International Journal of Pharmaceutics*, 358(1-2):285291, 2008.

50. X Gao, W Tao, W Lu, Q Zhang, Y Zhang, X Jiang, and S Fu. Lectin-conjugated peg-pla nanoparticles: preparation and brain delivery after intranasal administration. *Biomaterials*, 27(18):34823490, 2006.

51. WM Pardridge. Drug delivery to the brain. *Journal of Cerebral Blood Flow & Metabolism*, 17(7):713731, 1997.

52. NJ Abbott. Inflammatory mediators and modulation of blood-brain barrier permeability. *Cellular and Molecular Neurobiology*, 20(2):131147, Apr 2000.

53. N Vykhodtseva, N McDannold, and K Hynynen. Progress and problems in the application of focused ultrasound for blood-brain barrier disruption. *Ultrasonics*, 48(4):279296, 2008.

54. X Yin and K Hynynen. A numerical study of transcranial focused ultrasound beam propagation at low frequency. *Physics in Medicine and Biology*, Jan 2005.

55. J Sun and K Hynynen. The potential of transskull ultrasound therapy and surgery using the maximum available skull surface area. *The Journal of the Acoustical Society of America*, 105:2519, 1999.

56. M Kinoshita, N McDannold, FA Jolesz, and K Hynynen. Targeted delivery of antibodies through the blood-brain barrier by mri-guided focused ultrasound. *Biochemical and Biophysical Research Communications*, 340(4):1085 1090, 2006.

57. Y Hertzberg, A Volovick, Y Zur, Y Medan, S Vitek, and G Navon. Ultrasound focusing using magnetic resonance acoustic radiation force imaging: application to ultrasound transcranial therapy. *Medical Physics*, 37:2934, 2010.

58. JF Aubry, M Tanter, M Pernot, JL Thomas, and M Fink. Experimental demonstration of noninvasive transskull adaptive focusing based on prior computed tomography scans. *The Journal of the Acoustical Society of America*, 113:8493, 2003.

59. DD Allen and PR Lockman. The blood-brain barrier choline transporter as a brain drug delivery vector. *Life Sciences*, 73(13):16091615, Aug 2003.

60. Y Takada, DT Vistica, NH Greig, D Purdon, SI Rapoport, and QR Smith. Rapid high-affinity transport of a chemotherapeutic amino acid across the blood-brain barrier. *Cancer Research*, 52(8):21912196, 1992.

61. A Tsuji. Small molecular drug transfer across the blood-brain barrier via carrier-mediated transport systems. *NeuroRx*, 2(1):5462, 2005.

62. DJ Begley. Abc transporters and the blood-brain barrier. *Current Pharmaceutical Design*, 10(12):1295312, Jan 2004.

63. S Ohtsuki and T Terasaki. Contribution of carrier-mediated transport systems to the bloodbrain barrier as a supporting and protecting interface for the brain; importance for cns drug discovery and development. *Pharmaceutical Research*, 24(9):17451758, 2007.

64. AJM Sadeque, C Wandel, H He, S Shah, and AJJ Wood. Increased drug delivery to the brain by p-glycoprotein inhibition. *Clinical Pharmacology & Therapeutics*, 68(3):231237, 2000.

65. EM Kemper, AE van Zandbergen, C Cleypool, HA Mos, W Boogerd, JH Beijnen, and O van Tellingen. Increased penetration of paclitaxel into the brain by inhibition of p-glycoprotein. *Clinical Cancer Research*, 9(7):28492855, 2003.

66. JE Edwards, KR Brouwer, and PJ McNamara. Gf120918, a p-glycoprotein modulator, increases the concentration of unbound amprenavir in the central nervous system in rats. *Antimicrobial Agents and Chemotherapy*, 46(7):22842286, 2002.

67. F Imbert, M Jardin, C Fernandez, JC Gantier, F Dromer, G Baron, F Mentre, L van Beijsterveldt, E Singlas, and F Gimenez. Effect of efflux inhibition on brain uptake of itraconazole in mice infected with cryptococcus neoformans. *Drug Metabolism and Disposition*, 31(3):319325, 2003.

68. G Szakács, A Váradi, C Özvegy-Laczka, and B Sarkadi. The role of abc transporters in drug absorption, distribution, metabolism, excretion and toxicity (adme-tox). *Drug Discovery Today*, 13(9-10):379393, 2008.

69. WM Pardridge. Drug and gene targeting to the brain with molecular trojan horses. *Nature Reviews Drug Discovery*, 1(2):131139, 2002.

70. P Kumar, H Wu, JL McBride, KE Jung, MH Kim, BL Davidson, SK Lee, P Shankar, and N Manjunath. Transvascular delivery of small interfering rna to the central nervous system. *Nature*, 448(7149):3943, 2007.

71. J Kreuter. Nanoparticulate systems for brain delivery of drugs. *Advanced Drug Delivery Reviews*, 47(1):6581, 2001.

72. KB Kurakhmaeva, IA Djindjikhashvili, VE Petrov, VU Balabanyan, TA Voronina, SS Trofimov, J Kreuter, S Gelperina, D Begley, and RN Alyautdin. Brain targeting of nerve growth factor using poly(butyl cyanoacrylate) nanoparticles. *Journal of Drug Targeting*, 17(8):56474, Sep 2009.

73. B Dehouck, L Fenart, M P Dehouck, A Pierce, G Torpier, and R Cecchelli. A new function for the ldl receptor: transcytosis of ldl across the blood-brain barrier. *Journal of Cell Biology*, 138(4):877889, Aug 1997.

74. P Calvo, B Gouritin, H Chacun, D Desmaële, J DAngelo, JP Noel, D Georgin, E Fattal, JP Andreux, and P Couvreur. Long-circulating pegylated polycyanoacrylate nanoparticles as new drug carrier for brain delivery. *Pharmaceutical Research*, 18(8):11571166, 2001.

75. JM Koziara, PR Lockman, DD Allen, and RJ Mumper. Paclitaxel nanoparticles for the potential treatment of brain tumors. *Journal of Controlled Release*, 99(2):259269, Sep 2004.

76. JM Koziara, PR Lockman, DD Allen, and RJ Mumper. In situ blood-brain barrier transport of nanoparticles. *Pharmaceutical Research*, 20(11):17721778, Nov 2003.

77. P Blasi, S Giovagnoli, A Schoubben, M Ricci, and C Rossi. Solid lipid nanoparticles for targeted brain drug delivery. *Advanced Drug Delivery Reviews*, 59(6):454477, Jul 2007.

78. SV Vinogradov, EV Batrakova, and AV Kabanov. Nanogels for oligonucleotide delivery to the brain. *Bioconjugate Chemistry*, 15(1):5060, Jan 2004.

79. HJ Lee, B Engelhardt, J Lesley, U Bickel, and WM Pardridge. Targetingrat anti-mouse transferrin receptor monoclonal antibodies through blood-brain barrier in mouse. *Journal of Pharmacology and Experimental Therapeutics*, 292(3):1048 1052, 2000.

80. WM Pardridge, JL Buciak, and PM Friden. Selective transport of an anti-transferrin receptor antibody through the blood-brain barrier in vivo. *Journal of Pharmacology and Experimental Therapeutics*, 259(1):6670, Oct 1991.

81. WM Pardridge, YS Kang, JL Buciak, and J Yang. Human insulin receptor monoclonal antibody undergoes high affinity binding to human brain capillaries in vitro and rapid transcytosis through the bloodbrain barrier in vivo in the primate. *Pharmaceutical research*, 12(6):807816, 1995.

82. MJ Coloma, HJ Lee, A Kurihara, EM Landaw, RJ Boado, SL Morrison, and WM Pardridge. Transport across the primate blood-brain barrier of a genetically engineered chimeric monoclonal antibody to the human insulin receptor. *Pharmaceutical Research*, 17(3):266274, 2000.

83. RJ Boado, Y Zhang, Y Zhang, and WM Pardridge. Humanization of anti-human insulin receptor antibody for drug targeting across the human blood-brain barrier. *Biotechnology and Bioengineering*, 96(2):381391, 2007.

84. WM Pardridge. shrna and sirna delivery to the brain. *Advanced Drug Delivery Reviews*, 59(2-3):141152, 2007.

85. RJ Boado. Blood-brain barrier transport of non-viral gene and rnai therapeutics. *Pharmaceutical Research*, 24(9):17721787, Sep 2007.

86. J Lichota, T Skjrringe, LB Thomsen, and T Moos. Macromolecular drug transport into the brain using targeted therapy. *Journal of Neurochemistry*, 113(1):1 13, 2010.

87. Y Zhang and WM Pardridge. Near complete rescue of experimental parkinsons disease with intravenous, non-viral gdnf gene therapy. *Pharmaceutical Research*, 26(5):10591063, 2009.

88. Y Zhang, F Calon, C Zhu, RJ Boado, and WM Pardridge. Intravenous nonviral gene therapy causes normalization of striatal tyrosine hydroxylase and reversal of motor impairment in experimental parkinsonism. *Human Gene Therapy*, 14(1):112, 2003.

89. Y Zhang, F Schlachetzki, YF Zhang, RJ Boado, and WM Pardridge. Normalization of striatal tyrosine hydroxylase and reversal of motor impairment in experimental parkinsonism with intravenous nonviral gene therapy and a brain-specific promoter. *Human Gene Therapy*, 15(4):339350, 2004.

90. CF Xia, C Chu, J Li, Y Wang, Y Zhang, RJ Boado, and WM Pardridge. Comparison of cdna and genomic forms of tyrosine hydroxylase gene therapy of the brain with trojan horse liposomes. *The Journal of Gene Medicine*, 9(7):605612, 2007.

91. Y Zhang, F Schlachetzki, and WM Pardridge. Global non-viral gene transfer to the primate brain following intravenous administration. *Molecular Therapy*, 7(1):1118, 2003.

92. Y Zhang, Y Wang, RJ Boado, and WM Pardridge. Lysosomal enzyme replacement of the brain with intravenous non-viral gene transfer. *Pharmaceutical Research*, 25(2):400406, 2008.

93. Y Zhang, Y Zhang, J Bryant, A Charles, RJ Boado, and WM Pardridge. Intravenous rna interference gene therapy targeting the human epidermal growth factor receptor prolongs survival in intracranial brain cancer. *Clinical Cancer Research*, 10(11):3667, 2004.

94. CF Xia, Y Zhang, Y Zhang, RJ Boado, and WM Pardridge. Intravenous sirna of brain cancer with receptor targeting and avidinbiotin technology. *Pharmaceutical Research*, 24(12):23092316, 2007.

95. T Suzuki, D Wu, F Schlachetzki, JY Li, RJ Boado, and WM Pardridge. Imaging endogenous gene expression in brain cancer in vivo with 111in-peptide nucleic acid antisense radiopharmaceuticals and brain drug-targeting technology. *Journal of Nuclear Medicine*, 45(10):17661775, 2004.

96. J Huwyler, D Wu, and WM Pardridge. Brain drug delivery of small molecules using immunoliposomes. *Proceedings of the National Academy of Sciences of the United States of America*, 93(24):1416414169, 1996.

97. J Huwyler, J Yang, and WM Pardridge. Receptor mediated delivery of daunomycin using immunoliposomes: pharmacokinetics and tissue distribution in the rat. *Journal of Pharmacology and Experimental Therapeutics*, 282(3):1541 1546, 1997.

98. A Cerletti, J Drewe, G Fricker, AN Eberle, and J Huwyler. Endocytosis and transcytosis of an immunoliposome-based brain drug delivery system. *Journal of Drug Targeting*, 8(6):435446, 2000.

99. Z Pang, W Lu, H Gao, K Hu, J Chen, C Zhang, X Gao, X Jiang, and C Zhu. Preparation and brain delivery property of biodegradable polymersomes conjugated with ox26. *Journal of Controlled Release*, 128(2):120127, 2008.

100. D Wu, BW Song, HV Vinters, and WM Pardridge. Pharmacokinetics and brain uptake of biotinylated basic fibroblast growth factor conjugated to a blood-brain barrier drug delivery system. *Journal of Drug Targeting*, 10(3):239245, 2002.

101. BW Song, HV Vinters, D Wu, and WM Pardridge. Enhanced neuroprotective effects of basic fibroblast growth factor in regional brain ischemia after conjugation to a blood-brain barrier delivery vector. *Journal of Pharmacology and Experimental Therapeutics*, 301(2):605610, 2002.

102. Y Zhang and W M Pardridge. Conjugation of brain-derived neurotrophic factor to a blood-brain barrier drug targeting system enables neuroprotection in regional brain ischemia following intravenous injection of the neurotrophin. *Brain Research*, 889(1-2):4956, Jan 2001.

103. Y Zhang, WM Pardridge, and R Keep. Neuroprotection in transient focal brain ischemia after delayed intravenous administration of brain-derived neurotrophic factor conjugated to a blood-brain barrier drug targeting system editorial comment. *Stroke*, 32(6):13781384, Jun 2001.

104. RJ Boado, Y Zhang, Y Zhang, Y Wang, and WM Pardridge. Gdnf fusion protein for targeted-drug delivery across the human blood-brain barrier. *Biotechnology and Bioengineering*, 100(2):38796, Jun 2008.

105. QH Zhou, RJ Boado, JZ Lu, EKW Hui, and WM Pardridge. Monoclonal antibody-glial-derived neurotrophic factor fusion protein penetrates the blood-brain barrier in the mouse. *Drug Metabolism and Disposition*, 38(4):566572, 2010.

106. RJ Boado, Y Zhang, Y Zhang, C-F Xia, and WM Pardridge. Fusion antibody for alzheimers disease with bidirectional transport across the blood-brain barrier and abeta fibril disaggregation. *Bioconjugate Chemistry*, 18(2):44755, Jan 2007.

107. G Ter-Avetisyan, G Tünnemann, D Nowak, M Nitschke, A Herrmann, M Drab, and MC Cardoso. Cell entry of arginine-rich peptides is independent of endocytosis. *Journal of Biological Chemistry*, 284(6):33703378, 2009.

108. JP Richard, K Melikov, E Vives, C Ramos, B Verbeure, MJ Gait, LV Chernomordik, and B Lebleu. Cell-penetrating peptides. *Journal of Biological Chemistry*, 278(1):585590, 2003.

109. H Brooks, B Lebleu, and E Vivès. Tat peptide-mediated cellular delivery: back to basics. *Advanced Drug Delivery Reviews*, Jan 2005.

110. KM Stewart, KL Horton, and SO Kelley. Cell-penetrating peptides as delivery vehicles for biology and medicine. *Organic & biomolecular chemistry*, 6(13):22422255, 2008.

111. L Liu, SS Venkatraman, Y-Y Yang, K Guo, J Lu, B He, S Moochhala, and L Kan. Polymeric micelles anchored with tat for delivery of antibiotics across the blood-brain barrier. *Biopolymers*, 90(5):617 623, Jan 2008.

112. SR Schwarze, A Ho, A Vocero-Akbani, and SF Dowdy. In vivo protein transduction: delivery of a biologically active protein into the mouse. *Science*, 285(5433):15691572, 1999.

113. E Kilic, GPH Dietz, DM Hermann, and M Bähr. Intravenous tat-bcl-xl is protective after middle cerebral artery occlusion in mice. *Annals of Neurology*, 52(5):617622, 2002.

114. GPH Dietz, PC Valbuena, B Dietz, K Meuer, P Müller, JH Weishaupt, and M Bähr. Application of a blood-brain-barrier-penetrating form of gdnf in a mouse model for parkinsons disease. *Brain research*, 1082(1):6166, 2006.

115. S Santra, H Yang, JT Stanley, PH Holloway, BM Moudgil, G Walter, and RA Mericle. Rapid and effective labeling of brain tissue using tat-conjugated cds:mn/zns quantum dots. *Chemical Communications*, 2005(25):31443146, 2005.

116. L Liu, K Guo, J Lu, SS Venkatraman, D Luo, KC Ng, EA Ling, S Moochhala, and YY Yang. Biologically active core/shell nanoparticles self-assembled from cholesterol-terminated peg-tat for drug delivery across the blood-brain barrier. *Biomaterials*, 29(10):15091517, 2008.

Chapter 3

Calcium and EDTA induced folding and unfolding of calmodulin on functionalized quantum dot surfaces

Abstract

Calcium is a ubiquitous second messenger signal that is critical to many cellular processes. As such considerable efforts have been made to develop sensitive high resolution calcium sensors. However, organic dye calcium sensors have inherent limitations in signal to noise ratio and spatial resolution. We have developed a novel quantum dot (qdot) based calcium sensor with superior optical properties for biological detection of functional calcium signaling. Here, we discuss the in vitro calcium binding properties of our sensor. The sensor was designed as a fluorescence resonance energy transfer (FRET) complex, composed of a dihydrolipoic acid capped quantum (DHLA-qdot) which acts as a fluorescence donor, an organic dye (Alexa Fluor 647) which acts as a fluorescence acceptor, and calmodulin (CaM) which serves as the active calcium sensing element. We confirmed that a significant FRET signal was observed between the donor (610 nm) and acceptor (670 nm) emission wavelengths upon binding with calcium ions with a maximal fractional change in FRET ratio (ΔR/R) of up to 6.6. Unlike this DHLA-qdot system, almost no FRET was observed when qdots were coated with the relatively large surface ligands polyethylene glycol and polyethyleneimine, suggesting negative effects of the bulky ligands on CaM folding. Calcium-induced FRET in our system was reversed by EDTA treatment, suggesting the unfolding of CaM on the nanoparticle surface in the absence of calcium, enabling a regeneration of the sensor system.

3.1 Introduction

Intracellular calcium (Ca2+) signaling is ubiquitous and critical to cellular functions and survival. As such, studies on the regulation of Ca2+ dynamics receive significant focus in the life sciences. In order to image and measure these dynamics within cells, numerous calcium indicator dyes have been developed with varying spatial and temporal resolutions. Examples include synthetic dyes with acetoxymethyl (AM) esters [1] and protein based genetically encoded calcium indicators (GECIs) [2, 3].

The synthetic dyes are easy to use in living cells and have large dynamic ranges, high sensitivity and fast kinetic responses. However, photobleaching, compartmentalization, incomplete AM ester hydrolysis and potential toxicity of hydrolysis products, leakage into the extracellular medium, a short assay window and the inability to target specific intracellular compartments and organelles represent significant limitations of these indicators [4, 5]

The GECIs, including the Cameleon [6] family of sensors, have a number of advantages over the chemical dyes, in particular due to their capacity to target intracellular organelles. The GECIs contain one or two genetically encoded fluorescence proteins for fluorescence detection and a calcium sensing protein component, such as calmodulin (CaM) or troponin, which undergoes conformational transitions upon binding with free calcium ions. The well known Cameleon system consists of a tandem connection of a fluorescence donor protein, CaM, a CaM-binding peptide fragment (such as the M13 peptide derived from skeletal myosin light chain kinase), and a fluorescence acceptor protein. Upon binding with calcium ions, the donor-acceptor distance decreases due to a folding of CaM around the peptide fragment [6-9]. This, in turn, increases fluorescence resonance energy transfer (FRET) [6, 7]. The calmodulin based Cameleon was shown to detect free

calcium concentrations in the 10-8 to 10-2M range [6]. A detailed review on GECIs can be found in recent publications [5, 10].

CaM (148 amino acids) exists as a monomer in solution and contains two structurally homologous N- and C-terminal domains joined by a flexible linker. Each domain binds two calcium ions using two helix-turn-helix motifs (EF-hands) [9]. The calcium ion binding affinity of CaM (dissociation constant, Kd of 5x10-7M to 5x10-6M) falls into the biologically relevant range of intracellular free Ca2+ of 10-7M to 10-6M) [8]. Upon binding with calcium ions, CaMs calcium-free apo structure is converted into an extended holo structure with hydrophobic clefts in both domains open for binding to target sequences [8, 9].

Despite the many advantages of GECIs, they suffer from low expression levels in mammalian transgenic animals and experience rather small changes in fluorescence signals, resulting in a poor signal to noise ratio and low sensitivity. Since these sensors are gene-based, alteration of target sites requires obtaining different clones or DNA manipulation by end users. Delivery of GECI DNA to cells requires direct or virus assisted transfection followed by a waiting period of one to three days before fluorescence signals can be detected and experimental success can be determined. To address these limitations, we have constructed a calcium senor composed of a quantum dot fluorescence donor, a mutated Xenopus laevis CaM*-M13* pair that acts as an efficient calcium sensing motif that does not interfere with native CaM calcium binding (provided as a generous gift from Dr. Roger Tsien, UC San Diego) [11], and an organic dye that acts as a fluorescence acceptor. We further mutated the CaM* by introducing a cysteine at the 3rd position of the N-terminal to which we attached the organic dye. Our quantum dot based sensor responds to calcium ions and EDTA with very strong and robust FRET changes that produce large signal to noise ratios with fast temporal kinetics.

In this paper we describe in detail the physical characterization of CaM* folding and unfolding on quantum dot surfaces.

3.2 Materials and Methods

Cloning and purification of CaM protein. Calmodulin protein with a C-terminal hexa-histidine tag was constructed by cloning the CaM*-M13* part of mt-Cameleon in pcDNA3 into pET-28b vector (EMD, Gibbstown, NJ, USA). Two primers (forward : 5-agcataccatggcg*tgt*caactgacagaagagcagatt-3; reverse : 5-ggttcactcgagggagctggagatcttcttcag-3) were used to introduce NcoI and XhoI sites (underlined) at the N- and C-termini, respectively. This process also introduced a single cysteine at the 3rd position (underlined and italicized in the forward primer) and alanine at the 2nd position (H2A/D3C). The histidine 2 to alanine 2 mutation introduced by the NcoI site actually corrected the mutation made during the cloning of the mt-Cameleon into the pcDNA3 vector. The PCR product was digested with restriction enzymes and ligated with pET-28b vector restricted with the same enzymes and treated with Antarctic Phosphatase (NEB, Ipswich, MA, USA) to prevent self-ligation. Positive clones were screened by single colony PCR. For the single colony PCR, a small portion of colonies were directly mixed with 25 μl PCR mixture without a boiling step in water followed by amplification reactions. Using this method, wild-type CaM*-M13* and cysteine mutant CaM*-M13* D3C colonies were identified. The plasmids containing the inserts were purified from DH5 cells and transformed into BL21 Star (DE3) cells for protein expression. For the protein purification, BL21 Star (DE3) cells were grown at 37^{o}C to $OD_{600nm} \sim$ 0.6 and IPTG was added to give a final concentration of 0.6 mM. After 4 hours of further incubation the cells were collected and purified by PrepEase his-tagged

protein purification mini kits (USB, Cleveland, Ohio, USA) by following the protocol provided by the company, except for the lysozyme treatment step which was replaced by sonication. The amount of protein was calculated using an extinction coefficient of ϵ_{280nm} = 9,970 $M^{-1}cm^{-1}$ calculated from its amino acid composition and molecular mass of 20,652 Da for the CaM* aspartic acid 3 to cysteine 3 mutant protein (CaM*-M13* D3C). Larger scale purifications were made using PrepEase midi kit using a 300 ml culture and saved -80^{o}C in 20 mM Tris-HCl, pH 8.0 buffer.

Fluorescence labeling and spectra measurements. Fluorescence and absorption spectra were measured using a SpectraMax M5 microplate reader (Molecular Devices, Sunnyvale, CA, USA) at 25^{o}C. Absorption spectra were measured at 2 nm resolution using a 1 cm path length quartz cuvette. For fluorescence spectra, quartz cuvettes or glass tubes were used depending on the measurements. For quantum dots and sensor complexes, the excitation wavelength was fixed at 400 nm with a photomultiplier voltage set to medium and the emission spectra measured at 2 or 4 nm resolutions at 25^{o}C.

Fluorescence labeling of CaM. Before the labeling reaction, CaM*-M13* D3C protein was treated with 10 mM TCEP (tris(2-carboxyethyl)phosphine) in 1x PBS buffer, pH 7.4 to reduce the single cysteine, followed by removal of the reducing reagent using a10 kDa Millipore filter (Billerica, MA, USA) in order to improve the labeling efficiency [12]. For a typical labeling reaction, CaM*-M13* D3C was mixed with 3-fold molar excess of Alexa Fluor (AF647) maleimide dye (Invitrogen, Carlsbad, Ca, USA) at room temperature for 2 hours in PBS, pH 7.4. After the incubation, unreacted dye was removed by gel filtration using a G-25 column followed by buffer exchange with the 10 kDa filter, first with 20 mM Tris-HCl, pH 8.0, containing 10 mM EDTA, followed by the same buffer without

EDTA.

Preparation of DHLA and PEI capped CsSe/ZnS quantum dots. Octadecyl amine (ODA) capped hydrophobic CdSe/ZnS quantum dots (ODA-qdot 610, emission wavelength ~ 610 nm) were purchased from Ocean Nanotech (Springdale, AR, USA). For the DHLA quantum dot (DHLA-qdot), a quantum dot to DHLA molar ratio of 1:40,000 was used for ligand exchange reactions. The molecular weight (MW) of CdSe cores (qdot 610 without ZnS shell) was estimated to be 283,058 with a diameter of 5.09 nm [13] and concentrations of qdots were calculated using an extinction coefficient of $436{,}996 M^{-1}cm^{-1}$ at the first excitation band.14 For a typical phase transfer reaction, one milligram of ODA-qdot 610 in CHCl3 was near dried at 70^oC followed by the addition of 25mg DHLA (Sigma, T8260) dissolved in 0.6 ml of pure ethyl alcohol in a screw-capped eppendorf tube. The ligand exchange reaction was carried out at 70^oC with occasional mixing during the first two hours and continued overnight with light protection. After the overnight incubation, the reaction mixture was centrifuged at 13,000 rpm using a table top centrifuge for two minutes to remove any unreacted quantum dot particles. The supernatant, which contained qdot-DHLA, unbound DHLA and dissociated ODA, was collected and small grains of potassium tert-butoxide were directly added to the ethanol phase to deprotonate the DHLA for precipitation. Five minutes after the deprotonation, the sample was centrifuged at 13,000 rpm for two minutes and the resulting precipitate washed with 100% ethanol three times to remove free DHLA. After air drying, the DHLA-qdot pellet was resuspended in 20 mM Tris-HCl, pH 8.0. Quantum dots prepared by this method showed both physical and optical stability for more than six months. We found that DHLA (a dithiol) produced a much more stable cap than mercaptododecanoic acid (MDA), which has

only one mercapto group (unpublished results). Polyethylene glycol (PEG) capped quantum dots (Qdot 605 ITK amino (PEG)) with amide functional groups were purchased from Life Technologies (Carlsbad, USA) and polyethyleneimine (PEI) capped quantum dots (PEI-qdot) were prepared by a ligand exchange reaction as described by others [14].

3.3 Results and Discussion

Cloning and screening of CaM clones for bacterial expression. To produce CaM*-M13* and CaM*-M13* D3C proteins in bacteria, we sub-cloned the CaM*-M13* part of mt-Cameleon/pcDNA3 (Palmer et al., 2006) into NcoI and XhoI sites of pET-28b protein over-expression vector (Figure 3.1). The correct colonies containing wild-type and mutant CaM*-M13* D3C inserts were identified by a single colony PCR technique. The results of the single colony PCR screen and the induction patterns of the calmodulin protein from the selected clones are shown in Figure 3.2. Though the pET-28b vector is a low copy numbered plasmid, positive clones containing the wild-type CaM*-M13* and CaM*-M13* D3C mutant sequences were easily identified by PCR analysis (Figure 3.2, lanes 1, 5 and 7).

Purification and fluorescence labeling of calmodulin. The calmodulin protein was easily purified by a single affinity purification step using NTA-Ni2+ columns with the purity in excess of 98% (Figure 3.3A). Typically, about 7 $\sim$ 8 mg of CaM*-M13* D3C was obtained from a 300 ml culture. After the purification, CaM*-M13* D3C was labeled with AF647 maleimide dyes at a cysteine residue introduced at the 3rd position of the N-terminal end of the protein. The fluorescence labeling efficiency of the preparation was estimated to be about 80%

by comparing the absorption peaks at 280 nm and 647 nm for free AF647 dye and AF647 labeled protein (Figure 3.3B). CaM*-M13*-AF647 protein labeled at room temperature showed no indication of degradation (Figure 3.3B inset). The fluorescence intensity of the protein bands in the gel was rather weak compared to a fluorescence protein band in standard (st) due to the excitation wavelength (340 nm) of the UV box used for the gel image.

Self-assembly of fluorescence labeled CaM*-M13*-AF647 on quantum dot surfaces. Using the hexa-histidine tag at the C-terminal end of the CaM*-M13*-AF647, the protein was easily assembled onto the surface of quantum dots. The histidine tag mediated binding of proteins to DHLA or PEG capped qdots has been previously reported [15-17], and has a relatively tight Kd of ∼1 nM [18]. Histidine tag mediated binding of the protein minimizes the uncertainties of donor to acceptor distances and dye orientations on quantum dots, which are problematic in chemically cross-linked proteins [19]. Graph 3.1 shows that the FRET efficiency increases with the number of CaM*-M13*-AF647 positioned near the qdot surface due to enhanced non-radiative energy transfer of excitation energy from the qdot to the acceptor AF647 dye. The experimental FRET efficiency can be determined by following relationship [20]:

$$\mathrm{E} = 1 - \mathrm{F}_{DA}/\mathrm{F}_{D} = \mathrm{nR}_{o}^{6}/(\mathrm{nR}_{o}^{6} + \mathrm{r}^{6})$$

where FDA and FD are the fluorescence intensities of quantum dots in the presence and absence of the acceptor AF647 labeled calmodulin, respectively, and n is the number of CaM proteins bound to a quantum dot. The Ro is the Frster radius, which designates a separation distance corresponding to 50% FRET efficiency. Binding of CaM*-M13*-AF647 with DHLA-qdot 610 at different molar

ratios (0.99, 2.97, 5.91, 7.90 and 10.9) resulted in a gradual increase in FRET efficiency as judged from the qdot emission peaks (Graph 3.1): 12% (1:0.99), 33% (1:2.97), 45% (1:5.91), 52% (1:7.90) and 61% (1:10.9). Since we used an excitation wavelength (400 nm) where there is almost no absorption from the AF647 dye, the decrease of the fluorescence intensities at quantum dot emission peaks and the increased emission of AF647 fluorescence at 670 nm are due to the binding induced FRET. We also estimated the maximum number of CaM*-M13*-AF647 bound to a single quantum dot to be $10 \sim 12$ molecules per quantum dot particle, with an optimal number of calmodulin proteins for calcium sensing to be 2 to 5 molecules per quantum dot. The exact stoichiometry of binding and the stoichiometric dependency of calcium sensing parameters are currently under investigation (manuscript in preparation).

Calcium ion binding-induced folding and EDTA-induced unfolding of calmodulin on quantum dot surfaces. We then tested the calcium sensitivity of the quantum dot-calmodulin complex we constructed. In Graph 3.2A, the fluorescence spectra of the qdot sensor at 0, 0.5 and 1 mM calcium ions are shown. Upon binding with 0.5 mM calcium ions, more than 66% of the quantum dot emission was quenched at the donor fluorescence peaks with about 260% increase in the acceptor emission peak (670 nm). Fractional changes in FRET at 0.5 mM calcium ions were estimated by using a following relationship [3, 21]:

$$\text{Fractional changes in FRET} = \Delta R/R = (R_{Ca^{2+}-saturated}\text{-}R_{Ca^{2+}-free})/R_{Ca^{2+}-free}$$

where R is the acceptor (670 nm) to donor (610 nm) fluorescence intensity ratio. Based on this relationship, the quantum dot sensor gave a $\Delta R/R$ value of about 6.6, which is much greater than the values of $0.5 \sim 0.8$ for the original Cameleon

systems (estimated from figures in [6]) and about 1.7 for troponin C-based calcium sensor (estimated from a supplementary figure in [3]) in vitro. Further addition of calcium to 1 mM caused no change in the AF647 emission peak (670 nm) but resulted in a slight reduction of the quantum dot emission peak (610 nm), probably due to the quenching effects of extra calcium ions on the quantum dot. In the present work we are ignoring any quenching produced by metal or EDTA induced quenching effects on the quantum dots. However, the effects of various metals and ligands on the emission properties of water solubilized CsSe/ZnS quantum dots may not be negligible under certain conditions and may affect the interpretation of experimental data. As such, these effects require further investigation. Since reversible folding and unfolding of the calcium-sensing component (CaM*-M13*) is critical for the system to be used as a calcium ion sensor in vitro and in vivo, we have investigated whether the folded calmodulin can revert to its calcium deficient apo structure following EDTA treatment (Graph 3.2B).

The addition of increasing amounts of EDTA up to 1 mM resulted in the folded qdot 610-CaM*-M13*-AF647 complex presenting decreases at both the 610 nm and 670 nm fluorescence peaks, probably due to EDTA induced quenching of the quantum dots. In the presence of 2 mM EDTA, there were noticeable changes in the FRET signals, with a decrease in fluorescence intensity at 670 nm and an increase at 610 nm, implying the reversal of calcium binding-induced calmodulin folding. The reversal of the FRET response strongly suggests that the calmodulin undergoes an unfolding transition upon calcium deprivation resulting in the restoration of its open conformation. The reversibility of calmodulin folding and unfolding on the quantum dot surfaces allows for a wider range of possible applications for this sensor in cell biology.

Effects of surface ligands on Ca2+binding. We also investigated the effects of different surface ligands (PEG and PEI) on the binding of CaM*-M13*-AF647 to quantum dots and on calcium sensing. In Graph 3.3 the fluorescence spectra for PEG and PEI capped quantum dots upon binding to CaM*-M13*-AF647 and, subsequently, to calcium ions are shown. Binding of the protein caused a decrease in fluorescence intensity at 610 nm with a concomitant increase at 670 nm due to FRET from the quantum dot to the AF647 dye labeled on the CaM*-M13* protein. The data indicate that the histidine tagged calmodulin protein can bind to both neutral (PEG, Graph 3.3) and positively charged (PEI, Graph 3.3 Inset) ligand capped quantum dots, similar to the results of negatively charged DHLA capped quantum dots (Graph 3.1). Binding of histidine tagged proteins [15, 16] and peptides [17] to PEG or DHLA capped quantum dots have also been reported by others. After we confirmed the binding of the histidine tagged calmodulin protein to all three quantum dots, we tested the calcium sensing capacity of the PEG and PEI capped quantum dots. In contrast to DHLA-qdots, both PEG (Graph 3.3) and PEI (Graph 3.3 Inset) quantum dots did not show any significant changes in the presence of calcium ions. The minimal changes in the FRET signals suggest that the calmodulins on the PEG and PEI capped quantum dots are unable to fold upon binding with calcium ions. The longer ligands (PEG and PEI) probably cause an unacceptable degree of steric hindrance to optimal CaM*-M13* folding necessary to achieve the strong FRET signals we observed with DHLA-capped quantum dots.

3.4 Conclusions

We have constructed a novel FRET-based calcium sensor composed of a quantum dot acting as a fluorescence donor, a mutated calmodulin-M13 pair (CaM*-M13*) acting as a calcium sensing module, and a fluorescent dye conjugated to the N-terminal end (3rd position) of the protein acting as a fluorescence acceptor. The use of qdots as FRET donors are numerous, due to their robust optical properties, and include ligand binding studies [15], aptamer-target protein binding [22], peptide-RNA interactions [23], and measurements of enzyme activity [24, 25]. However, to the best of our knowledge, this is the first quantum dot-based calcium sensor. The FRET sensor we constructed produced a maximal fractional change in FRET (ΔR/R) of about 6.6 upon calcium binding, one of the biggest ratio changes among all known FRET-based quantum dot sensors reported in the literature for any system. Despite the many advantages of genetically encoded calcium indicators (GECIs), they still suffer from small changes in fluorescence signal. Considering the ΔR/R values of the original Cameleon and troponin-C based GECIs are in the range of $0.5 \sim 1.7$ [3, 6], the strong FRET response of the quantum dot sensor (ΔR/R of 6.6, Graph 3.2A) gives it significant potential to be developed as an intracellular calcium indicator, which our lab is actively pursuing.

Using a hexa-histidine tag (Figure 1) we were able to assemble calmodulin proteins onto quantum dot surfaces (Graph 3.1). The spontaneous complex formation in response to the exposure of different (charged) ligand (PEG, PEI and DHLA)-capped quantum dots facilitate the easy preparation of qdot-protein complexes and the determination of their protein binding stoichiometry. After examining the calcium binding sensitivity of the probes, we examined the unfolding characteristics of the calmodulin (CaM*-M13*). Treatment with EDTA reverted the closed calcium ion-bound conformation to an open structure (Graph 3.2B), as

indicated by the increase of the 610 nm / 670 nm intensity ratios. Our data suggest that in addition to the quantum dot-protein complex capacity as a sensor, it is also an excellent system with which to study the folding-unfolding properties of proteins for structural analysis. We also found that our quantum dot-calmodulin-based calcium sensor was very sensitive to the nature of the surface ligands. When we used longer surface ligands such as PEG (unpublished MW by Life Technologies) or PEI (MW = 2,000), there was almost no FRET response to calcium ion binding (Graph 3.3). This is in contrast to the shorter eight-carbon DHLA-capped quantum dots, which showed significant FRET at the same concentration of calcium ions (Graph 3.2A). The longer ligands probably prevent the folding of calmodulin by steric hindrance causing minimal FRET signals, which should be considered in the development of protein folding-based quantum dot sensors.

Quantum dot-based sensors are also well known for their excellent optical properties [26, 27] including superior photostability, a broad range of excitation wavelengths (ca 350 $\sim$ 550 nm), size-tunable narrow emission bands (full-width at half-maximum of about 25-40 nm), minimal crosstalk, long lifetimes, and adjustable optical cross-sections through varying numbers of attached acceptors. These features along with the large quantum dot surface area available for functionalization provide users considerable flexibility in the choice of excitation sources and optical filters, experimental duration, system multiplexing, and intracellular targeting.

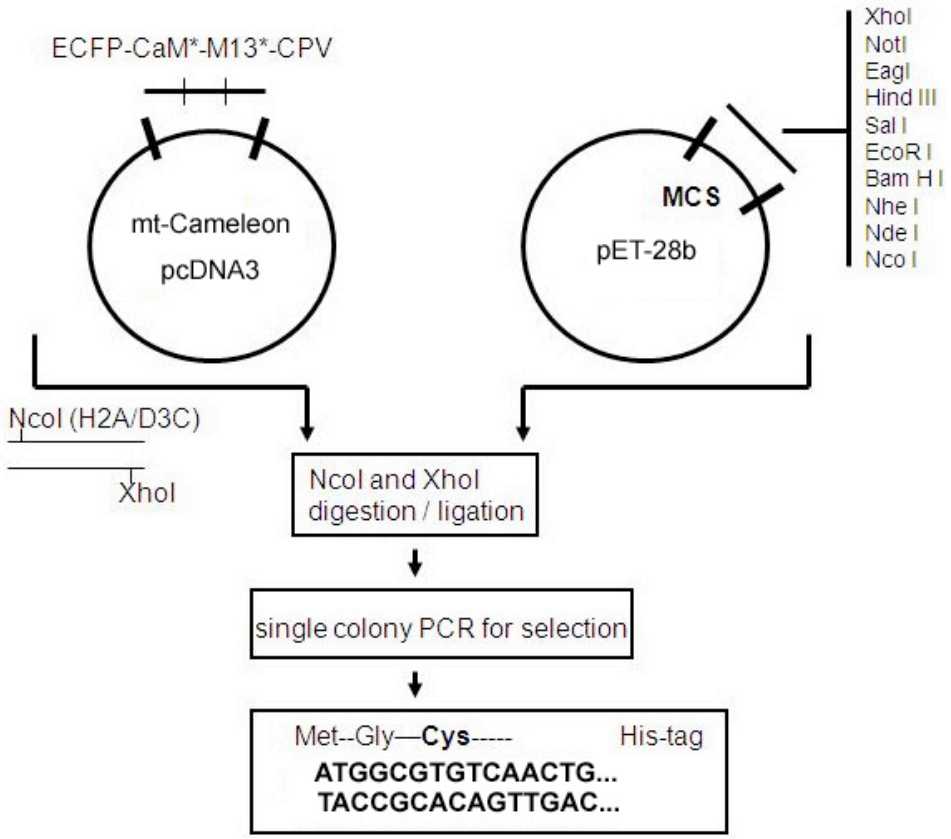

Figure 3.1: Summary of sub-cloning stages for CaM*-M13* proteins from mt-Cameleon/pcDNA3 to pET-28b vector. Wild-type (CaM*-M13*/pET-28b) and D3C mutant (CaM*-M13* D3C / pET-28b) were generated by PCR amplification.

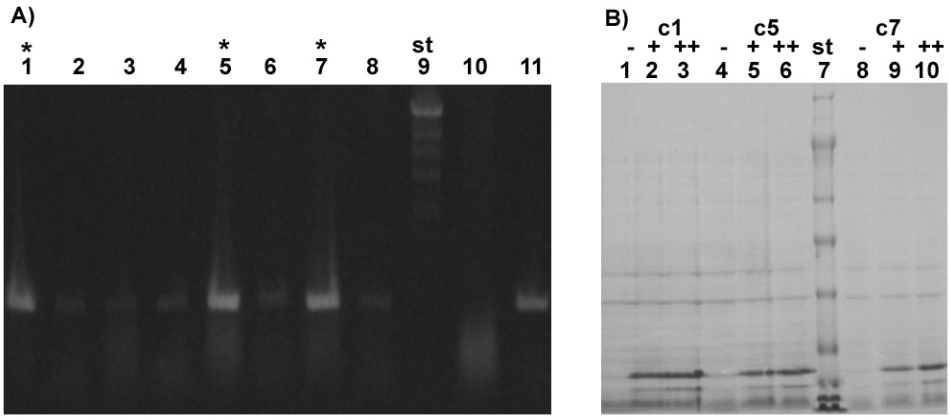

Figure 3.2: Plasmid delivery and expression. A) Single colony PCR screen for CaM*-M13 D3C clones and B) protein induction of the corresponding positive clones. A) 1 - 8. screened colonies, 9. HindIII DNA standard (st), 10. negative control (pET-28b vector in DH5 cells), 11. positive control (mt-Cameleon/pcDNA3 in DH5 cells). B) Protein induction patterns of the screened positive clones (* marked 1, 5 and 7 in A and c1, c5 and c7 in B) with (+) and without (-) IPTG. +, 2 hours IPTG induction, ++, 4 hours IPTG induction.

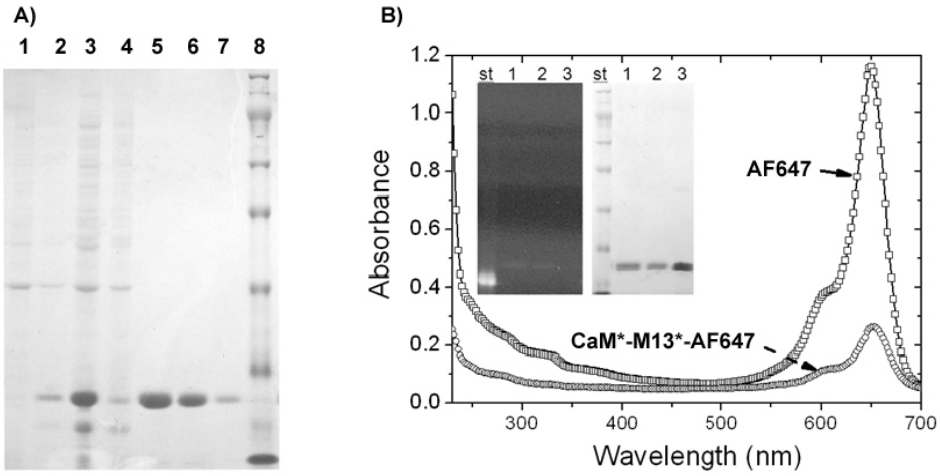

Figure 3.3: SDS-PAGE (10%) of the purification steps for CaM*-M13* D3C using a 300 ml culture. A) 1. - IPTG, 2. + IPTG (0.6mM, 4 hr), 3. load, 4. flow through, 5 - 7. eluted fractions, 8. protein standard B) Absorption spectra of free dye (AF647) and AF647 labeled CaM*-M13*. Inset) st. protein standard, 1,2 CaM*-M13*-AF647 at different concentrations, 3. Unlabeled CaM*-M13* D3C. SDS-PAGE was visualized by UV illumination (left) and commassie brilliant blue staining (right).

Graph 3.1: Titration of DHLA-qdot 610 with CaM*-M13*-AF647. The concentration of the quantum dots was 12.9 nM in 1.5 ml of 20mM Tris-HCl buffer, pH 8.0. Increasing amounts of 57.2 uM CaM*-M13*-AF647 were added to have protein to quantum dot molar ratios of 0, 0.99, 2.97, 5.91, 7.90 and 10.9 (top to bottom at 610 nm peaks at 25^{o}C. Excitation wavelength was 400 nm with photomultiplier high voltage set to medium.

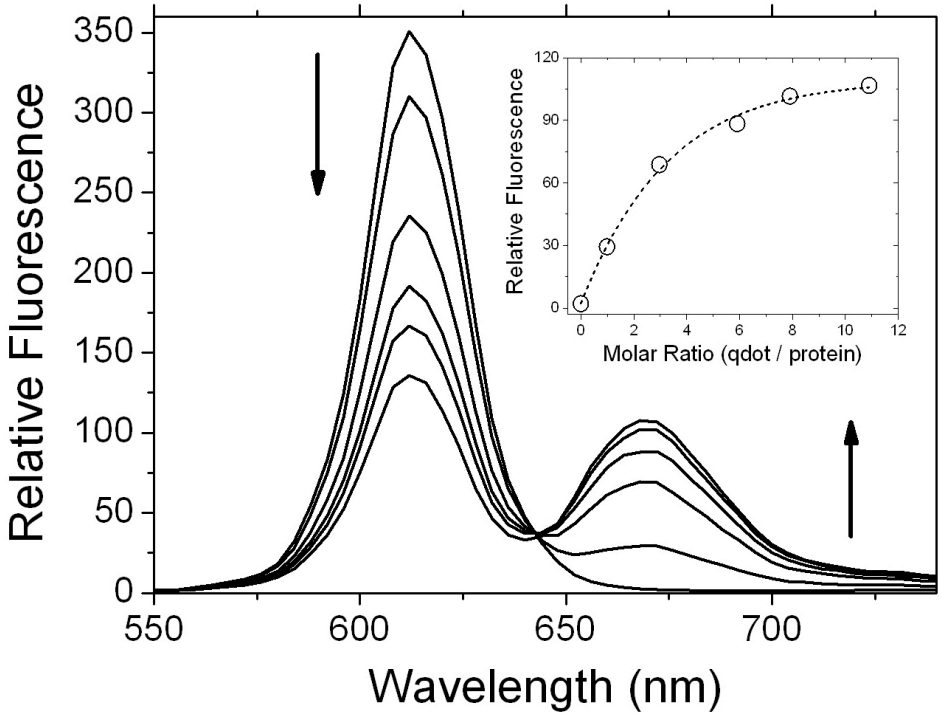

Graph 3.2: Calcium and EDTA induced folding and unfolding of calmodulin on the quantum dot surface. A) Calcium ion binding induced folding of CaM*-M13*-AF647 on the quantum dot surface as indicated by FRET from donor (qdot, 610 nm) to acceptor (AF647, 670 nm). Binding-induced decrease of the donor fluorescence at 610 nm and sensitized emission of acceptor (AF647) at 670 nm is observable. The concentrations of the calcium ions are indicated. B) EDTA induced unfolding of CaM*-M13*-AF647. Opening of the closed calmodulin structure is evidenced by the reversal of the calcium ion induced FRET. Decrease of acceptor (670 nm) and increase of donor (610 nm) fluorescence are observed. The concentrations of EDTA are indicated. The quantum dot to calmodulin molar ratio was 1 to 5.

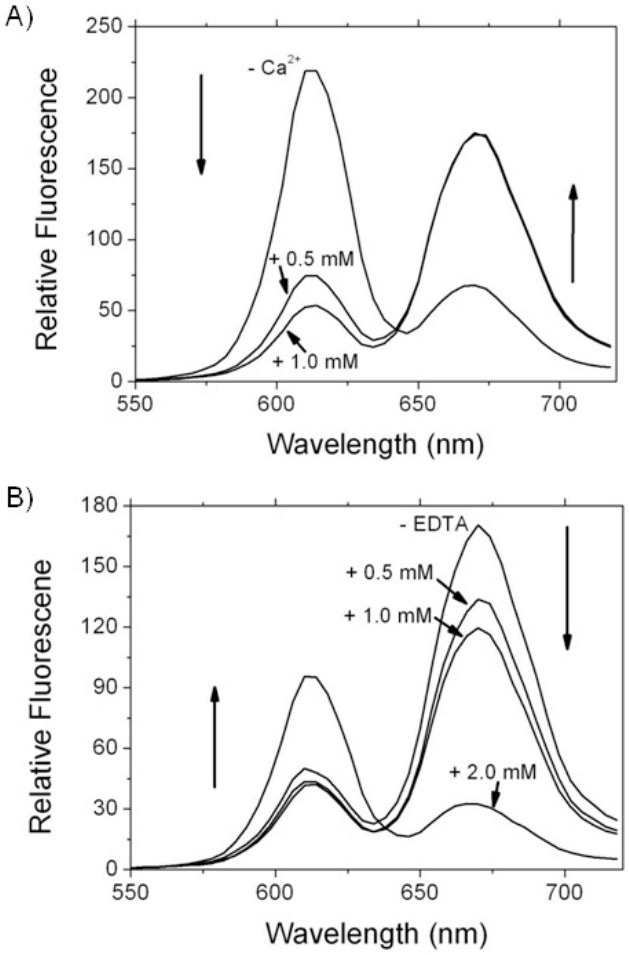

Graph 3.3: Effects of surface ligands on the binding and calcium induced folding of calmodulin. Fluorescence spectra PEG capped quantum dot (PEG-qdot) in the presence of calcium ions. Increasing amount of calcium ions decreased fluorescence peaks at both 605 nm and 670 nm. Inset) Fluorescence spectra of PEI (MW=2,000) capped quantum dot (PEI-qdot). Calcium ions have a minimal effect on the fluorescence peaks. Concentrations of calcium ions are indicated.

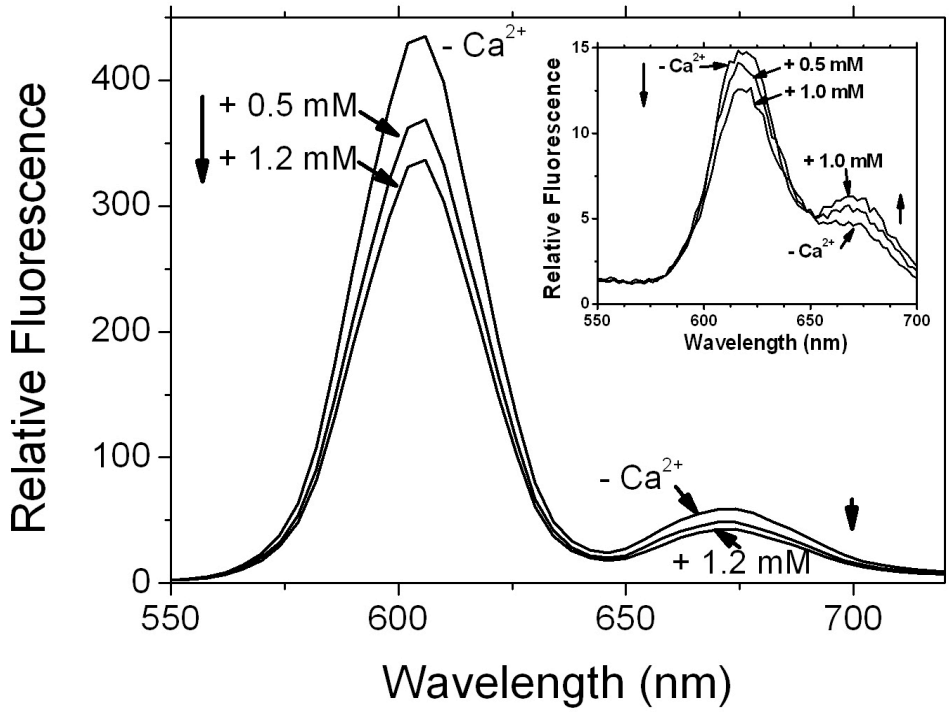

3.5 Acknowledgments

This work was funded by NIH grant RO1 NS054736 with a partial support from Mokpo National University exchange scholar program to S.-J. Kim. We would also like to thank Dr. Roger Tsien (University of California, San Diego) for kindly providing a mt-Cameleon/pcDNA3 plasmid used for CaM*-M13* probes.

Chapter 3, in full, is a reprint of the material as it appears in Kim, Soon-Jong; Blumling, James P.; Davidson, Marie C.; Saad, Helen; Eun, Su-Yong; Silva, Gabriel A. Calcium and EDTA induced folding and unfolding of calmodulin on functionalized quantum dot surfaces, Journal of Nanoneuroscience, in press. The dissertation author was second author of this paper.

3.6 References

1. Tsien, RY. A non-disruptive technique for loading calcium buffers and indicators into cells. *Nature*, 290(5806):527528, 1981.

2. Palmer, AE, Tsien RY. Measuring calcium signaling using genetically targetable fluorescence indicators. *Nature Protocols*, 1(3):1057-1065, 2006

3. Heim N, Garaschuk O, Friedrich MW, Mank M, Milos RI, Kovalchuk Y, Konnerth A, Griesbeck O. Improved calcium imaging in transgenic mice expressing a troponin C-based biosensor. *Nature Method*, 4(2): 127-129, 2007.

4. Rudolf RR, Mongillo M, Rizzuto R, Pozzan T. Looking forward to seeing calcium. *Nature Review: Molecular Cell Biology*, 4(7):579-586, 2003.

5. Mank M, Griesbeck O. Genetically Encoded Calcium Indicators. *Chemical Reviews*, 108(5):1550-1564, 2008.

6. Miyawaki A, Llopis J, Heim R, McCaffery JM, Adams JA, Ikurak M, Tsien RY. Fluorescent indicators for Ca2+ based on green fluorescent proteins and calmodulin. *Nature*, 388(6645):882-887, 1997.

7. Truong K, Sawano A, Mizuno H, Hama H, Tong KI, Mal TK, Miyawaki A, Ikura M. FRET-based in vivo calcium imaging by a new calmodulin-GFP

fusion molecule. *Nature Structural and Molecular Biology*, 8(11):1069-1073, 2001.

8. Chin D, Means AR. Calmodulin: a prototypical calcium sensor. *Trends in Cell Biology*, 10(8):322328, 2000.

9. Chou JJ, Li SP, Klee CB, Bax A. Solution structure of Ca2+-calmodulin reveals flexible hand-like properties of its domains. *Nature Structural and Molecular Biology*, 8(11):990-997, 2001.

10. McCombs JE, Palmer AE. Measuring calcium dynamics in living cells with genetically encodable calcium indicators. *Methods*, 46(3):152-159, 2008.

11. Palmer AE, Giacomello M, Kortemme T, Hires S, Lev-Ram V, Baker D, Tsien R. Ca2+ indicators based on computationally redesigned calmodulin-peptide pairs. *Chemistry & Biology*, 13(5):521530, 2006.

12. Shafer DE, Inman JK, Lees A. Reaction of tris(2-carboxyethyl)phosphine (TCEP) with maleimide and -haloacyl groups: anomalous elution of TCEP by gel filtration. *Analytical Biochemistry*, 282(1):161164, 2000.

13. Yu WW, Qu L, Guo W, Peng X. Experimental determination of the extinction coefficient of CdTe, CdSe, and CdS nanocrystals. *Chemistry of Materials*, 15(14):2853-2860, 2003.

14. Duan H, Nie S. Cell-penetrating quantum dots based on multivalent and endosome-disrupting surface coatings. *Journal of the American Chemical Society*, 129(11):3333-3338, 2007.

15. Medintz IL, Clapp AR, Mattoussi H, Goldman ER, Fisher B,Mauro JM. Self-assembled nanoscale biosensors based on quantum dot FRET donors. *Nature Materials*, 2(9):630-683, 2003.

16. Dennis AM, Bao G. Quantum dot-fluorescent protein pairs as novel fluorescence resonance energy transfer probes. *Nano Letters* 8(5):1439-1445, 2008.

17. Delehanty JB, Medintz IL, Pons T, Brunel FM, Dawson PE, Mattoussi H. Self-assembled quantum dot-peptide bioconjugates for selective intracellular delivery. *Bioconjugate Chemistry* 17(4):920-927, 2006.

18. Sapsford KE, Pones T, Medintz IL, Higashiya S, Brunel FM, Dawson PE, Mattoussi H. Kinetics of metal-affinity driven self-assembly between proteins or peptides and CdSe-ZnS quantum dots. Journal of Physical Chemistry C, 111(31):11528-11538, 2007.

19. Mattoussi H, Mauro JM, Goldman ER, Anderson GP, Sundar VC, Mikulec FV, Bawendi G. Self-assembly of CdSe-ZnS quantum dot bioconjugates using an engineered recombinant protein. *Journal of the American Chemical Society*, 122(49):12142-12150, 2000.

20. Lakowicz JR. Principles of Fluorescence Spectroscopy, 2nd Edition. Kluwer, New York, 1999.

21. Reiff DF, Ihring A, Guerrero G, Isacoff EY, Joesch M, Nakai J, Borst A. In vivo performance of genetically encoded indicators of neural activity in flies. *Neuroscience*, 25(19):4766-4778, 2005.

22. Levy M, Cater SF, Ellington AD. Quantum-dot aptamer beacons for the detection of proteins. *ChemBioChem*, 6(12):2163-2166, 2005.

23. Zhang CY, Johnson LW. Quantum-dot-based nanosensor for RRE IIB RNA-Rev peptide interaction assay. *Journal of the American Chemical Society*, 128(16):5324-5325, 2006.

24. Xu CJ, Xing BG, Rao HH. A self-assembled quantum dot probe for detecting beta-lactamase activity, *Biochemical and Biophysical Research Communications*, 344(3):931935, 2006.

25. Clapp AR, Goldman ER, Uyeda HT, Chang EL, Whitley JL, Medintz IL. Monitoring of enzymatic proteolysis using self-assembled quantum dot-protein substrate sensors. *Journal of Sensors*, 2008:1-10, 2008.

26. Michalet X, Pinaud FF, Bentolila LA, Tsay JM, Doose S, Li JJ, Sundaresan G, Wu AM, Gambhir SS, Weiss S. Quantum dots for live cells, in vivo imaging, and diagnostics. *Science*, 307(5709):538-544, 2004.

27. Mazumder S, Dey R, Mitra MK, Mukherjee S, Das GC. Review: biofunctionalized quantum dots in biology and medicine. *Journal of Nanomaterials*, 2009:1-17, 2009.

Chapter 4

Cell penetrating peptide-mediated delivery of quantum dots to cortical astrocytes

4.1 Introduction

The delivery of molecules and particles across the cell membrane is often a difficult task, especially since most molecules of interest are not hydrophobic and cannot diffuse passively through it. This has led to the implemetation of a number of physical and chemical approaches to circumventing cell membranes. These include microinjection, electroporation, sonoporation, osmotic shock, attachment of poly(ethylene glycol) (PEG) or other membrane permeable molecules, and the use of cell-penetrating peptides (CPPs). Microinjection works well, but requires great technical expertise, is extremely time-consuming, and is impossible to utilize on a large field of cells. Electroporation and sonoporation often have limited efficiency and/or a high rate of cell death depending on implementation [1]. Osmotic shock also requires carefully designed protocols to avoid cell death, while yielding efficient delivery [2], and has seen little use with nanoparticles, possibly a sign of limited success with a broad range of cell types. PEGylation works well for both small and large molecules (like DNA), but it may not function as well for large nanoparticles; it is harder to get larger objects to pass through the membrane in a diffusive manner. On the other hand, CPPs have shown wide success in delivering cargoes over a range of sizes, from small molecules to large particles [3-6]. Our interest in efficient delivery nanodevices to many cells simultaneously led us to explore CPPs in neural cells.

CPPs are a general class of short peptides (typically less than 30 amino acids [3]) that can translocate across the cell membrane through a variety of means. Some induce forms of endocytosis, while others purportedly cause transient deformations in membrane architecture allowing cargo to pass through. We focused our study on the widely used synthetic CPP polyarginine (polyR; Table 4.1) [4,7-10]], due to its simple structure and the ease with which one could tailor it, although we

also considered the HIV-1-derived Transactivator of Transcription (TAT) peptide [11, 12], due to its extensive use [13-15], as well as a fragment derived from rabies virus glycoprotein (RVG), as it is known to bind the acetylcholine receptor and promote trafficking into the central nervous system (CNS) across the blood-brain-barrier [16].

Our RVG sequence provided for little cell penetration, and while the TAT worked well (data not shown), literature reports of its potential to cause oxidative stress in neural cells [17-19] narrowed our views onto polyR, which also provided for a high level of cell penetration (Figures 4.1 and 4.2). Given promising results with polyR, we attempted to optimize our protocol and investigate the delivery more closely. We considered the effect of peptide length, peptide concentration, incubation buffer, and incubation temperature on delivery efficiency. We chose these parameters due to their ease of control, likelihood of impact on delivery, and the potential insight experimental results could provide. Additionally, we studied transmission electron micrographs to assess the localization of delivered nanoparticles.

4.2 Results and Discussion

4.2.1 Exploration of PolyR

Length. PolyR's simple structure as a sequence of arginine residues permits tailoring of delivery efficiency through the addition or removal of arginines from an optimal length. The literature places this optimal length between 8 and 9 residues [7, 8], however, we were uncertain of the effect of a rather large quantum dot on the behavior of the CPP. As such, we investigated two lengths, 8 (R8; Table 4.1) and 11 (R11; Table 4.1). Our theory was that the QD coating might inhibit the

functionality of nearby residues, and the addition of a few extra might improve the efficacy of delivery. The choice of 11 residues was somewhat arbitrary; we wanted to add as few residues as possible to minimize cost, while still achieving enough change in relative length to reasonably expect a change in delivery efficiency. We were fortunate in our choice, and did in fact see a significant change in efficiency. Moreover, our hypothesis was given credibility as cells treated with QD-R11 complexes displayed greater fluorescence than those treated with the QD-R8 counterpart at all measured time points, and only one of those proved not to be statistically significant (Graph 4.1).

Concentration. To create the QD-R11 particles, hydrophilic QDs were incubated with a defined ration of histidine-tagged peptide; the tag provided for metal-affinity binding to the QD surface [20]. By varying the stoichiometry, we could affect the number of peptides per QD. As such, it seemed prudent to determine the optimal QD:R11 ratio for cell delivery. Four ratios were investigate: 1:12.5, 1:25, 1:50, 1:100. During the first 4 hours of incubation, little distinction could be made between fluorescences, and at later time points only 1:12.5 appeared to yield noticeably less fluorescence (Graph 4.2). Since most experiments would be carried out with at most a 4-hour incubation, it is likely that any of the ratios would suffice, and from a utility standpoint, using the minimum amount of peptide is preferrable (1:12.5). However, for longer incubation times, or just to err on the side of caution, 1:25 appears to be the optimal choice.

Buffer. QD-R11 complexes were incubated with cells under four different buffer conditions: phosphate buffered saline (PBS), Hank's balanced salt solution without calcium and magnesium (HBSS-), Hank's balanced salt solution with calcium and magnesium (HBSS+), and culture medium. The intent of these choices was to pro-

vide a range of starvation: PBS being completely a completely starved condition, HBSS- providing some important inorganice ions, HBSS+ additionally providing calcium and magnesium, and culture medium providing all essential nutrients. To minimize starvation-induced cell death, observations were made at two and four hours only, with no later time points. The results indicate starvation increases uptake of the QD-R11 complex (Graph 4.3), possibly due to a negative impact on membrane integrity. The improved delivery in HBSS- versus HBSS+ supports the notion of pinocytosis (although the differences were not statistically significant), as the process has been shown to be inhibited by the addition of calcium ions [21]. The morphology of the astrocytes in PBS was atypical, suggesting cell viability was compromised, although morphology was preserved in HBSS for several hours (data not shown). Taking all this into account, HBSS appears to be the best buffer for a high delivery rate with minimal effect on cell viability; however, the improvement over efficiency in culture medium may not be enough to warrant any increase in cell death, depending on the application. The results are encouraging in another respect, as well: starved conditions only increase uptake by about two-fold, suggesting that *in vivo* application of these types of complexes will not suffer greatly from an inability to produce effective starved conditions.

Temperature. Our interest in temperature effects was to gain insight into potential methods of internalization. Obviously, physiological temperatures are optimal for cell viability and more or less essential for any *in vivo* applications, but the effects of lower temperature on internalization can yield information as to the importance of active transport mechanisms on QD-R11 delivery. Incubations were performed and room temperature (25^{o}C) and physiological temperature (37^{o}C), and fluorescence was observed at two and four hours. At both time points, there

was significantly more internalization at 37^{o}C (Graph 4.4). This implies a significant dependance of internalization on active (endocytic) pathways, since enzymes and proteins involved function optimally at biological temperatures [22]. If the process were heavily passive (i.e. diffusive or involving some direct membrane-peptide interaction), the small shift in absolute temperature would have had little effect. The results suggest pinocytosis as the likely path to internalization, since the synthetic peptide is probably not specific to any receptor and hence would not initiate phagocytosis of receptor-mediated endocytosis.

4.2.2 Transmission Electron Microscopy (TEM).

In order to potentially confirm our suspicions about the nanoparticle delivery, as well as to determine if any of the complexes find their way into the cytosol, we obtained a series of TEM images. Images were taken after incubation for 4 hours and 24 hours to assess where the complexes tended to accumulate, both initially and later on. Careful inspection of the images reveals that the majority end up in vesicles, which tended to fuse into large vacuoles by 24 hours (Figure 4.3), this is in agreement with the assumption of pinocytosis and parallels findings in A549 cells [9].

Some QD-R11 could be found in the cytoplasm, but with the bulk inside vesicles, any fluorescence-based sensing from free nanodevices would be drowned out by background from those that are trapped. Still, there is potential for this system, as methods exist that may break down the endosomes or improve nanoparticle escape. We made an attempt at this utilizing an R11 peptide that also contained a nuclear localization sequence (NLS; Table 4.1), R11-NLS [23]. Overall delivery was still efficient (Graph 4.5), and some of the complexes appeared to have found their way to the nucleus by the 24 hour mark (Figure 4.4), but the majority remained

within vesicles.

4.2.3 Implications and Future Work

This work has demonstrated the potential for synthetic polyR CPPs to deliver large cargo across the membranes of astrocytes. It does appear that the majority are trapped within vesicles; however, incorporation of various localization sequences or tandem delivery approaches may improve escape and intracellular targeting. One might include additional surface molecules shown to aid vesicle escape (e.g. branched polyamines or poly(amido amines) [24, 25]) or follow CPP delivery with osmotic shock, electroporation, or sonoporation; the tandem approach may permit much milder stimulation, minimizing the cell death often associated with physical delivery methods.

The sequestration of polyR CPPs within astrocytes warrants revisiting TAT (in spite of potential oxidative stress) and other CPPs, although any that induce macropinocyotosis are likely to have the same final destination. It would be greatly beneficial to neuroscience, if we could efficiently deliver nanodevices across neural membranes. A great deal of mystery still surrounds the inner working of neural networks and the exchange of information between cells. Nanotechnology offers the potential for novel, superior sensors of action potentials and cellular interactions/responses, but, in order to utilize these devices effectively, we need to be able to apply them to a large group of cells quickly and with minimal cell damage.

For our group, initial investigations into astrocytes were of particular interest as we study calcium signals in glial cells. We recently developed a QD-based calcium sensor that may be useful in characterizing calcium microdomains known to exist within neural cells, astrocytes in particular [26, 27]. Naturally, being able to deliver these sensors to a field of glial cells in a network and observe local in-

tracellular calcium transients would be a great boon to the understanding of glial functionality in the central nervous system. Steps such as this are essential to fully grasping information processing in the brain.

4.3 Methods

Cell culture. All experiments were carried out in accordance with approved protocols from the Institutional Animal Care and Use Committee of the University of California (San Diego, CA). Primary cortical cultures were prepared from postnatal day 1 Sprague-Dawley rats (Harlan Sprague Dawley, Indianapolis, IN). The pups were euthanized by anesthesia overdose. Their heads were decapitated, the brains were removed and cerebral cortices dissected in sterile dissociation media (DM). Cells were mechanically dissociated in DM (Table 4.2) through a 70 μm cell strainer (BD Biosciences, San Jose, CA) and cultured in MEM (Gibco/Invitrogen, Carls- bad, CA) supplemented with 10 percent FBS (Gibco/Invitrogen, Carlsbad, CA), 1 percent glutamax (Gibco/Invitrogen, Carlsbad, CA), and 1 percent pen/strep (Gibco/Invitrogen, Carlsbad, CA) onto a 10 cm petri dish (BD Biosciences, San Jose, CA). Once the cell cultures reached desired confluency (approximately 80 per- cent), cells were removed mechanically using a cell scraper (Corning Incorporated, Corning, NY). Astrocytes were seeded on 24-well glass bottom plates (MatTek Corp., Ashland, MA) at a density of 1.6 x 104 cells/well and incubated at 37^{o}C and 5% CO2. With regards to the temperature-dependent and electron microscopy experiments, cells were seeded onto 35 glass bottom culture dishes (MatTek Corp., Ashland, MA) at a density of 1.5 x 104 cells/well. For immunocytochemistry studies, cells were grown on glass cover slips seated in a 24-well tissue culture plate (Becton Dickinson, Franklin Lakes, NJ) at a density of 1 x

104 cells per well. Culture media for all experiments was changed twice per week (50% removed, 50% new), and all cultures were used within three passages. Cells were grown and considered ready for experiments at 50% confluency or greater.

Immunocytochemistry. Immunocytochemistry (ICC) was performed on astrocyte cultures identical to those used for fluorescence imaging. Cells were fixed in 4% paraformaldehyde (Electron Microscopy Sciences, Hatfield, PA) for 15 minutes and washed twice with phosphate buffered saline (PBS; Invitrogen, Carlsbad, CA). Cultures labeled for glial fibrillary acidic protein (GFAP) were permeabilized in 1% horse serum (Gibco/Invitrogen, Carlsbad, CA) and 0.2% Triton X-100 (Fisher Scientific Inter- national, Hampton, NH) for 30 mintues before incubation with anti-GFAP primary antibodies (1:100 dilution; Sigma, St. Louis, MO) with 10% HS in PBS overnight. Routine negative controls included the omission of the primary antibody and in- cubation with 10% HS in PBS during the primary incubation step. For secondary antibody labeling, cells labeled for GFAP were incubated with tetramethylrho- damine isothiocyanate (TRITC) conjugated anti-mouse IgG (1:200; Sigma, St. Louis, MO). Following the ICC, all slides were mounted using Molecular Probes Prolong Gold antiface reagent with DAPI (Eugene, OR). Images were acquired with the same hardware and software as described previously and viewed using filters for TRITC and DAPI. Astrocyte isolation was confirmed (data not shown).

Live-dead assay. To determine whether cells were viable, a live/dead assay was performed on cells (Invitrogen, Carlsbad, CA). When cell were ready to be tested, cell media is aspirated, and the cells are washed with HBSS once to remove remaining growth media. A mixture of 3μM EthD-1 (dead dye) and 1μM calcein AM (live dye) is added to HBSS and incubated with cells for 20 minutes at 37^{o}C

in 5% CO2 environment. Following the live/dead solution, The live/dead dyes in HBSS were aspirated from cells, and 3.5μg/mL of Hoechst 33342 (Invitrogen, Carlsbad, CA) in HBSS was further incubated with the cells for 5 minutes at 37^{o}C in 5% CO2. The solution was then aspirated and replaced with HBSS for microscopy imaging [28]. Images were acquired with the same hardware and software as described previously and viewed using filters for DAPI, FITC, and TRITC.

Histidine-tagged CPP assembly on QDs. 605nm eFlour amine-functionalized nanocrystals (eBioscience, San Diego, CA) were briefly centrifuged prior to use. The peptide of interest (R11, R8, NLS) was evenly mixed prior to use. Stoichiometric concentrations of QDs and peptides were premixed in a microcentrifuge tube (Dot Scientific, Burton, MI) and allowed to self-assemble at 4^{o}C for one hour or longer. CPPs were tagged with a polyhistidine sequence (6 residues) to enable metal-affinity binding to the quantum dot surface [21]. All peptides were synthesized and obtained from Biomatik Corp. (Cambridge, Ontario, Canada).

QD-CPP concentrations and conditions The R11 peptide was tested at four different stoichiometric concentration ratios of 1:12.5, 1:25, 1:50, and 1:100 (QD:peptide). Note that for each individual well or dish (in all experiments), the actual concentration of QDs used was 6 pmol. Furthermore, each concentration ratio was subjected to six different incubation time points: 1-hour, 2-hour, 4-hour, 8-hour, 12-hour, and 24-hour. The control for this experiment was treated with unconjugated QDs with the same concentration (6 pmol) per well, and also subjected to the same six incubation time points above.

To determine polyarginine length effects on QD internalization, peptides R8 and R11 were compared against each other using the same stoichiometric ratio of 1:25 (QD:peptide), and tested at six different time points: 1-hour, 2-hour,

4-hour, 8-hour, 12-hour, and 24-hour. To compare delivery efficiency between different peptides, R11 and R11-NLS were tested at a stoichiometric ratio of 1:25 (QD:peptide) at two different time points: 2-hour, and 24-hour.

To determine buffer effects on QD internalization, R11 with a stoichiometric ratio of 1:25 (QD:peptide) was used. The buffers tested include cell culture media, HBSS with (+) and without (-) calcium and magnesium, and PBS. All conditions were tested at two different time points: 2-hour and 4-hour.

To determine temperature effects on QD internalization, the R11 peptide with a stoichiometric ratio of 1:25 (QD:peptide) was used in all cases. The two different temperatures tested was 37^{o}C and 25^{o}C in a CO_2 environment. All conditions were tested at two different time points: 2-hour and 4-hour.

A transmission electron microscopy (TEM) study was performed to confirm the uptake of QDs. All peptides in this experiment were kept at a stoichiometric ratio of 1:25 (QD:peptide). The R11 peptide was subjected to two time points: 4-hour and 24-hour, while the NLS and ER peptides were only subjected to a 24-hour time condition. A control cell culture dish with no treatment was also tested.

Delivery of QD-CPP to astrocytes For all experiments (unless otherwise noted), 300μl of cell media was added to the QD-CPP premixture to yield the treatment media. All contents were briefly mixed by vortexing prior to beginning the experiment. The tested wells or dishes were gently aspirated, treatment media was added, and the cells were incubated with the desired incubation time. Following treatment, all wells/dishes were gently aspirated, washed once with PBS, and then rinsed three times for three minutes each with cell media. Cells were replaced with fresh cell media and immediately visualized with via fluorescence microscopy.

Fluorescence microscopy. Visualization of the quantum dots was done using a 605 nm quantum dot filter on an Olympus IX inverted fluorescence confocal microscope (Olympus Opti- cal, Tokyo, Japan) that included epifluorescence, confocal, phase, brightfield, and Hoffman differential interference contrast (DIC) modalities. Images were all acquired using a x20 UPlanFLN objective (NA = 0.5; Olympus Optical) with an acquisition time of 5 ms using a Hamamatsu ORCA-ER digital camera (Hamamatsu Photonics K.K., Hamamatsu City, Japan) and a custom-written LabVIEW (National Instruments, Austin, TX) software developed in our laboratory.

Transmission electron microscopy. Following QD-peptide treatment, cell media was aspirated from the dish and fixative (2% glutaraldehyde in 1x0.1M sodium cacodylate buffer pH 7.4) was added. Fixed cells remained in 4^oC refrigerator until processing began. All of the following procedures were carried out on ice. The sample was briefly washed three times for 3 minutes each in 0.1M SC buffer. It was then incubated with 1% OsO4 in 0.1M SC buffer for 30 minutes following another 3 repeats of washing, and then rinsed in dH2O two times for 1 minute each. The sample was incubated with 2% uranyl acetate (UA) in dH2O for 30 minutes, then rinsed with dH2O. It was then dehydrated in ETOH 20%, 50%, 70%, and 90% two times for 1 minute each. The rest of the steps were carried out in room temperature. The sample was incubated in a mixture of ETOH and Durcupan epoxy (50:50) for 1 hour, then 100% Durcupan for 1 hour. The embedded cells are then placed in a 60^oC oven overnight. 85nm thick sections were cut on Leica Ultracut UCT microtome and collected on 200 mesh copper grids. Sections were stained with 2% UA (in dH2O) for 5 minutes and Sato Lead for 1 minute. The EM evaluation was carried out on a JEOL 1200 EX.

Quantitative image analysis. Using ImageJ, a Java-based image processing program (rsbweb.nih.gov/ij/), the free-select total was modified to allow manual selection of individual cells on the xy-plane of each image. Each cell was considered as an individual region of interest (ROI). An ImageJ plugin was used to calculate the average intensity for each ROI in each image. All of this data was organized in matrix format for postprocessing analyses. We assumed that the QD fluorescence intensity was proportional to the amount of QDs that internalized. All graphs were generated using Matlab (Mathworks, Natick, MA) and the analysis of variance (ANOVA) test was used to determine statistical significance (p¡0.05) between data sets.

Table 4.1: Polyarginine CPP sequences. The NH_2 and COOH denote the amine and carboxyl terminals, respectively. Each peptide included an amino-terminal cysteine with a glycine spacer to provide a thiol for derivatization (e.g. for incorporation of another fluorophore), a tryptophan residue with glycine spacers for UV spectroscopic analysis, and a polyhistidine carboxy-terminal for metal-affinity binding to quantum dot surfaces (6 residues). The additional sequence in R11-NLS (PPKKKRKV) is a nuclear localization sequence.

R8	NH_2-CG-RRRRRRRR-GWG-HHHHHH-COOH
R11	NH_2-CG-RRRRRRRRRRR-GWG-HHHHHH- COOH
R11-NLS	NH_2-CG-PPKKKRKV-RRRRRRRRRRR-GWG-HHHHHH-COOH

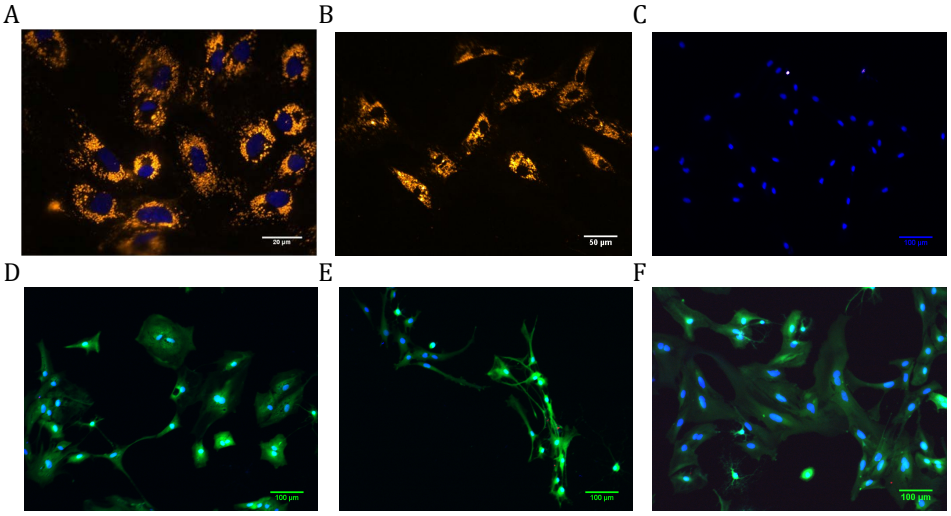

Figure 4.1: QD delivery to cortical astrocytes with polyarginine. A-C) Fluorescence micrographs of QD delivery with R11, R11-NLS, and no peptide, respectively. D-F) Fluorescent micrographs of live/dead staining of astrocytes subject to QD delivery with R11, R11-NLS, and no peptide, respectively. Blue dots indicating nuclei are the result of Hoechst staining. Images were obtained after 24-hour incubations with QD complexes.

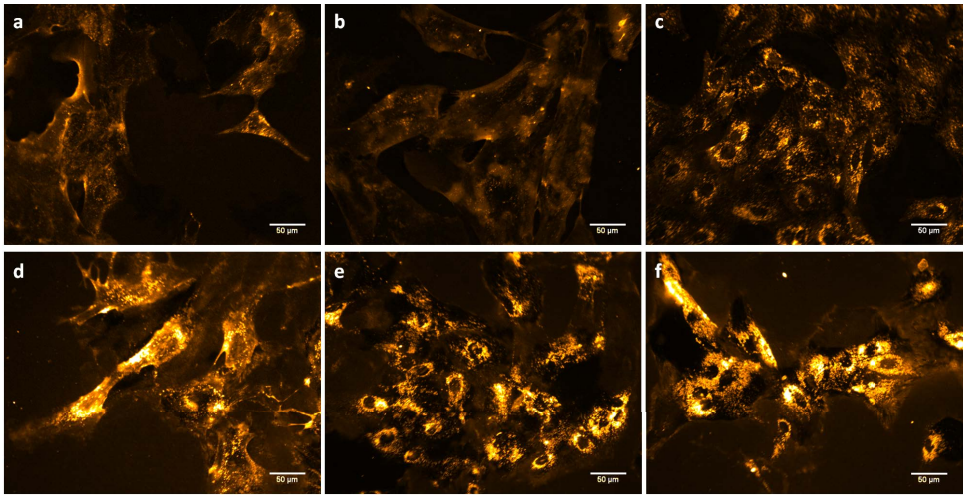

Figure 4.2: Time lapse of QD delivery with polyarginine. A-F) Fluorescence micrographs of QD delivery with R11 at 1, 2, 4, 8, 12, and 24 hours, respectively.

Graph 4.1: Comparison of R8 and R11 delivery efficiency.
* p-value < 0.05 ** p-value < 0.01

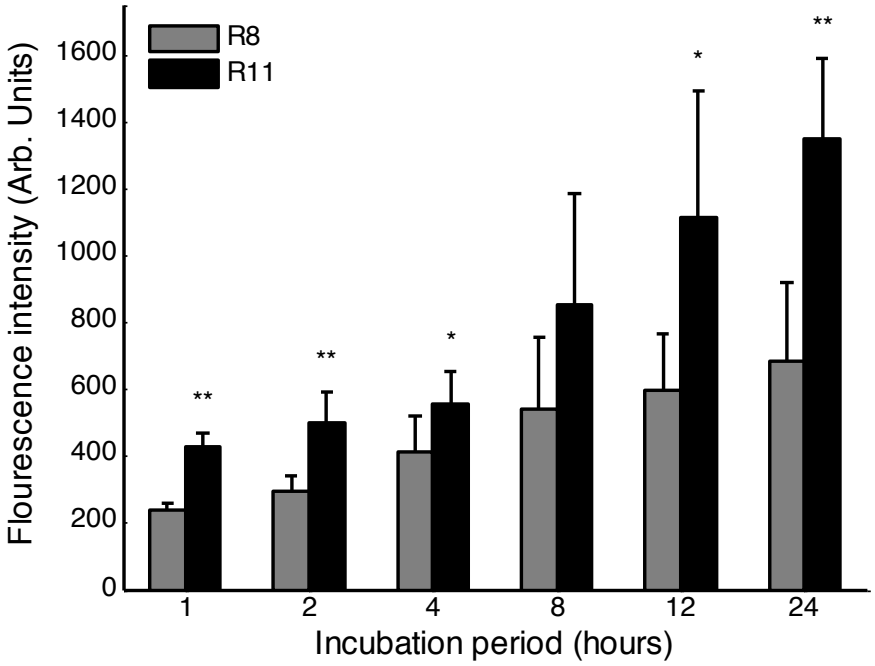

Graph 4.2: Effects of stoichiometry on R11 delivery. Fluorescence of QD-R11 treated cells given four different stoichiometries of QDs to R11 peptides: 1:12.5, 1:25, 1:50, and 1:100. By 8 hours, 1:50 and 1:100 are significantly more fluorescent (p-value < 0.05) than 1:25. At 12 and 24 hours, 1:25, 1:50, and 1:100 all display significantly greater fluorescence than 1:12.5 (p-value < 0.05).

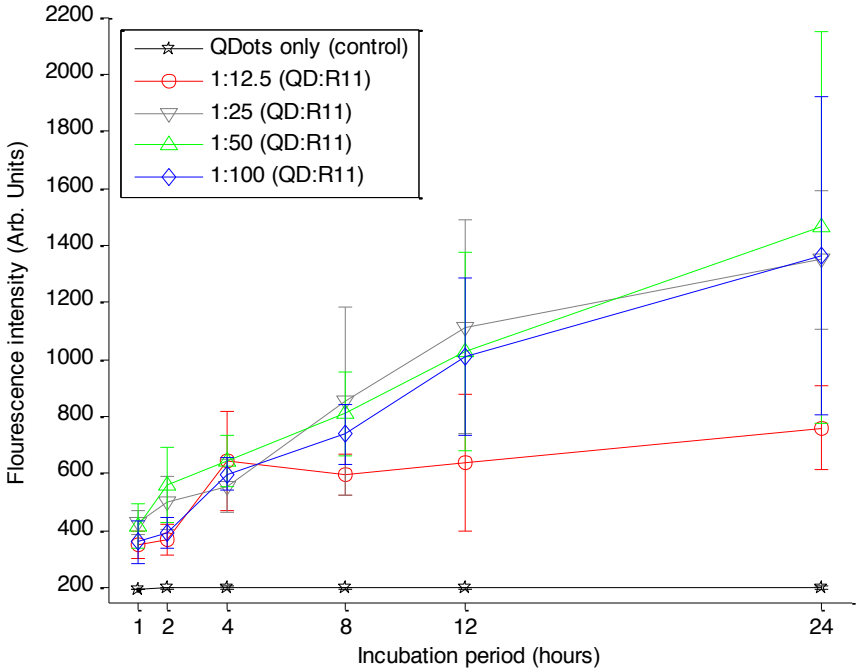

Graph 4.3: Effects of buffer on R11 delivery. Fluorescence of cells treated with QD-R11 treated under four different buffer conditions: PBS, HBSS-, HBSS+, and culture media. Differences between bars indicated by horizontal black lines have a p-value < 0.05.

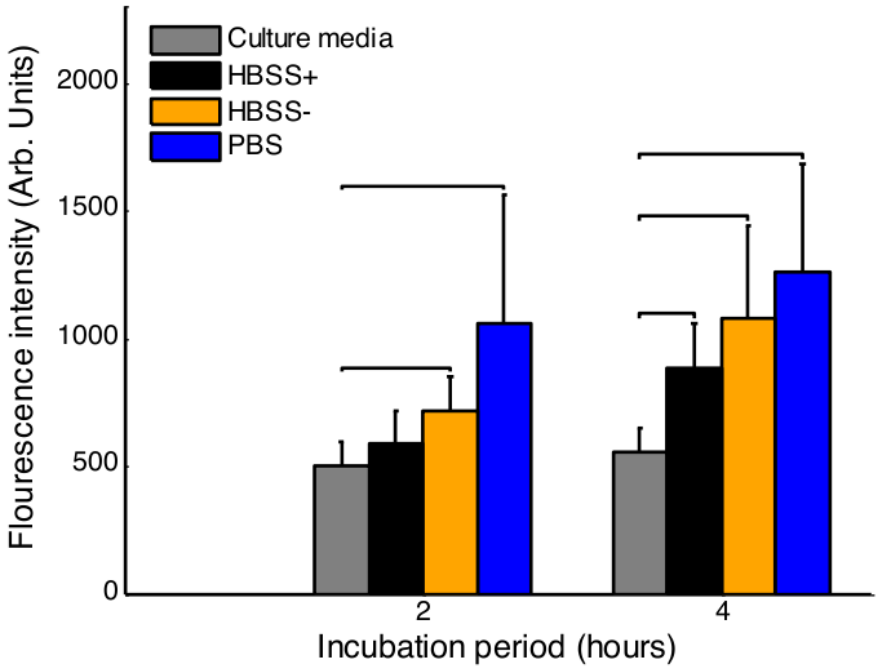

Graph 4.4: Effects of temperature on R11 delivery. Fluorescence of cells treated with QD-R11 incubated at 25^{o}C and 37^{o}C.
* p-value < 0.05 ** p-value < 0.01

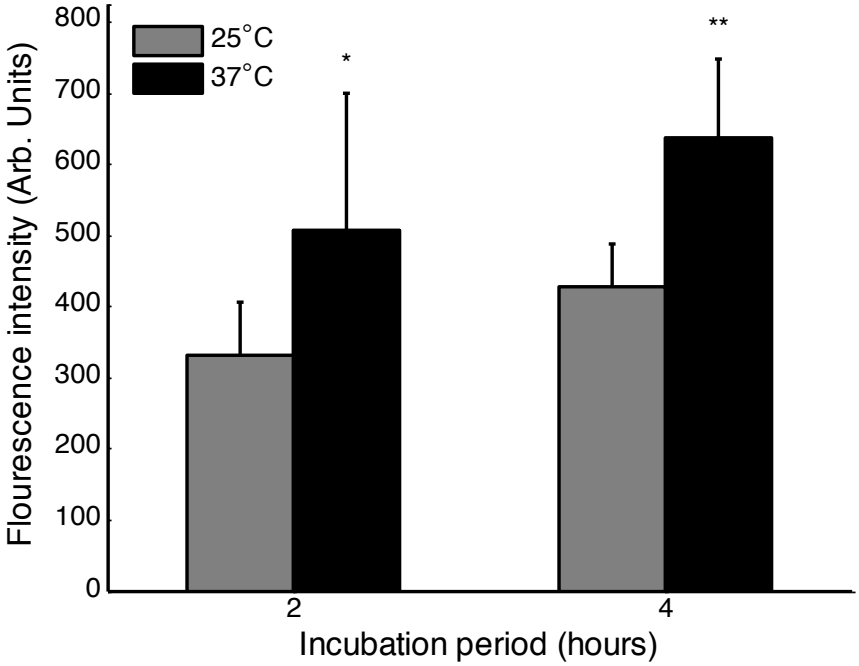

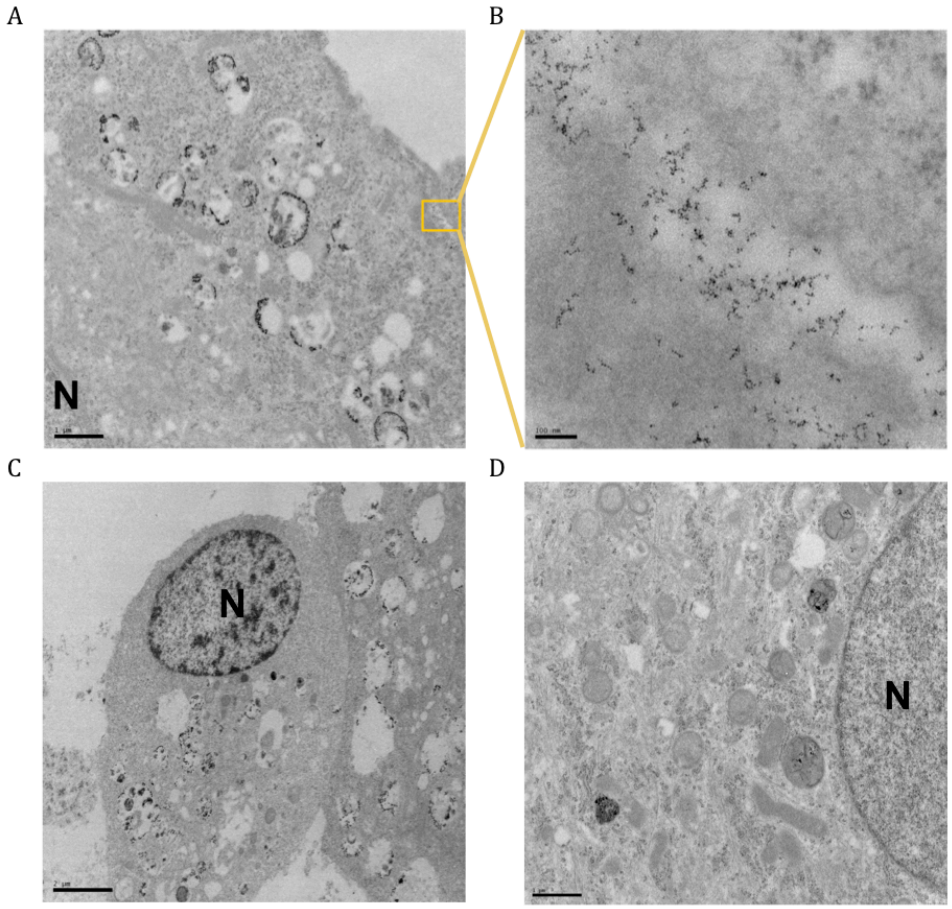

Figure 4.3: Transmission elctron micrographs of QD-R11 in astrocytes. A) Image of a cell treated with QD-R11 complexes for 4 hours. The dark regions at the perimeter of the numerous vesicles are indicative of the dense semiconductor cores of the QDs. B) A zoomed in image of a local region (yellow box) from A depicting some free QDs in the cytosol. C) Image of a cell treated with QD-R11 complexes for 24 hours. Apparent vesicle fusion resulted in the formation of large vacuoles and a distorted cell architecture. D) Image of a typical untreated astrocyte. The scale bars of A-D are 1, 0.1, 2, and 1 μm, respectively. Nuclei are labeled N for clarity.

Graph 4.5: Comparison of R11 and R11-NLS delivery efficiency.
* p-value < 0.05 ** p-value < 0.01

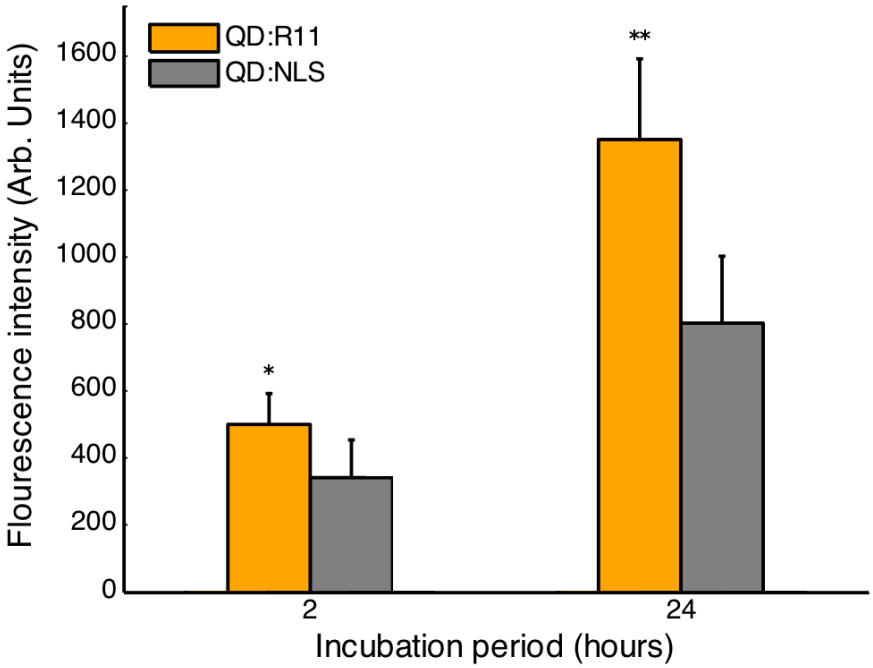

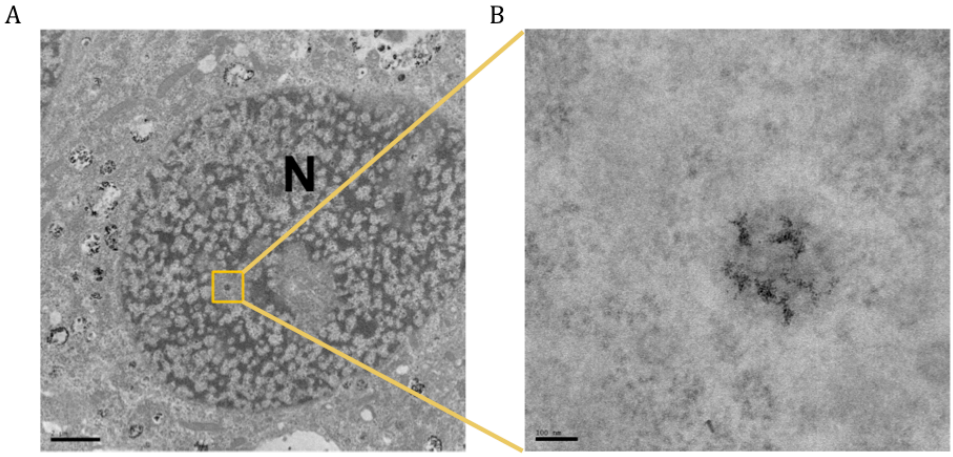

Figure 4.4: Transmission electron micrographs of QD-R11-NLS in astrocytes. A) Image of a cell treated with QD-R11-NLS for 24 hours. Most QDs appear at the perimeter of vesicles. B) A zoomed in image of local region (yellow box) from A depicting some free QDs in the nucleus. The scale bars in A and B are 2 and 0.1 μm, respectively. Nuclei are labeled N for clarity.

Table 4.2: Dissociation media ingredients.

Compounds	Volumes for 400 mL	Concentrations
Water	364.5 mL	
Magnesium chloride	2.32 mL	1 M
Calcium chloride	1 mL	1 M
HEPES	1.28 mL	0.5 M
Phenol red	800 μL	
Sodium hydroxide	800 μL	0.1 N
Sodium sulfate	18 mL	2 M
Potassium sulfate	15 mL	0.5 M
Adjust to pH 7.4 with $\sim$40 μL of 0.1 N sodium hydroxide. Filter sterilize through a 0.22 μm filter and store at 4^{o}C.		

4.4 Acknowledgments

Chapter 4, in part, contains data as it appears in Nguyen-Ta, Kim. Characterization of peptide-mediated delivery of quantum dots into cortical astrocytes. Thesis, UCSD, 2011. The dissertation author was a secondary investigator for this material.

4.5 References

1. J Pepe, M Rincón, J Wu. Experimental comparison of sonoporation and electroporation in cell transfection applications. *Acoustics Research Letters Online*, 5(2):62-67, 2004.

2. CY Okada and M Rechsteiner. Introduction of macromolecules into cultured mammalian cells by osmotic lysis of pinocytic vesicles. *Cell*, 29(1):3341, 1982.

3. M Zorko and U Langel. Cell-penetrating peptides: mechanism and kinetics of cargo delivery. *Advanced Drug Delivery Reviews*, 57(4):529545, 2005.

4. YH Wang, YW Hou, and HJ Lee. An intracellular delivery method for sirna by an arginine-rich peptide. *Journal of Biochemical and Biophysical Methods*, 70(4):57986, 2007.

5. GP Dietz and M Bahr. Delivery of bioactive molecules into the cell: the trojan horse approach. *Molecular and Cellular Neuroscience*, 27(2):85131, 2004.

6. IL Medintz, T Pons, JB Delehanty, K Susumu, FM Brunel, PE Dawson, and H Mattoussi. Intracellular delivery of quantum dot-protein cargos mediated by cell penetrating peptides. *Bioconjugate Chemistry*, 19(9):1785 95, 2008.

7. P Guterstam, F Madani, H Hirose, T Takeuchi, S Futaki, S El Andaloussi, A Graslund, and U Langel. Elucidating cell-penetrating peptide mechanisms of action for membrane interaction, cellular uptake, and translocation utilizing the hydrophobic counter-anion pyrenebutyrate. *Biochimica et Biophysica Acta*, 1788 (12):250917, 2009

8. S Futaki, T Suzuki, W Ohashi, T Yagami, S Tanaka, K Ueda, and Y Sugiura. Arginine-rich peptides. an abundant source of membrane-permeable peptides having potential as carriers for intracellular protein delivery. *Journal of Biological Chemistry*, 276(8):583640, 2001.

9. Y Xu, BR Liu, HJ Lee, KB Shannon, JG Winiarz, TC Wang, HJ Chiang, and YW Huang. Nona-arginine facilitates delivery of quantum dots into cells via multiple pathways. *Journal of Biomedicine and Biotechnology*, 2010:948543, 2010.

10. I Nakase, M Niwa, T Takeuchi, K Sonomura, N Kawabata, Y Koike, M Takehashi, S Tanaka, K Ueda, JC Simpson, AT Jones, Y Sugiura, and S Futaki. Cellular uptake of arginine-rich peptides: roles for macropinocytosis and actin rearrangement. Mol Ther, 10(6):101122, 2004.

11. M Green and PM Loewenstein. Autonomous functional domains of chemically synthesized human immunodeficiency virus tat trans-activator protein. *Cell*, 55(6):11791188, 1988.

12. AD Frankel and CO Pabo. Cellular uptake of the tat protein from human immunodeficiency virus. *Cell*, 55(6):11891193, 1988.

13. KM Stewart, KL Horton, and SO Kelley. Cell-penetrating peptides as delivery vehicles for biology and medicine. *Organic & Biomolecular Chemistry*, 6(13):2242-2255, 2008.

14. F Heitz, MC Morris, G Divita. Twenty years of cell-penetrating peptides: from molecular mechanisms to therapeutics. *British Journal of Pharmacology*, 157(2):195206, 2009.

15. E Vivès, J Schmidt, A Pèlegrin. Cell-penetrating and cell-targeting peptides in drug delivery. *Biochimica et Biophysica Acta*, 1786(2):126-138, 2008.

16. P Kumar, H Wu, JL McBride, K-E Jung, MH Kim, BL Davidson, SK Lee, P Shankar, and N Manjunath. Transvascular delivery of small interfering RNA to the central nervous system. *Nature*, 448(7149):39-43, 2007.

17. II Kruman, A Nath, MP. Mattson. HIV-1 protein tat induces apoptosis of hippocampal neurons by a mechanism involving caspase activation, calcium overload, and oxidative stress. *Experimental Neurology*, 154(2):276-288, 1998.

18. B Shi, J Raina, A Lorenzo, J Busciglio, and D Gabuzda. Neuronal apoptosis induced by HIV-1 Tat protein and TNF-: potentiation of neurotoxicity mediated by oxidative stress and implications for HIV-1 dementia. *Journal of Neoruvirology*, 4(3):281-290, 1998.

19. TO Price, N Ercal, R Nakaoke, WA Banks. HIV-1 viral proteins gp120 and Tat induce oxidative stress in brain endothelial cells. *Brain Research*, 1045(1-2):57-63, 2005.

20. KE Sapsford, T Pons, IL Medintz, S Higashiya, FM Brunel, PE Dawson, and H Mattoussi. Kinetics of metal-affinity driven self-assembly between proteins or peptides and cdse-zns quantum dots. *Journal of Physical Chemistry C*, 111(31):1152811538, 2007.

21. C Chapman-Andresen. Endocytosis in freshwater amebas. *Physiological Reviews*, 57(3):371-385, 1977.

22. DK Niarchos, SA Perez, and M Papamichail. Characterization of a novel cell penetrating peptide derived from bag-1 protein. *Peptides*, 27(11):2661 2669, 2006.

23. D Kalderon, BL Roberts, WD Richardson, and AE Smith. A short amino acid sequence able to specify nuclear location. *Cell*, 39(3):499-509, 1984.

24. MJ Berridge. Calcium microdomains: Organization and function. *Cell Calcium*, 40(5-6):405-412, 2006.

25. TA Fiacco, KD McCarthy. Astrocyte calcium elevations: Properties, propagation, and effects on brain signaling. *Glia*, 54(7):676-690, 2006.

26. H Duan and S Nie. Cell-penetrating quantum dots based on multivalent and endosome-disrupting surface coatings. *Journal of the American Chemical Society*, 129(11):3333-3338, 2007.

27. Y-B Lim, S-M Kim, H Suh, and J-S Park. Biodegradable, endosome disruptive, and cationic network-type polymer as a highly efficient and nontoxic gene delivery carrier. *Bioconjugate Chemistry*, 5(13):952-957, 2002.

28. Live/dead (r) viability/cytotoxicity kit for mammalian cells. *Invitrogen*, 2005.

Chapter 5

Sulforhodamine B-loaded polyethyleneimine/silica hybrid nanoparticles

5.1 Communication

Biosensors and labeling technologies continue to play a central role in molecular and cell biological experiments aimed at uncovering and understanding both the structure and function of cells. As the biological questions have become more detailed and challenging to address from a methodological perspective, biosensor fluorescent probe technologies and methods have had to improve, becoming ever more sophisticated and sensitive. For example, of the existing wide range of technologies, reactive dyes have enabled direct conjugation of highly fluorescent molecules to targets of interest [1-3], fluorescent proteins have permitted target cells to produce their own protein-based sensors and labels [4, 5], and quantum dots (QDs) with high quantum yields have provided bright labels that are individually distinguishable at a molecular level using light microscopy [6]. While each approach provides its own unique advantages, all methods have shortcomings and limitations that must be overcome to advance biotechnology and imaging at the nano scale, and to permit the pursuit of deeper, more sophisticated questions.

While useful, Reactive dyes are often prone to photobleaching [7, 8] and can be rather expensive. Fluorescent proteins are susceptible to photobleaching [8-10], as well, and require manipulation of target cell genomes, which can also be expensive and extremely time-consuming. Quantum dots, on the other hand, are relatively cheap, photostable, and provide a large surface area for derivatization and cell interaction, but their size often inhibits cellular delivery, and they can be difficult to derivatize without a significant loss of fluorescence [6, 8, 11, 12]. Avoiding this loss of fluorescence typically results in thick coatings unsuited for fluorescence resonance energy transfer (FRET) approaches frequently employed in optical nanosensors.

Another class of nanoparticles that has attracted significant interest derives

from silica. Silica nanoparticles are inherently biocompatible and have a wide array of commercially available precursors. A number of groups have conjugated reactive dyes to amine-functional trialkoxysilanes, permitting their integration into growing silica matrices [13-17]. This provides the robust quantum yield of organic fluorophores with the versatility of derivatizable nanoparticles. Additionally, entrapment of dyes increases photostability by reducing exposure to reactive oxygen species in the environment, which typically cause photobleaching. The biocompatibility of silica also makes them preferable to QDs, which contain toxic inorganics such as cadmium [11, 12, 18].

While silica nanoparticles offer a number of chemical and biological advantages that have pushed their development and investigation, there remains considerable room for improvement of the technology. The reactive dyes are expensive, and the need for multiple isolated reaction steps is time-consuming and undesirable. More recently several groups have attempted to grow silica nanoparticles and entrap dyes without direct conjugation [19-21]. Unfortunately, high dye loading has only been shown with positively charged dyes [21], likely due to the negative charge of the silica matrix. The desirability of incorporating cheap, high quantum yield molecules typically used and accepted in biological experiments, such as sulforhodamine B (SRB), led us to develop a new protocol that facilitates the loading of negatively charged dyes. Our approach took advantage of a polyethyleneimine (PEI) as a co-matrix within the growing silica particles. The motivation for this work was a synthesis scheme that was simple and used common materials, reproducible, robust, of high yield, and which allowed us to encapsulate a biologically tested molecule (SRB).

To synthesize particles, we adapted typical reverse micelle techniques. These methods utilize specific amphiphilic molecules to suspend aqueous solutions

within various organic solvents. The aqueous system is divided into a large number of nanoreactors, each providing a site for the growth of a single nanoparticle. Recent studies have made use of cyclohexane/triton-X100/n-hexanol reverse micelle systems [19-21], but for various reasons we settled on an older system, dioctyl sulfosuccinate sodium (DSS)/2,2,4-trimethylpentane (TMP).

Including SRB in the aqueous solution resulted in very little dye entrapment regardless of our chosen type of reverse micelle. This was not surprising as the negative charge interacts unfavorably with growing silica matrix, likely causing the dye to accumulate outside growing particles, rather than being trapped within them. Additionally, it likely inhibits growth of the silica around a given dye molecule, repelling free silicic acid. To overcome this, we decided to incorporate a positively charged matrix that could both adsorb the dye and permit encapsulation within silica particles.

We chose PEI for our positive matrix due to its widespread availability, concentration of positive charge, and ease of derivatization. While the PEI did improve SRB solubility, it still failed to facilitate much dye entrapment. We believe the PEI molecules adsorb the dye, but the silica particles grow from a single seed within the micelles, keeping the PEI at its surface, but failing to merge with it. In efforts to improve our results, we decided to crosslink the PEI with fumaryl chloride prior to initiating nanoparticle growth. The intent was to physically trap the SRB within the matrix, instead of relying solely on electrostatic adsorption. Furthermore, we hoped to form more rigid structures within the micelles, creating nanoskeletons of sorts. To improve incorporation in the silica, we also linked the PEI directly to an amino-functional silica precursor ((3-aminopropyl)triethoxysilane), providing for direct covalent linkage to growing nanoparticles.

This methodology was much more successful, significantly improving dye

loading. The cyclohexane solvent system, though, resulted in what appeared to be large masses of fused particles. This occurred to a lesser extent in our trimethylpentane alternative, leading us to focus on it, instead. We prepared two varieties of particles with this method; some were left as is, and some were reacted with itaconic anhydride during purification.

Silica particles produced through these methods are by nature mesoporous. As such, dye can leak out even after initial entrapment. The itaconic anhydride was intended to react with exposed primary and secondary amines within these pores, creating additional physical barriers to escape. Itaconic anhydride was chosen specifically as an intramolecular anhydride that would produce both carboxylate moieties and α,β-unsaturated carbonyls. Both functionalities provide for further derivatization, the double bond in particular providing a simple route for UV polymerization. Additionally, the negative charge of the carboxylate in aqueous solutions would electrostatically hinder dye release.

The simple technique produced large quantities of polydisperse silica nanoparticles (Figure 5.1) with mean diameter of 74$\pm$20 nm (Figure 5.2); there was no significant difference between populations with or without itaconic anhydride. Given the large polydispersity, we analyzed the population more closely to ascertain any potential abnormalities, such as skewing, or the presence of multiple subpopulations with distinct means. We binned our particle diameters in 10 nm increments and averaged each bin to obtain a population density at a given diameter. The resulting distribution overlaps well with the standard Gaussian estimate. The median diameter, 70 nm, also falls within the 95% confidence interval for the mean indicating a negligible amount of skewing.

We analyzed particle shape, as well, using 2-dimensional eccentricities as an estimate of 3-dimensional sphericality. Using best fit ellipses from transmis-

sion electron microscopy (TEM) images, we determined mean eccentricity to be 0.48±0.18. While particles typically exhibited fairly spherical structures (Figure 5.2), the presence of particle fusions and some smaller irregular structures produces the large standard deviation. We also noted the particle surfaces to be rather rough. We suspect this to be a product of the high polymer content, leading to multiple regions of independent silica growth and inhibiting their merging. There may also be a high polymer content at the surface, which could also explain the topography.

Of particular interest was the particle quantum yield, Φ. We wanted to develop a protocol that yielded high dye-loading and, hence, high quantum yield. We compared our particle absorbance and fluorescence in water to that of two standards in ethanol, sulforhodamine 101 (Φ = 0.90) and sulforhodamine B (Φ = 0.83), using [22-24]:

$$\Phi_{unkown} = \Phi_{known} \cdot \left(\frac{m_{unknown}}{m_{known}} \right) \cdot \left(\frac{\eta_{unkown}}{\eta_{known}} \right)^2, \tag{5.1}$$

where m is the slope of cumulative fluorescence relative to absorbance, and ν is the refractive index of the solvent used [25].

Particles that were not coated with itaconic anhydride presented a quantum yield of 0.14±0.01 in water (Figure 5.3), a value that falls at the lower end of commercial probes (Alexa Fluor dyes vary between Φ = 0.1 and Φ = 0.9) [26]. Coated particles, however, displayed a Φ of 0.27±0.02 in water. The large increase in yield indicates improved dye entrapment. Furthermore, this yield is more typical of commercial dyes, augmenting its value as a replacement for standard fluorophores.

Particle absorbance and emission is depicted in Figure 5.4. The bulk of the absorbance peak falls between 500 and 600 nm, with a maximum near 560 nm.

Under 520 nm excitation, the bulk of fluorescence occurs between 530 and 630 nm with a maximum near 580 nm. Normalizing the values for absorbance and fluorescence, respectively, it can be seen that both particle types have similar emission spectra, but the slight deviation between their absorbance characteristics should be noted. Particles that were not reacted with itaconic anhydride possessed a higher relative absorbance density around 520 nm than coated particles, indicating the anhydride may have effects beyond simply increasing dye entrapment.

Both particle types show promise as alternatives to conventional fluorescent probes utilized in aqueous systems. They possess high quantum yield, are easy to derivatize, and are composed of low-cost, biocompatible materials. The simplicity and versatility of the chemistry involved in their synthesis is also attractive to biological researchers that lack expensive, dedicated chemical and analytical equipment or chemical expertise. The wide commercial availability of silica precursors provides numerous options for surface functionality and enables the attachment of bioactive molecules in whatever fashion is most convenient. The inherent dispersibility of these particles in water simplifies their use in biological systems.

These probes should also be able to be integrated into other systems. For example, we have recently developed a calcium sensitive QD-FRET probe [27]. One of the challenges with this system is a decay in fluorescence during QD modification for aqueous dispersion, a critical requirement if such a system is to be used under cell biological conditions. The silica nanoparticles we describe here should be able to replace quantum dots in nanosensor designs. This would not only address inherent limitations in QD fluorescent quenching under biological conditions, but would also support longer term biological experiments; the long term exposure of cells to QDs can result in cytotoxicity due to the presence of heavy metal cores.

One immediate limitation of these silica nanoparticles is their current size;

they are four to ten times the diameter of most commercial QDs, which may be a problem for some cell applications. This issue can likely be overcome by utilizing appropriate surface modifications and physical or chemical methods to aid cell delivery and distribution, a very active area of research in its own right, being explored for the delivery of all kinds of other nanoscale cellular probes. Nonetheless, this does represent a limitation that needs further consideration.

5.2 Experimental

Materials: Materials were obtained from Sigma-Aldritch, unless otherwise noted. (3-aminopropyl)triethoxysilane (APTES); ammonium hydroxide (28% NH3 in water); dioctyl sulfosuccinate sodium salt (DSS); ethanol (from Gold Shield Chemical Company); fumaryl chloride ($FuCl_2$); itaconic anhydride (IA); polyethyleneimine (PEI; 50% in water, Mw 2000); sulforhodamine 101 (SR101); sulforhodamine B (SRB); tetraethyl orthosilicate (TEOS); 2,2,4-trimethylpentane (TMP).

Absorbance and fluorescence measurements: All measurements were made using an M5 spectrophotometer from Molecular Devices in a Starna quartz cuvette with a path length of 1 cm. Nanoparticle were analyzed in deionized water. Quantum yields (Φ) were determined relative to sulforhodamine B ($\Phi = 0.83$) and sulforhodamine 101 ($\Phi = 0.90$) in ethanol [22-24]. The control dyes were cross-calibrated to confirm accuracy of fluorescence measurements. Excitiation was performed at 520 nm and emission readings taken every 2 nm from 535 nm to 735 nm. Absorbance was measured at the excitation wavelength, and 5 readings were made for each of the controls and samples. Relative fluorescence quantum yields were calculated according to Equation (5.1), which appears in the main text.

Nanoparticle synthesis: To 10 mL 0.1 M DSS in TMP, 300 μL 0.033 M SRB in 10% PEI was added. Throughout the reaction, the mixture was stirred continuously in a 50 mL polypropylene conical tube. 2.5 mL TMP containing 4 μL APTES was added to 2.5 mL TMP containing 3.75 μL $FuCl_2$. This was reacted for 15 minutes, then added to the 10 mL SRB solution. After another 15 minutes, 1 mL of 0.1 M DSS in TMP containing 50 μL 28% NH3 was added to the mixture. This was left to stir for 15 minutes, then filtered through a 0.2 μm syringe filter. Finally, 200 μL TEOS was added and the entire reaction volume was stirred for 24 hours.

To purify particles, an equal volume of acetone was added to disrupt micelles and quench the reaction. The mixture was centrifuged in 1.5 mL eppendorf tubes at $\sim$14000 g for 15 minutes. The supernatant was discarded and the pellets washed 3 times with ethanol and 3 times with water. To cap particles, the third ethanol wash contained 10 mM IA. Particles were kept suspended in this solution for 1 hour. Mild Sonication was necessary to resuspend the pellet into solvents, and each resuspension was followed by a 15-minute centrifugation at $\sim$14000 g. Resuspensions were combined as desired to concentrate particles. The final pellet was dispersed in water for subsequent analysis.

Physical characterization of nanoparticles: Transmission electron micrographs were analyzed to determine the distribution of nanopraticle size and shape. Image analysis was performed with ImageJ software. Particles were manually outlined. Their two-dimensional areas were used to estimate diameters, and best fit ellipses of these areas were used to determine eccentricities, approximating deviation from sphericality.

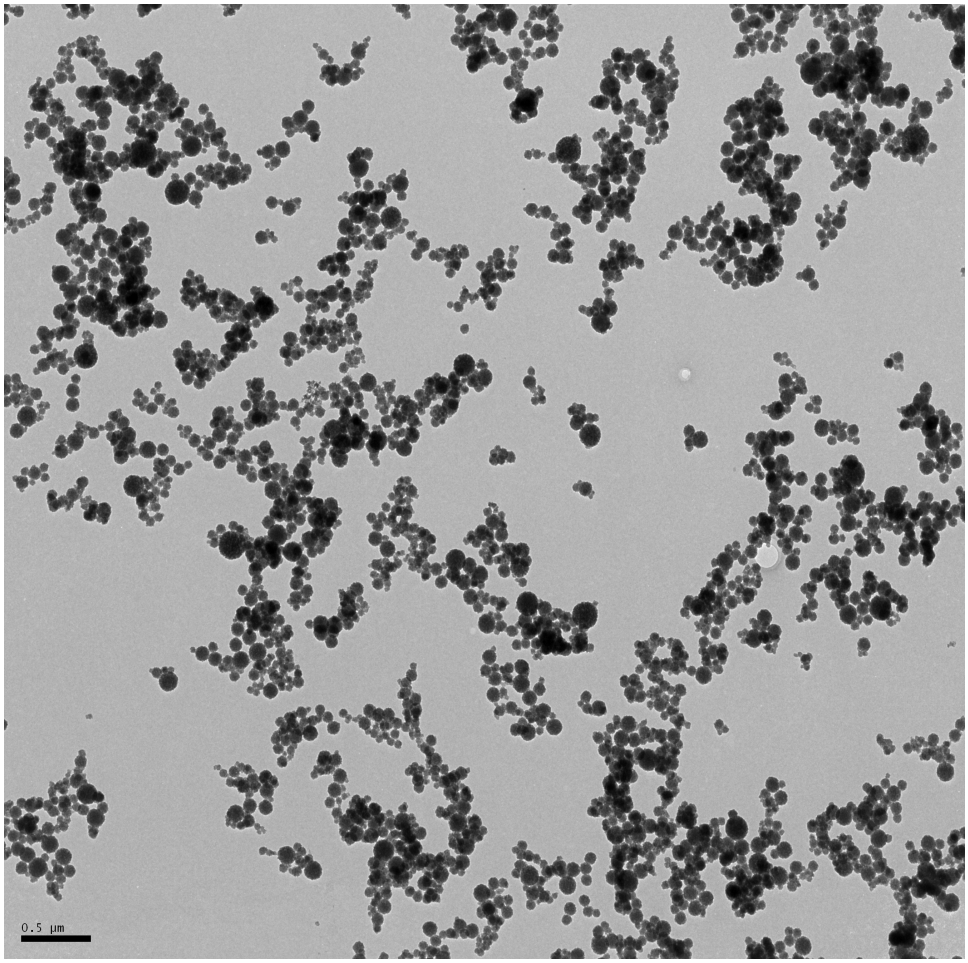

Figure 5.1: A field of nanoparticles. The scale bar is 0.5 μm.

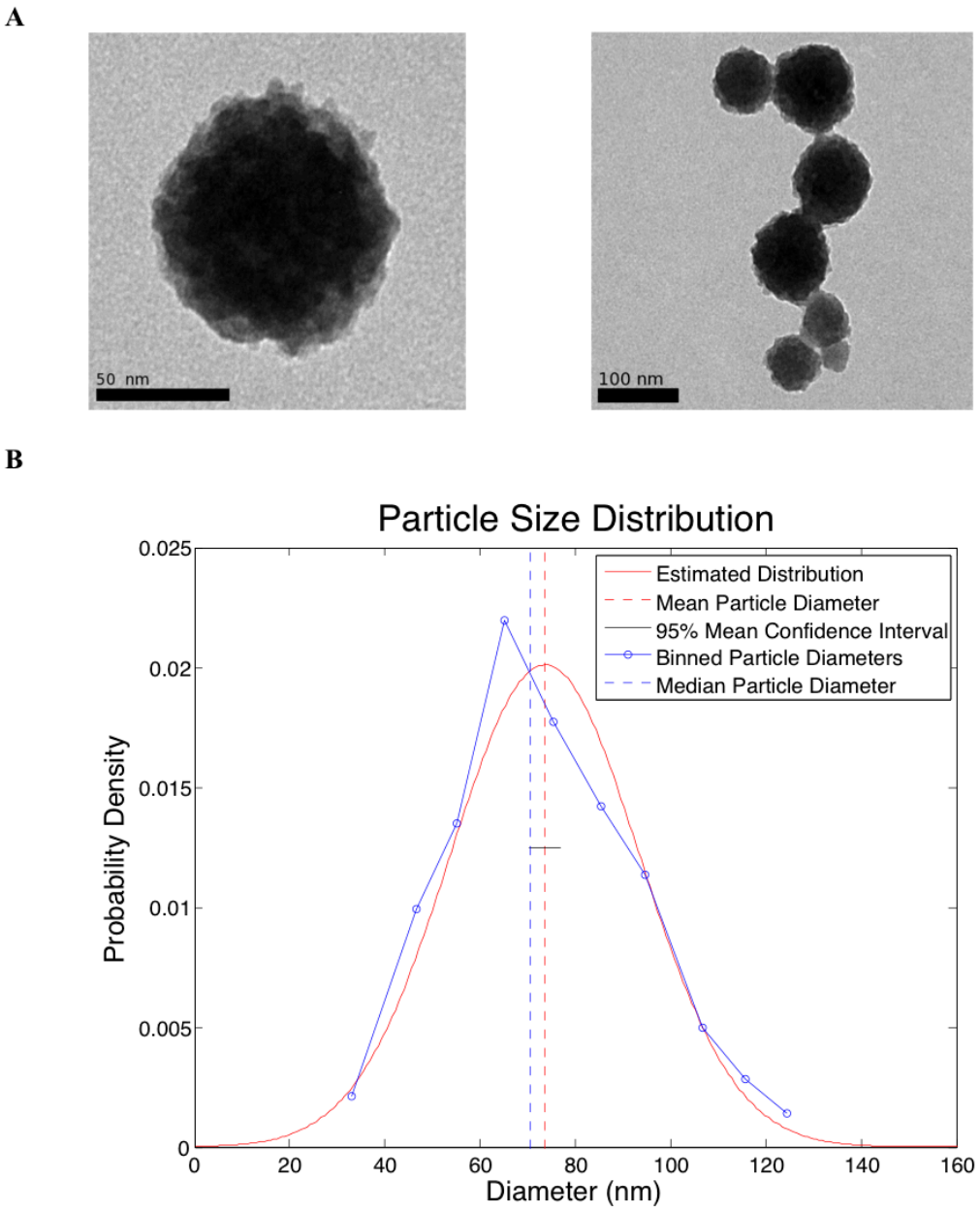

Figure 5.2: Physical characteristics of the particles. (A) Illustrates a typical isolated particle (left) and an aggregate of large and small particles (right). The graph in (B) shows the normalized particle diameter counts (binned and averaged over 10 nm intervals) along with the Gaussian estimate of particle distribution. The black bar through the mean line indicates its 95% confidence interval.

Graph 5.1: Cumulative particle fluorescence versus absorbance. The quantum yield of NPs in water was determined from the respective cumulative fluorescence curves of SR101 (red), SRB (green), and the two NP samples, bare and coated with itaconic anydride (blue).

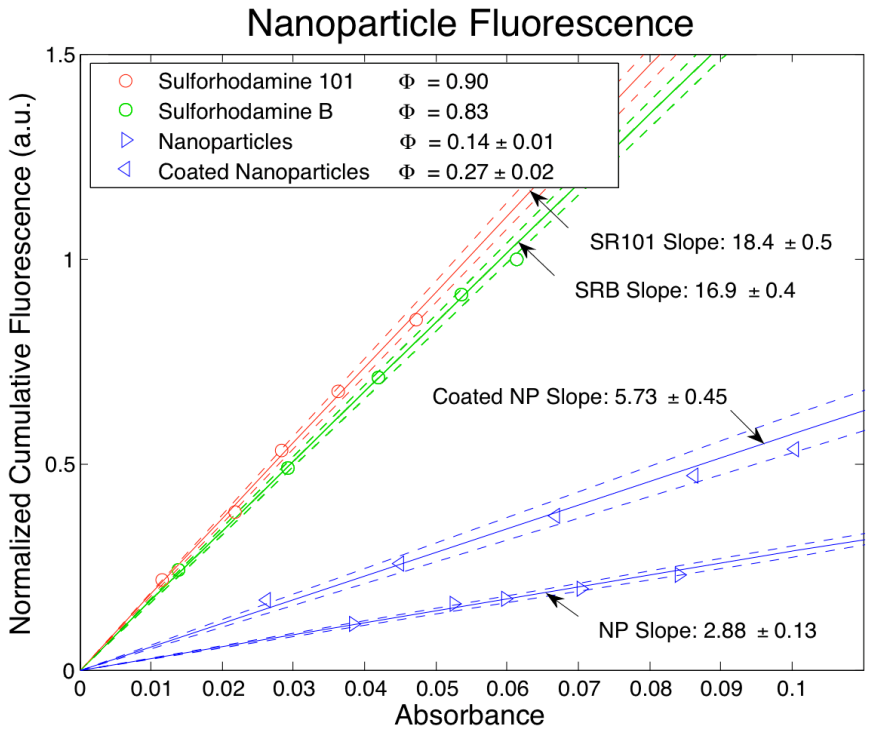

Graph 5.2: Normalized particle absorbance and fluorescence. The data in both graphs are normalized to arbitrary units for illustrative purposes. The top graph displays the relative absorbance of the two particle types given equivalent cumulative fluorescence under 520 nm excitation. The bottom graph displays relative fluorescence given equivalent 520 nm absorbance.

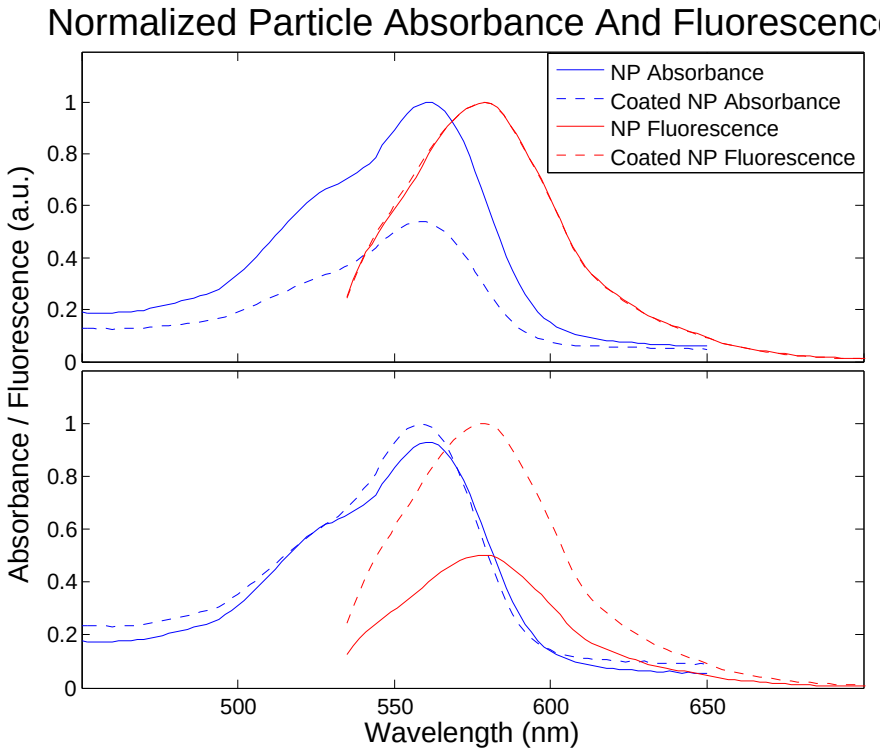

5.3 Acknowledgments

The authors would like to thank Dr. Marilyn Farquhar for the use of the electron microscopy facility, and Ying Jones and Timo Meerloo for aid with electron microscopy sample preparation. This work was supported by NINDS NIH grant NS054736.

Chapter 5, in full, has been submitted for publication of the material as it may appear in Blumling, James P.; Silva, Gabriel A. Sulforhodamine B-loaded polyethyleneimine/silica hybrid nanoparticles, Small, submitted (2012). The dissertation author was the primary investigator and author of this material.

5.4 References

1. JW Goding. Conjugation of antibodies with fluorochromes: modifications to the standard methods. *Journal of immunological methods*, 13(3-4):215226, Jan 1976.

2. Y Kim, SO Ho, NR Gassman, Y Korlann, EV Landorf, FR Collart, and S Weiss. Efficient site-specific labeling of proteins via cysteines. *Bioconjugate Chemistry*, 19(3):786791, Mar 2008.

3. RB Mujumdar, LA Ernst, SR Mujumdar, CJ Lewis, and AS Waggoner. Cyanine dye labeling reagents: sulfoindocyanine succinimidyl esters. *Bioconjugate Chemistry*, 4(2):105111, Jan 1993.

4. BJ Baker, H Mutoh, D Dimitrov, W Akemann, A Perron, Y Iwamoto, L Jin, LB Cohen, EY Isacoff, VA Pieribone, T Hughes, and T Knopfel. Genetically encoded fluorescent sensors of membrane potential. *Brain Cell Biology*, 36(1-4):5367, Jan 2008.

5. M Mank and O Griesbeck. Genetically encoded calcium indicators. *Chemical reviews*, 108(5):15501564, Jan 2008.

6. X Michalet, FF Pinaud, LA Bentolila, JM Tsay, S Doose, JJ Li, G Sundaresan, AM Wu, SS Gambhir, and S Weiss. Quantum dots for live cells, in vivo imaging, and diagnostics. *Science*, 307(5709):538544, Jan 2005.

7. LA Deschenes and DAV Bout. Single molecule photobleaching: increasing photon yield and survival time through suppression of two-step photolysis. *Chemical Physics Letters*, 365(5-6):387395, Jan 2002.

8. JK Jaiswal and SM Simon. Potentials and pitfalls of fluorescent quantum dots for biological imaging. *Trends in Cell Biology*, 14(9):497504, Jan 2004.

9. GH Patterson, SM Knobel, WD Sharif, SR Kain, and DW Piston. Use of the green fluorescent protein and its mutants in quantitative fluorescence microscopy. *Biophysical Journal*, 73(5):27822790, Nov 1997.

10. J Lippincott-Schwartz and GH Patterson. Development and use of fluorescent protein markers in living cells. *Science*, 300(5616):8791, Apr 2003.

11. F Pinaud, X Michalet, LA Bentolila, JM Tsay, S Doose, JJ Li, G Iyer, and S Weiss. Advances in fluorescence imaging with quantum dot bio-probes. *Biomaterials*, 27(9):16791687, Mar 2006.

12. T Jamieson, R Bakhshi, D Petrova, R Pocock, M Imani, and AM Seifalian. Biological applications of quantum dots. *Biomaterials*, 28(31):47174732, Nov 2007.

13. DR Larson, H Ow, HD Vishwasrao, AA Heikal, U Wiesner, and WW Webb. Silica nanoparticle architecture determines radiative properties of encapsulated fluorophores. *Chemistry of Materials*, 20(8):26772684, 2008.

14. R Hardman. A toxicologic review of quantum dots: Toxicity depends on physicochemical and environmental factors. *Environental Health Perspectives*, 114(2):165172, Jan 2006.

15. CW Lu, Y Hung, JK Hsiao, M Yao, TH Chung, YS Lin, SH Wu, SC Hsu, HM Liu, and CY Mou. Bifunctional magnetic silica nanoparticles for highly efficient human stem cell labeling. *Nano Letters*, 7(1):149154, 2007.

16. H Ow, DR Larson, M Srivastava, BA Baird, WW Webb, and U Wiesner. Bright and stable core-shell fluorescent silica nanoparticles. *Nano Letters*, 5(1):113117, 2005.

17. AA Burns, J Vider, H Ow, E Herz, O Penate-Medina, M Baumgart, S M Larson, U Wiesner, and M Bradbury. Fluorescent silica nanoparticles with efficient urinary excretion for nanomedicine. *Nano Letters*, 9(1):442448, 2009.

18. AA Burns, H Ow, and U Wiesner. Fluorescent coreshell silica nanoparticles: towards lab on a particle architectures for nanobiotechnology. *Chemical Society Reviews*, 35(11):10281042, 2006.

19. A Auger, J Samuel, O Poncelet, and O Raccurt. A comparative study of non-covalent encapsulation methods for organic dyes into silica nanoparticles. *Nanoscale Research Letters*, 6(1):112, 2011.

20. S Santra and SR Grobmyer. Fluorescent silica nanoparticles for cancer imaging. *Methods in Molecular Biology*, 624:151162, 2010.

21. S Santra, K Wang, R Tapec, and W Tan. Development of novel dye-doped silica nanoparticles for biomarker application. *Journal of Biomedical Optics*, 6:160, 2001.

22. R Pribik, K Aslan, Y Zhang, and CD Geddes. Metal-enhanced fluorescence from chromium nanodeposits. *The Journal of Physical Chemistry C*, 112(46):1796917973, 2008.

23. DL Sackett and J Wolff. Nile red as a polarity-sensitive fluorescent probe of hydrophobic protein surfaces. *Analytical Biochemistry*, 167(2):228234, 1987.

24. JM Drake, RI Morse, RN Steppel, and D Young. Kiton red s and rhodamine b. The spectroscopy and laser performance of red laser dyes. *Chemical Physics Letters*, 35(2):181188, 1975.

25. Jobin Yvon Ltd. A Guide to Recording Fluorescence Quantum Yields. http://www.horiba.com/fileadmin/uploads/Scientific/Documents/-Fluorescence/quantumyieldstrad.pdf.

26. Life Technologies Corporation. Fluorescence quantum yields (QY) and lifetimes (τ) for Alexa Fluor dyes Table 1.5. http://www.invitrogen.com/site/us/en/home/References/Molecular-Probes-The-Handbook/tables/Fluorescence-quantum-yields-and-lifetimes-for-Alexa-Fluor-dyes.html.

27. S-J Kim, JP Blumling III, MC Davidson, H Saad, S-Y Eun, and GA Silva. Calcium and EDTA induced folding and unfolding of calmodulin on functionalized quantum dot surfaces. *Nanoneuroscience*, in press.

Chapter 6

Future Directions

Nanotechnology has a very important role to play in neuroscience, both as a tool of observation and discovery and in treatments for many of the most debilitating illnesses. In the broadest sense, I see continued growth in the use of micelles, vesicles, and polymeric nanoparticles as delivery agents for drugs and therapeutics. Their beauty lies in an ease of production and an ease of modification. In particular, increasing attention is being paid to surface modifications of these nanodelivery modalities. The use of cell-penetrating peptides, synthetic polymers, and trojan horse molecules have enabled transmembrane delivery of a host of different cargo, and overcome many obstacles of traditional pharmacological delivery. Furthermore, the increased understanding of these delivery molecules has permitted their tailoring, and the development of simplified strategies for incorporation into nanodevices has enabled multiplexed systems, both providing for highly specific and efficient delivery to select sites within a select class of cells among larger mixed populations. These sort of tailored approaches are the future of medicine and biotechnology, providing for safe and effective delivery in complicated biological systems.

In pursuit of this future, we see definitive directions for our research. Our calcium sensor needs to be optimized for the ranges of calcium we wish to observe; this can be accomplished via site-directed mutagenesis near the calcium binding sites of calmodulin. By slightly modifying the amino acids in these areas, we can increase or decrease the calcium affinity of these binding sites. Having different sensors effective over a variety calcium levels enables the exploration of calcium variations in multiple environments.

Exchanging the quantum dot core with a more biocompatible alternative would also be beneficial. The cadmium present in conventional QDs is rather toxic

to biological tissues, and even in capped nanodevices the ions diffuse into the environment can cause damage. Minimizing the negative impact of our research tools on their subjects not only reinforces the validity of results, but permits longer-term studies. To achieve biocompatible sensors, we must improve our silica-based fluorescent nanoparticles and incorporate them into our nanodevice. Particle polydispersity should be minimized, which may require alternate solvent conditions or extending the time over which particles are grown. Additionally, dye retention needs to be improved within biological buffers. This may also be improved by extending the particle growth phase (by reducing the concentration of the ammonium catalyst); allowing more time for complete hydrolysis of the alkoxysilanes incorporated within the micelles would increase the available surface area for incorporation of new, partially hydrolyzed alkoxysilanes and encourage 'holes' in the the structures to be filled. This would provide a greater barrier to dye escape. Moreover, other molecules can be employed to derivatize exposed amines and create further barriers (our choice of itaconic anhydride was mostly for convenience and potential utility in later derivitizations).

It should be noted that in the case of replacing QDs with our silica NPs we would need to implement a different strategy for conjugation to our calcium-responsive, calmodulin-based unit. Fortunately, a silica based system permits conjugation of desired molecules to any of the numerous functionalized silica precursors commercially available. Moreover, this conjugation can be performed directly to modified particle surface, or to the precursor and added to particles with unmodified surfaces. Simple approaches include utilizing a thiolated precursor and a cysteine-terminated peptide; a disulfide bond can be formed in a mildly oxidizing environment, or a bismaleimide linker could be used instead. Other options with a cysteine residue are to employ a bifunctional crosslinker containing both a

maleimide (for the thiol) and an N-hydroxysuccimidyl ester for reaction with an amino-functional precursor, or to attempt reaction of the thiol with an epoxide-containing precursor. The latter alternative may run into competition with exposed amines, but the result may still be a functional device.

An efficient method of delivering these devices is also necessary. Our polyarginine peptides work well for getting particles into cells, but we need to develop effective methods for escape from endosomes. Including polymers known to encourage vesicle-escape such as poly(amido amine) [1, 2], or peptide sequences that do the same, like the N-terminal of the influenza hemagglutinin protein [3], are simple options. Using a peptide sequence is particularly attractive because it can be added directly into the CPP sequence. Furthermore, the entire sequence can be included at the end of the calmodulin unit of our sensor (although other methods of conjugation, such as those mentioned earlier, are entirely plausible). It may also be possible to use osmotic shock or another physical method to break vesicles, but these approaches would probably be applicable only *in vitro*.

Endosomal escape would be the penultimate delivery step, followed by intracellular localization. This would be achieved most simply through various peptide localization sequences for, perhaps, the nucleus, endoplasmic reticulum, or mitochodria. Certain RNAs are also localized in neural cells, and it may be desirable to incorporate subsets of these into our device for fine-tuned delivery to axons or dendrites [4]. These molecules, however, need to be incorporated into our device apart from our protein units. Additionally, this becomes more expensive, as nucleic acids with functional groups for simple conjugation are not easily synthesized in cells, whereas plasmids can be developed and inserted into cell lines to produce peptides with easily derivitizable groups. It may, therefore, be more prudent to hijack proteins that are in locations of interest using specific antibodies or other

protein fragments that would bind them.

Our final, complete system would be a family of sensors for use in multiple environments having distinct calcium regimes. They would contain biocompatible, stable fluorophores (possibly a unique FRET pair for each type of sensor) and traverse cell membranes using CPPs. Devices that are trapped in endosomes would escape through biological mechanisms using additional peptide sequences, and localize within cells by incorporating protein fragments or signal sequences specific to regions of interest. Once delivered, conventional fluoescence microscopy would enable detailed observation of large networks of cells, providing simultaneous visualization of the entire population's calcium dynamics, including microdomains within cells.

6.1 References

1. H Duan and S Nie. Cell-penetrating quantum dots based on multivalent and endosome-disrupting surface coatings. *Journal of the American Chemical Society*, 129(11):3333-3338, 2007.

2. Y-B Lim, S-M Kim, H Suh, and J-S Park. Biodegradable, endosome disruptive, and cationic network-type polymer as a highly efficient and nontoxic gene delivery carrier. *Bioconjugate Chemistry*, 5(13):952-957, 2002.

3. JS Wadia, RV Stan, and SF Dowdy. Transducible TAT-HA fusogenic peptide enhances escape of TAT-fusion proteins after lipid raft macropinocytosis. *Nature Medicine*, 10(3):310-315, 2004.

4. CE Holt and SL Bullock. Subcellular mRNA Localization in animal cells and why it matters. *Science*, 326(5957):1212-1216, 2009.